Evolution of a sand-rich submarine channel-lobe system and impact of mass-transport and transitional flow deposits on reservoir heterogeneity: Magnus Field, northern North Sea

Michael J. Steventon[1*], Christopher A-L. Jackson[1], Howard D. Johnson[1], David M. Hodgson[2], Sean Kelly[3], Jenny Omma[4], Christine Gopon[4], Christopher Stevenson[5] & Peter Fitch[1]

[1]Basins Research Group (BRG), Department of Earth Science & Engineering, Imperial College, Prince Consort Road, London, SW7 2BP
[2]School of Earth and Environment, University of Leeds, Leeds, LS2 9JT
[3]EnQuest PLC, Annan House, Palmerston Road, Aberdeen, AB11 5QP
[4]Rocktype Ltd, 87 Divinity Road, Oxford, OX4 1LN
[5]School of Earth, Ocean and Ecological Sciences, University of Liverpool, Liverpool, L69 3GP

[*]Correspondence: m.steventon@shell.com

Running header: *Impact of mass-transport and transitional flow deposits on reservoir heterogeneity*

Conflict of interest: The authors declare no known conflicts of interest associated with this publication.

ABSTRACT

The geometry, distribution, and rock properties (i.e. porosity and permeability) of turbidite reservoirs, and the processes associated with turbidity current deposition, are relatively well known. However, less attention has been given to the equivalent properties resulting from laminar sediment gravity-flow deposition, with most research limited to cogenetic turbidite-debrites (i.e. transitional flow deposits) or subsurface studies that focus predominantly on seismic-scale mass-transport deposits (MTDs). Thus, we have a limited understanding of the ability of sub-seismic MTDs to act as hydraulic seals and their effect on hydrocarbon production, and/or carbon storage. We investigate the gap between seismically resolvable and sub-seismic MTDs, and transitional flow deposits on long-term reservoir performance in this analysis of a small (<10 km radius submarine fan system), Late Jurassic, sandstone-rich stacked turbidite reservoir (Magnus Field, northern North Sea). We use core, petrophysical logs, pore fluid pressure, quantitative evaluation of minerals by scanning electron microscopy (QEMSCAN), and 3D seismic-reflection datasets to quantify the type and distribution of sedimentary facies and rock properties. Our analysis is supported by a relatively long (c. 37 years) and well-documented production history. We recognise a range of sediment gravity deposits: (i) thick-/thin- bedded, structureless and structured turbidite sandstone, constituting the primary productive reservoir facies (c. porosity = 22%, permeability = 500 mD), (ii) a range of transitional flow deposits, and (iii) heterogeneous mud-rich

sandstones interpreted as debrites (c. porosity = <10%, volume of clay = 35%, up to 18 m thick). Results from this study show that over the production timescale of the Magnus Field, debrites act as barriers, compartmentalising the reservoir into two parts (upper and lower reservoir), and transitional flow deposits act as baffles, impacting sweep efficiency during production. Prediction of the rock properties of laminar and transitional flow deposits, and their effect on reservoir distribution, has important implications for: (i) exploration play concepts, particularly in predicting the seal potential of MTDs, (ii) pore pressure prediction within turbidite reservoirs, and (iii) the impact of transitional flow deposits on reservoir quality and sweep efficiency.

Keywords: deep-water fan/lobe, mass-transport complex (MTC), hybrid event beds (HEBs), banded sandstones, subsurface fluid flow, reservoir characterisation, reservoir quality, QEMSCAN.

Sand-rich submarine fans are small- to moderate-sized systems (c. 5-100 km radius), typically fed by point-source feeder systems and/or shelf failure. By definition, such fans are characterised by a high percentage (c. >70%) of sand-grade material (e.g. Mutti & Normark 1987; Reading & Richards 1994; Mattern 2005). Sand-rich channel-lobe systems form high-quality reservoirs in many basins (e.g. the North Sea, Gulf of Mexico, Atlantic Passive Margins), and the stratigraphic architecture of their turbidite deposits have been extensively studied (e.g. Piper & Normark 1983; Reading & Richards 1994; Kendrick 1998; Prather 2003). An understanding of inter- and intra-reservoir heterogeneities within these systems is critical for reservoir evaluation (e.g. Garland et al. 1999; Drinkwater & Pickering 2001; Hodgson 2009). In this study, we document sub-seismic mass-transport deposits (MTDs) and transitional flow deposits (i.e. hybrid, banded, and "slurry" beds), highlighting their impact on hydrocarbon fluid flow and the stratigraphic evolution of a sand-rich fan.

MTDs and petroleum systems

MTDs are the product of creep, slide, slump, and debris flow processes (see Dott 1963; Nardin 1979; Coleman & Prior 1988; Weimer 1989). MTDs are typically sourced from slope or shelf-edge environments when the component of downslope shear stress exceeds the shear strength of the *in-situ* sediment (Hampton et al 1996). MTDs can be composed of a mixture of debrites and deformed sediments, derived from a failing slope or from substrate entrainment during emplacement (e.g. Pickering & Corregidor 2005; Flint et al. 2007; Tripsanas et al. 2008). The geometry, aerial extent, and thickness of MTDs is highly variable, ranging from <10 m thick (e.g. Auchter et al. 2016) to >100 m thick (e.g. Moscardelli et al. 2006). Here, we make a distinction between (1) *small-scale MTDs* resulting from single failure episodes and typically <10 m thick (hence usually sub-seismic, but covering most core, well-log and outcrop scales), and (2) *large-scale mass-transport complexes (MTCs)* comprising multiple, genetically related mass-transport and sediment gravity flow deposits, usually 10s-100s m thick (hence within seismic resolution), and often identified as a single seismic-stratigraphic unit (Weimer 1989; Beaubouef & Friedmann 2000; Ortiz-Karpf et al. 2016).

In petroleum systems, MTDs can act as seals (e.g. Day-Stirrat et al. 2013; Cardona et al. 2016) and less commonly as reservoirs (e.g. Jennette et al. 2000; Welbon et al. 2007; Meckel 2011). MTDs can form seals through shear deformation along a basal shear zone (BSZ), resulting in alignment of clay fabrics and increasing bulk rock density, thereby significantly reducing permeability (Dugan 2012; Day-Stirrat et al. 2013; Wu et al. 2019). Alternatively, they can act as conventional fine-grained seals with high capillary entry pressures (Downey 1984). Fluid migration can be focused along the BSZ (e.g. Sun et al. 2017), or they can form fluid bypass conduits (e.g. Gamboa & Alves 2015; Sun & Alves 2020). MTDs are also linked to zones of anomalously high fluid pressures, due to either shallow overpressure

generated by rapid sedimentation, or shallow gas accumulations where MTDs act as capillary seals (Osborne & Swarbrick 1997). The irregular top surface relief of large MTDs can influence the behaviour of subsequent sediment gravity flows and therefore, the distribution and geometry of overlying turbidite reservoirs that in some cases may form stratigraphic traps (e.g. Armitage et al. 2009; Jackson & Johnson 2009; Dykstra et al. 2011; Ortiz-Karpf et al. 2015; Kneller et al. 2016; Bell et al. 2018, Fig. 1a, b). Most work has focused on seismic-scale, sealing-MTDs, with only limited consideration given to the spatial variability of their rock properties (see Yamamoto & Sawyer 2012). Many studies use well data from shallowly buried (<1 km) MTDs, with a focus on the Gulf of Mexico (e.g. Flemings et al. 2008; Dugan 2012; Sawyer et al. 2012; Day-Stirrat et al. 2013; Wu et al. 2019). These types of studies are useful when considering the controls and location of shallow fluid flow within basins, or when analysing the failure mechanisms of submarine slopes; however, they are less relevant to understanding how MTDs may act as hydrocarbon seals, barriers, and baffles within deeply buried reservoirs. Here, we focus on MTDs that act as intra-reservoir seals, either in the form of barriers to fluid flow, forming separate reservoir compartments (e.g. Beaubouef & Abreu 2010; Algar et al. 2011), or as more localised baffles in conjunction with transitional flow deposits (e.g. hybrid beds). We ultimately show how MTDs and transitional flow deposits contribute to reservoir heterogeneity and an overall reduction in effective permeability (e.g. O'Connor & Walker 1993; Garland et al. 1999; McCaffrey & Kneller 2001; Haughton et al. 2003).

Seal evaluation and MTDs

Any evaluation of seal potential needs to focus on three properties: (i) *capacity*, which is related to minimum capillary entry pressure and controlled by pore-throat characteristics, most notably size and connectivity, (ii) *integrity*, which is related to rock ductility and tendency to fracture during deformation, and (iii) *geometry*, which is related to thickness, form, and aerial extent of the unit, and is controlled by depositional environment (Downey 1984; Kaldi & Atkinson 1997). Evidence that MTDs can act as seals is observed at several scales. Seismic-scale sealing MTDs are evident where gas-related bright spots are located directly beneath MTDs (e.g. Berndt et al. 2003; Bünz et al. 2003; Berndt et al. 2012; Sun et al. 2017), and where there is a lack of gas-escape structures (e.g. pockmarks) directly above these deposits (e.g. Sarkar et al. 2012; Riboulot et al. 2013). However, seismic studies focusing on structural fabrics surrounding large (~0.5-5 km wide) rafted blocks suggest these feature may decrease seal integrity (Alves et al. 2014; Gamboa & Alves 2015; Steventon et al. 2019). Second, at the borehole-scale, analysis of petrophysical well-logs, pore fluid pressure, shear deformation, and capillary pressures characteristics all point to MTDs having relatively low permeability (Flemings et al. 2008; Dugan 2012; Yamamoto & Sawyer 2012; Day-Stirrat et al. 2013; Cardona et al. 2016; Wu et al. 2019) (Fig. 1c).

Reservoir evaluation and transitional flow deposits

In relation to reservoir evaluation, small-scale MTDs, thin-bedded turbidites, and transitional flow deposits (e.g. linked turbidite-debrite beds, hybrid beds, and banded beds; see Lowe & Guy 2000; Haughton et al. 2003; Talling et al. 2004) can impart significant heterogeneity within otherwise high-quality turbidite reservoirs. This type of bed-scale heterogeneity is often below seismic and sometimes conventional well-log scales (i.e. cm-dm-scale) and requires image log or core data for effective analysis. Thin-bedded turbidites or simply "*thin beds"*, typically associated with submarine levee, lobe fringe, and basinfloor settings, or sediment bypass-dominated zones (Stevenson et al. 2015), have received much attention in both outcrop (e.g. Mutti 1977; Stow & Piper 1984; Walker 1985) and the subsurface (e.g. Kendrick 1998; Kendrick 2000; Hansen et al. 2017). Thin-beds can contribute significantly to reservoir pay where they are separated by thin mudstones; in other cases they can be mudstone-dominated and act as baffles (Passey et al. 2006). However, considerably less attention has been given to the role of transitional flow deposits (see Haughton et al. 2003; Lowe et al. 2003; Talling et al. 2004). Analysis of transitional flow deposits has focused on their distribution in relation to an idealised lobe complex (e.g. Hodgson 2009; Fonnesu et al. 2015; Spychala et al. 2017b) and their occurrence in confined basins (e.g. Haughton et al. 2009; Fonnesu et al. 2018; Soutter et al. 2019). Studies of transitional flow deposit reservoir quality and their impact on subsurface fluid flow are rarer (see Amy et al. 2009; Porten et al. 2016; Southern et al. 2017).

Aims and significance

Here, we aim to bridge the gap between the potential production impact of shallowly-buried seismically-resolvable MTDs and deeply-buried sub-seismic MTDs and transitional flow deposits, by studying their distribution within an Upper Jurassic turbidite sandstone reservoir in the Magnus Field, northern North Sea (Fig. 2). The Magnus Field is a mature oilfield: discovered in 1974, with first oil production in 1983, and the start of enhanced oil recovery in 2002 (MacGregor et al. 2005). There is an estimated c.1.8 billion barrels of STOIIP, with a predicted recovery factor of 50-55% (Shepherd et al. 1990; MacGregor et al. 2005). We use the comprehensive well-bore and seismic reflection dataset to conduct a thorough analysis of the reservoir's nature, origin, and distribution of physical properties (i.e. porosity, permeability, volume of clay, density/compressional velocity), highlighting the role of sub-seismic MTDs and transitional flow deposits. We focus on three main aims: (i) to capture the stratigraphic evolution of the submarine slope depositional system in the Magnus reservoir, (ii) to characterise the lateral variability of sub-seismic MTDs and assess their impact on fluid flow, and (iii)

to investigate the impact of overlying transitional flow deposits on reservoir quality and fluid flow. Our study has implications for petroleum exploration and production, and the role of MTDs in carbon storage projects, including predicting the distribution of deep-water reservoir-seal pairs, and understanding the impact of heterogeneities on turbidite reservoir connectivity, compartmentalisation, and pore-pressure prediction.

BASIN SETTING & STRATIGRAPHY

Structure

The Viking Graben represents one arm of the northern North Sea trilete rift system, formed through multiple episodes of extension during the Permo-Triassic and latest Jurassic-Early Cretaceous (e.g. Badley et al. 1984; Badley et al. 1988; Yielding 1990). The East Shetland Basin comprises several half-grabens, bound to the east by the Viking Graben and to the west by the Shetland Platform, Unst Basin, and Magnus Basin (Johns & Andrews 1985; Lee & Hwang 1993). The basin has undergone a complex tectono-stratigraphic history, influenced by: (i) Caledonian basement structural grains, (ii) Middle-to-Late Jurassic and Early Cretaceous rifting, associated with the formation of the Viking Graben, and (iii) early Cretaceous rifting and opening of the Magnus and Møre Basins in the North Atlantic (Shepherd 1991; Gabrielsen et al. 1999; Al-Abry 2002). The post-Triassic sedimentary succession of the East Shetland Basin consists of Triassic-Jurassic tilted fault blocks, with syn-rift sedimentation transitioning from shallow marine to deep marine environments (Partington et al. 1993; Morris et al. 1999). The succession can be split into: (i) the Lower Jurassic post-rift shallow marine Dunlin Group (Jurassic sequence (J) 10), (ii) the Middle Jurassic post-rift deltaic Brent Group (J20-30), which included a period of minor fault activity recorded by a top-Rannoch unconformity, (iii) the initiation of Late Jurassic rifting during deposition of the Tarbert Formation, and (iv) deposition of the Upper Jurassic syn-rift shelfal Heather (J30-40) and deep-marine Kimmeridge Clay Formations (J60-70) (Partington et al. 1993; Morris et al. 1999; Dominguez 2007) (Fig. 2, 3, X-X^{l}). These deposits were subsequently truncated during the formation of the Base Cretaceous unconformity (BCU) (Dominguez 2007). During the Cretaceous and Cenozoic, the East Shetland Basin underwent post-rift thermal subsidence, and a ~3.5 km-thick marine succession was deposited in the Magnus area (Partington et al. 1993; Ravnås & Steel 1997).

The Magnus Field is located on the north-western limit of the East Shetland Basin, within the Penguin half-graben, bound to the north-west by the Magnus and End of the World faults (Shepherd 1991; Thomas & Coward 1995) (see inset maps, Fig. 2). The field lies on the crest of a tilted fault block in the footwall of the Magnus Fault, with hydrocarbons trapped by a combination of stratigraphic pinch-

out and truncation below the BCU (Shepherd 1991) (Fig. 3a, b). In the Magnus area, Jurassic to Cretaceous rifting led to the development of: (i) NNW-SSE and N-S-striking arrays of Late Bathonian early syn-rift faults, offsetting the Brent Group (pre-rift) and active during deposition of the Heather Formation, (ii) a WNW-ESE-striking array of late syn-rift faults predominantly in the Heather and Lower Kimmeridge Clay Formations, and later reactivation of the NNW-SSE-striking array of faults, and (iii) NE-SW Atlantic rifting trend in the Early Cretaceous (Fig. 3c, d) (see Al-Abry 2002). Major structures in the Magnus area include: the Brent, Magnus, and the End of the World Faults. The Brent Fault trends NNW-SSE through the Magnus area, with both the Heather and Kimmeridge Clay formations thickening into the hanging-wall of the fault, especially in the southern area of the field (Fig. 3b, c). The Magnus Fault strikes NE-SW to N-S, dipping to the NW, and contains a fault scarp degradation complex in its footwall (e.g. Underhill et al. 1997). The End of the World Fault strikes NE-SW and dips to the NW, bounding the northern area of the Penguin half-graben (Al-Abry 2002) (Fig. 2, inset maps).

Magnus Field Reservoir Stratigraphy

The Magnus Field reservoir is contained within the Upper Jurassic Kimmeridge Clay Formation, comprising (bottom to top) (Fig. 2): (i) the Lower Kimmeridge Clay Formation (J50-62) composed of a turbidite and clastic injectite system (see Goodall et al. 1999), (ii) the Magnus Sandstone Member (MSM, J63-64), composed of a sand-rich turbidite system, and (iii) the Upper Kimmeridge Clay Formation (J66-70), composed of hemipelagic mudstones (Partington et al. 1993; Morris et al. 1999; Fraser et al. 2002) (Fig. 2, 3b). The MSM (the focus of this study) comprises (bottom to top) (Fig. 3e): (i) the lower MSM reservoir (MSA), (ii) a basin-wide mud-rich unit, MSB, which is related to *Autissiodorensis* maximum flooding surface, (iii) the upper MSM reservoir, which can be subdivided into sand-rich (MSC, MSE, MSG) and mud-rich (MSD, MSF) units (MSF is marked by *Iathetica re-influx*), and (iv) a transition into the Upper Kimmeridge Clay Formation (MSG-MSH), marked by the *Hudlestoni* maximum flooding surface (Partington et al. 1993; Morris et al. 1999). Two main depositional trends are observed: (i) a lower reservoir trend (MSA) deposited within a centrally fault-controlled depocentre, and (ii) an upper reservoir trend (MSC-H) with a southern depocentre in the footwall of the Brent Fault, and a northern depocentre onlapping the Brent Fault footwall high (Fig. 2) (Ravnås & Steel 1997; Morris et al. 1999; Al-Abry 2002).

DATA & METHODS

We use a 3D seismic-reflection survey and 83 wells, containing petrophysical well-logs, biostratigraphic tops, and fluid pore pressure data (see Supplementary Material). This included 33 wells with core photos, of which five were available for physical core logging (see Fig. 2a for locations).

Core and wireline petrophysics

Detailed sedimentological core logging (1:10 scale, i.e. 1 m = 10 cm) of the MSB and surrounding lower (MSA) and upper (MSC) MSM reservoir units was undertaken on five wells, covering a combined stratigraphic thickness of 238.5 m (see Fig. 2 for well locations). Data collection comprised lithology, grain-size, bed thickness, type of bed contacts, and primary sedimentary structures and (secondary) soft sediment deformational structures. QEMSCAN© (quantitative evaluation of minerals by scanning electron microscopy) was used to quantify the grain size and shape, textural information, mineralogy, and porosity distribution for 14 core samples from well 211/12a-M16, located in the central area of the field (Fig. 2a). The QEMSCAN platform is a scanning electron microscope (SEM) with energy dispersive x-ray (EDS) detectors and provides automated petrographic quantification of spatially resolved compositional and textural data. For this study, the data were collected by Rocktype Ltd using a QEMSCAN® WellSite instrument (Aspex Extreme Scanning Electron Microscope with 5030 Bruker EDS detectors) using the FieldScan mode at 15 kV beam energy and 10 μm stepping interval. Details of the microscope set-up can be found in Supplementary Material. QEMSCAN samples (QM1 to QM14) were taken from reservoir units MSA, MSB, MSC, and MSE (see Fig. 4).

In addition to physical core, a full suite of wireline logs, pressure, and core analysis data were available (see Supplementary Material). Core plug measurements of porosity, horizontal permeability (Kh) and vertical permeability (Kv) were used to define flow units. Fluid pressure data (repeat formation tests) was also used to identify internal pressure breaks within the reservoir, which may reflect the presence of structural or stratigraphic barriers. Well-log-based reservoir zonation and correlation of maximum flooding surfaces to subdivide the primary Magnus reservoir units (MSA-H) was guided by biostratigraphic reports from EnQuest and BP, along with published biostratigraphic schemes (see Partington et al. 1993; Morris et al. 1999, Supplementary Material).

Seismic interpretation

The 3D pre-stack depth migrated seismic-reflection (ocean bottom cable) survey used in this study covers a *c.* 178 km^2 area, imaging the tilted fault block containing the Magnus Field. The data are SEG reverse polarity (i.e. European polarity, with an increase in acoustic impedance = trough), zero-phased, and have a lateral bin spacing of 12.5×12.5 m and a vertical resolution (assumed to be tuning thickness, 1/4 of the dominant wavelength) of *c.* 12 m at 3 km. We interpret three seismic horizons within and

surrounding the Magnus reservoir: (i) the top Heather Formation (ii) the MSA/MSB boundary, and (iii) the BCU. In addition, a coloured inversion cube was available that allowed further analysis of the lateral variability of the depositional systems (for method see Lancaster & Whitcombe 2000).

The sand-rich reservoir sections are predominantly characterised by high-amplitude, positive (SEG-reverse polarity) reflections, related to an interface from higher-density background sediments to hydrocarbon-filled lower-density ("soft") sands. This equates to sand-rich reservoir zones being characterised by negative acoustic impedance responses (Fig. 3a). Note that amplitude maps are only extracted up to the vertical resolution of the seismic data (c. 12 m).

SEDIMENTOLOGY OF RESERVOIR SANDSTONE FACIES

This core-based sedimentary facies analysis is focused on the MSA, MSB, and upper (MSC to MSH) units of the MSM reservoir (see Fig. 2, 3e). Seven facies types have been recognised: (i) thick-bedded sandstones (F1); (ii) thin-bedded sandstones (F2); (iii) banded heterolithic beds (F3); (iv) hybrid beds (F4); (v) heterogeneous deformed beds (F5); (vi) mudstones (F6); and (vii) heterogeneous argillaceous beds (F7) (see Table 1, Fig.5).

Turbidite deposits

Facies 1: Thick-bedded sandstones (high-density turbidites)

Description: Fine- to coarse-grained, 0.2-1 m-thick amalgamated sandstone beds with predominantly massive or planar laminated internal features (Fig. 5, F1). Normal grading fine sand to silt is observed at bed tops, associated with current ripple and planar laminated bed tops (see Facies 2). Intercalated mudclast-rich horizons (~0.5-2 m thick) (Fig. 5, F1) comprise angular and/or sheared clasts (<1-8 cm diameter). Intermittently preserved medium- to granule-grade sandstones (0.05-0.25 m thick), with matrix- and grain-supported intervals display erosive bases, weak normal grading, and poorly developed imbrication of quartz, lithic, and mudstone clasts (Fig. 5, F1).

Interpretation: The massive to planar laminated sandstone beds, are interpreted to have been deposited by high-density turbidity currents, with rapid deposition and bed aggradation suppressing tractional bedform development (Lowe 1982; Kneller & Branney 1995). The basal sandstones with erosive bases are interpreted to be formed by tractional processes at the base of high concentration turbidity currents, with the coarsest-grained material deposited first (e.g. Walker & Mutti 1973; Lowe 1982). Mudclast-

rich horizons are interpreted to represent lag deposits and represent locations dominated by sediment bypass (Stevenson et al. 2015).

Facies 2: Thin-bedded sandstone (low-density turbidite)

Description: Very fine- to fine-grained, c. 0.05-0.2 m-thick sandstone beds, showing normal grading, current ripple cross-lamination, including climbing sets, convolute lamination, and planar-parallel lamination (Fig. 5, 6k). Typically, sandstone bed bases are sharp and planar to weakly erosional, and bed tops may be sharp or normally graded. The sandstones can occur in either: (i) sets of thin bedded sandstones interbedded with mudstones (~3 m set thickness), or (ii) as individual sandstone beds above high-density turbidites (Facies 1).

Interpretation: The thin-bedded structured sandstones are interpreted to have been deposited by low density turbidity currents, representing 'classical' turbidites (mainly T_C/$T_{D/E}$ divisions) (Bouma 1964; Mutti 1977; Talling et al. 2012). The climbing ripple sets represent periods of rapid suspended sediment fallout (Fig. 6k) (Jobe et al. 2012).

Transitional flow deposits

Facies 3: Banded beds

Description: This facies is dominated by 5-35 cm-thick sandstones beds that comprise alternating dark and light, cm-scale, parallel to sub-parallel bands (Fig. 5, F3). The light bands can be planar and current ripple cross laminated and are sand-rich. Dark bands have elevated amounts of mud, and are less well sorted, but with similar maximum grain-size to the light bands (Fig. 5, F3). The upper contacts of banded beds record a sharp grain size break into an overlying mudstone.

Interpretation: Banded turbidite sandstone beds and bed divisions have been reported in the North Sea (e.g. Lowe & Guy 2000; Haughton et al. 2009; Stevenson et al. 2020), however, the process of deposition is still under debate. Lowe & Guy (2000) proposed a model of cyclic freezing of a near-bed plug flow, and postulate that banding forms between turbulent and laminar flow states, through variations in near-bed clay content modifying flow cohesion from low (sands-silt bands) to high (clay-rich bands). However, flume tank experiments suggest flows with migrating bedforms within the upper stage plane bed flow regime can also produce banded beds (see Baas et al. 2011; Baas et al. 2016). Stevenson et al. (2020) provide a thorough review of banded turbidite sandstones, and supports the Baas model for banded sandstones of the scale observed here.

Facies 4: Structured argillaceous sandstones (hybrid beds)

Description: This facies comprises of approximately 15-40 cm thick bipartite beds with lower fine- to medium-grained sandstone divisions, and upper argillaceous sandstone division (Fig. 5, F4). The lowermost sandstones are well-sorted and appear as either: (i) normally graded to ungraded sandstones, with basal loading structures and sheared mudstone clasts at the base, dewatering pipes, and mudclasts/chips concentrated at the top or (ii) weakly laminated to banded sandstones (Facies 3) with sharp to slightly wavy bases. The overlying argillaceous sandstone division often has a sharp, loaded or variably deformed contact, sometimes with sand injection, and can contain outsized granules, highly sheared mudstones clasts, and dispersed quartz grains forming a 'starry night' appearance (Fig. 5). A sharp contact usually marks the base of thin (mm-cm-scale) parallel laminated to current ripple cross-laminated sandstones, followed by a thin mudstone cap.

Interpretation: Beds comprising lower sandstone divisions overlain by argillaceous sandstones are interpreted as turbidites with linked debrites (sensu Haughton et al. 2003), whereby the lower division represents a sandy turbidite and the upper argillaceous division a muddy debrite (Haughton et al. 2003; Talling et al. 2004). Overlying graded beds might represent low-density turbulent flow/wake deposits (Haughton et al. 2009). The beds conform well with Haughton et al. (2009) five part classification scheme (H1-5), albeit sometimes lacking rippled sandstones and mudstone caps. Hybrid beds may be attributed to sediment gravity flow transformation (Fisher 1983), with flow concentration increasing with runout distance of a turbidity current related to entrainment of substrate, or the partial transformation of an initial debris flow (e.g. Haughton et al. 2003; Sumner et al. 2009; Hodgson 2009; Fonnesu et al. 2015; Kane et al. 2017).

Facies 5: Deformed-remobilised "slurry" beds

Description: This facies comprises beds of fine-grained, light-grey sandstones and siltstones, and dark-grey mud-rich sandstones. Individual beds are 0.25-0.7 m thick, with irregular basal contacts (Fig. 5, F5). The heterolithic alternations display soft sediment deformation, including ball and pillow structures, folded and sheared fabrics, and sheared/injected mudstone horizons (Fig. 5, F5). The beds show a similar trend to the hybrid beds, with a lower cleaner sandstone division overlain by a more argillaceous division. The beds are commonly associated with banded beds (Facies 3). However, these "slurry" beds are different to hybrid beds (Facies 4) because they show: (i) gradational changes between sand- and mud-rich facies with poorly developed debritic textures, and (ii) may be chaotic or unstructured.

Interpretation: The chaotic sheared nature of the beds and syn-sedimentary soft sediment deformation structures suggest downslope movement of a heterolithic unit that was partially liquefied. The common

occurrence above or below banded beds suggested a link between Facies 3 and 5. Therefore, we interpret the facies to represent remobilised banded sandstone beds which were transported farther downslope. This facies is similar to the "mixed slurry flows" described from the Britannia Field (Lowe & Guy 2000), where the facies are interpreted to be deposited initially as banded beds, which were later remobilised as water-rich heterolithic mixtures (Barker et al. 2008; Eggenhuisen et al. 2010).

Mudstone deposits

Facies 6: Mudstones

Description: Massive to parallel laminated (mm-scale) mudstones and siltstone beds, with sharp contacts and normal grading profiles (based on colour change). Bed thicknesses are variable (from 0.2->1 cm).

Interpretation: We interpret that these mudstones were deposited by either: (i) suspension settling of very fine-grained, pelagic and hemipelagic sediments in a very low-energy environment; and/or (ii) from mud-rich dilute turbidity currents (Stow & Shanmugam 1980; Boulesteix et al. 2019).

SEDIMENTOLOGY OF MTD FACIES

Overview of the MSB unit (Facies 7)

Facies 7 forms a 1-18 m-thick unit that constitutes the entirety of the MSB unit (Fig. 4b, 7a). Three sub-facies are recognised, based on varying clay concentrations: (i) light-coloured and sand-rich (VSH<25%, D1); (ii) grey to dark-grey coloured and mud-rich (VSH 25-50%, D2-D4), and (iii) brecciated (D5) (see Table 2). We here describe these units in details, along with nature of their bounding surface and the overall lateral variability within the MSB, before interpreting the formative physical processes and environment.

Sub-facies types

Sub-facies D1 (sand-rich debrites)

Description: Light-grey muddy sandstones, predominantly composed of fine to very coarse grained sand, with both clast- (Fig. 7c) and matrix-supported (Fig. 6a) areas. Clast are mudstone and sandstone,

and sub-rounded to angular, with sheared and/or squeezed fabrics (Fig. 6a). Intact clasts of bedded sediments are smaller than Facies D2-4 (<60 cm) and composed of mudstones with only minor disaggregation of original bedding (Fig. 7c).

Sub-facies D2-4 (mud-rich debrites)

Description: Matrix-supported sandy mudstone with "floating" grains (fine to coarse sand grade). The colour of the poorly sorted matrix varies from grey (D2-3, VSH=25-50%) to dark grey (D4, VSH=>50%) with increased clay content (Fig. 6b-d). A 'starry night' matrix texture is composed of predominantly granule to pebble-grade clasts of quartz, mudstones, belemnites and carbonaceous material, supported within the mudstone matrix (Fig. 5, D2-4, Fig. 6b-d). Belemnites are commonly found near the base of MSB (Fig. 7b, d). Small clasts (<7 cm diameter) within the matrix are predominantly dark mudstones, which are either sub-rounded to angular, or sheared and aligned parallel to bedding (Fig. 4b, 6b, 7, D2-4,). Larger intact bedded and disaggregated clasts (up to 1.5 m thick) are observed throughout the unit (Fig. 7c, g), which are locally overturned (including Facies 1, 2, 3 and 6). Some of the larger clasts are composed of clean sandstones with angular edges (e.g. top of Fig. 7g) that are not oil stained, while others display sheared/squeezed fabrics and soft-sediment deformation (e.g. Fig. 7f). The clasts can be distinguished from regular bedded sediments by: (i) irregular, disintegrated, or sheared contacts, (ii) incorporation of poorly sorted mud-rich matrix into clasts, and (iii) juxtaposition of clasts of different facies (e.g. Fig. 7f). Structures within the unit include soft-sediment deformation, microfaulting, injections, sheared clasts oriented mostly parallel to bedding, and sheared fabrics in the matrix (Fig. 5, 6, 7).

Sub-facies D5 (discordant sandstones and brecciated mudstones)

Description: Facies D5 is composed of a chaotic mixture of: (i) mudstones, (ii) sandstones, and (iii) mudstone-sandstone breccia. The mudstones form the main lithology, exhibiting bedded intervals, with planar and irregular contacts, folded and deformed intervals, and chaotic intervals disrupted by sandstones (Fig. 7j). The sandstones are very fine- to fine-grained, light grey, and discordant to the primary mudstone bedding (Fig. 6e, 7j). The contact between sandstone and mudstone is sharp and sometimes ptygmatically folded, or irregular, with sheared mudstone clasts at contacts and sandstone grains incorporated into the surrounding mudstone (Fig. 7j, k). The mudstone-sandstone breccia consists of angular to sub-angular sandstone clasts within a mudstone matrix (Fig. 6e). Clasts range in size from 15 to <1 cm, with contacts between the mudstone and sandstone sharp (Fig. 6e).

MSB bounding zones

418 The basal surfaces of the MSB unit display either thin (<10 cm) zones of intense deformation or sharp
419 contacts with the underlying substrate. Updip the basal contact is characterised by a sharp contact with
420 small-scale injection dyke structures where a sand-rich debrite (D1) in MSB overlies a high-density
421 turbidite in MSA (well M12; Fig. 7b). Downdip to the SE in well M16 the basal shear zone is
422 characterised by an erosively-based, 10 cm-thick, highly sheared mud-rich debrite (D2) overlying a
423 high-density turbidite in MSA (Fig. 4b, 7d). Sharp contacts between the underlying MSA sandstone
424 turbidites and the MSB mud-rich debrites (D3) are observed farther downdip (well M1 and 12a-11, Fig.
425 7h, o).

426 The top of the MSB unit is marked by an abrupt change from debrites or mudstones into banded, hybrid
427 and remobilised beds of the MSC unit (see Fig. 4b, 6). In well M12, there is a sharp contact between
428 MSB mudstones and thicker (~2 m) MSC remobilised beds (Fig. 6f). Above this, high-density turbidites
429 dominate the upper reservoir zone. Well M16 displays a sharp contact between mudstones, and
430 overlying banded beds that pass upwards into remobilised beds (Fig. 6g, h). Well M1 displays a sharp
431 contact between mud-rich debrites (D4) and banded beds, which pass gradually upwards into high-
432 density turbidites and hybrid-beds (Fig. 6i). The contact in well 12a-11 is not preserved in core, but the
433 facies changes from mudstones to high-density turbidites. In the northern area of the field, well 211/7-
434 1 comprises 8 m of interbedded Facies D5 and turbidite facies 1 and 2 (Fig. 6j, k, l).

435

436 *MSB lateral variability*

437 The MSB-unit is lithologically variable across the Magnus field. In the central and southern areas of
438 the field, the MSB unit is predominantly characterised by a sandy mudstone matrix (Facies D1-4). The
439 isopach thickness map of MSB broadly follows the outline of MSA isopach (Fig. 7a, 15b). A change
440 from sand- to mud rich debrite facies is observed between well 12a-9 and M12 (Fig. 9a). MSB is
441 interpreted to pinch-out between M12 and 12-a14, located in the footwall of the Magnus Fault (Fig. 9a).
442 In the northern area (e.g. well 7-1, Fig. 6e), the MSB is dominated by brecciated and injection fabrics
443 (Facies D5), with an absence of Facies D1-4. In this area the MSB can also be correlated between wells
444 7-1 and 7a-3 (~420 m), thinning towards 7a-6 (Fig. 9c).

445

446 **MSB-unit Interpretation**

447 The facies characteristics, together with the deformation features at its base, suggest that the MSB is a
448 debrite. The basal deformation in some parts of the central and southern areas support interpretation of
449 a basal shear zone (see Butler et al. 2016; Hodgson et al., 2019). Elsewhere, the basal shear is expressed
450 as a sharp surface. The absence of internal bounding surfaces or consistent changes in character suggest
451 that the unit was transported and deposited *en masse* as a dominantly cohesive debris flow in a single

event, having sufficient yield strength to enable >1 m diameter 'rafted' block/clasts to be transported. The larger blocks were likely incorporated from either the source area or substrate entrainment during transport based on, (i) over-turned, folded or anomalous bedding or lamination dips, (ii) irregular contacts between blocks and debritic matrix, or (iii) incorporation of debritic matrix streaks or inclusions into the blocks. The change in facies downslope from sand-rich (Facies D1) (e.g. well M12, Fig. 6a), to mud-rich debrites with higher clay contents (e.g. well M1, Fig. 6d), may represent a longitudinal flow evolution to a more cohesive debris flow; as grains become increasingly disaggregated and mixed into the matrix, increasing the yield strength of the flow (Fig. 6). As the yield strength increased, larger clasts could be supported by the debris flow (e.g. Hampton 1975; Talling 2013). This distribution supports a transport direction towards the SE (i.e. from well M12 to M1, Fig. 7a). The trend from sand- to mud-rich debrite facies (D1-4) in the central and southern areas suggests a minimum runout distance of ~3.7 km between well 12a-9 and M12 (Fig. 9a).

The character of the MSB unit in the northern area is markedly different (Facies DB) when compared to the debritic textures (Facies D1-4) in the central (e.g. well M16) and southern (e.g. well 12a-11) areas. Observations of discordant sandstones, brecciation, and soft sediment folding in Facies D5 suggest formation through hydraulic fracturing and injection processes (see Koša 2007; Satur & Hurst 2007), and minor remobilisation through slumping (Fig. 6e, 7j), rather than a debris flow. This suggests Facies D5 was either: (i) detached from the main central and southern debris flow; (ii) represents a separate failure event or the injected margin of the MSB debrite; or (iii) that the MSB was either very thin or not preserved in the northern area and D5 represents the boundary between the MSA and MSC.

Clay content is a controlling factor in the strength of a debris flow, with highly cohesive flows resistive to mixing with the ambient seawater, and prone to hydroplaning (Mohrig et al. 1998; Talling 2013). The character of the basal shear zone in the central and southern areas of the Magnus Field, suggests more erosion updip with lower clay content in the overlying deposit (i.e. Facies D1-2, Fig. 6b,d). The sharper basal contact downdip (wells M1 and 12a-11 (Fig. 7h, o)) could suggest less erosion with higher clay contents in the overlying deposit (i.e. Facies D3-4, Fig. 7h). This may support a debris flow transported from the NW that was able to erode into a likely unlithified/semi-lithified substrate (primarily MSA reservoir unit), which evolved longitudinally into a highly cohesive debris flow that was prone to hydroplaning. Hydroplaning, enables debris flows to detach from the underlying substrate, and to bypass with limited or no transmission of shear stress beneath the flow (see "free-slip flows" Sobiesiak et al. 2018). Field studies of similar sized deposits (i.e. 10's m thick) show debrites can have heterogeneous basal zones including sharp, discordant, and erosive contacts (e.g. Auchter et al. 2016).

PETROPHYSICS & PETROGRAPHIC ANALYSIS

Petrophysical properties of the MSM

Here, we build on the core facies analysis outlined above by using well-log and biostratigraphic data to correlate the lower reservoir (MSA), intra-reservoir MTD (MSB), upper reservoir (MSC, E, G, & H), and mud-prone units (MSD & F) across the Magnus Field, thereby establishing their spatial distribution and thickness (Fig. 8, 9).

Lower reservoir (MSA)

The lower reservoir (MSA) is characterised by predominantly low gamma-ray (GR) values (<75 gAPI), indicating low volumes of shale (<1% average, derived from GR logs), and a neutron-density cross-over consistent with high-density turbidite sandstones (Facies 1) observed in core (Fig. 8a). The compressional (p-wave) velocity (i.e. sonic log) is approximately constant (c. 80-100 µs/ft) across the interval, and the high resistivity (c. 25-270 Ωm) and oil saturation (0.79, derived from resistivity in well M16) is consistent with oil staining observed in the core (see fluorescence emission in Facies 1, Fig. 5). Breaks in these responses are rare and interpreted to represent the transitions between turbidite packages, characterised by higher gamma-ray values and limited separation between neutron-density (see Fig. 8a). These breaks correlate with the mudclast-rich intervals identified from core in Facies 1 (Fig. 5). The responses are consistent with an interpretation of predominantly amalgamated high-density turbidites in the central area of the field (Fig. 9a). Away from the central trend of the field (i.e. Fig. 9a), log values become more variable with increasing GR values (>75 gAPI), and neutron-density cross-overs (e.g. M1 and M2, Fig. 7a, 9e). Calibrating these responses with core shows that variable responses in MSA can be attributed to thin-bedded low-density turbidites (Facies 2) and background mudstones (Facies 6) (see Fig. 7r). Core plugs from high-density turbidites (Facies 1) display an average porosity = 22%, average vertical permeability (Kv) = 500 mD, and average horizontal (Kh) permeability = 600 mD.

Intra-reservoir seal (MSB)

The MSB is characterised by relatively high (>75-250 gAPI) gamma-ray values, related to high volumes of clays within the debrite matrix of Facies 7 (Table. 2). However, the petrophysical expression of MSB can vary depending on well location, with updip wells (e.g. M16 & M12, Fig. 9a) characterised by an upwards increase in GR (75->150 gAPI), and downdip wells by a more consistent GR response (e.g. >125 gAPI, M1 & M8z, Fig. 9a). We attribute the distal expression to reflect increased mixing of clays

519 with increasing transport distance (Fig. 6a-d). Neutron-density cross-overs reverse when compared to
520 the MSA, suggesting a predominantly clay-rich unit. Compressional velocities show an irregular
521 signature, and resistivity values (1-2 Ωm) are less than in MSA, likely related to a combination of no
522 hydrocarbon saturation, and increased saturation of conductive brine and clay minerals. However, there
523 are resistivity peaks (c. 10 Ωm) in the basal zone of MSB, which are similar to those seen in studies of
524 more shallowly buried MTDs in other basins (e.g. Sawyer et al. 2009).

525

526 *Upper reservoir (MSC, E, G, & H) and mud-prone (MSD & MSF) units*

527 The upper reservoir sand-rich units (MSC, E, G, & H) are similar to MSA, with generally low GR
528 values (45-80 gAPI), and neutron-density crossings consistent with sandstones. However, this
529 expression can be more variable, likely related to more variable facies (i.e. Facies 3, 4, and 5) when
530 compared to the high-density turbidite-dominated lower reservoir (MSA). The upper reservoirs can be
531 interpreted as three turbidite-dominated sequences, split by zones of increased clay content (MSD and
532 MSF). MSD/F are characterised by elevated GR (c. 100 gAPI), and reduced resistivity responses (c. 4
533 Ωm). Core data show MSD and MSF are dominated by hybrid, banded, and remobilised beds, and low-
534 density turbidites, which are likely more conductive than high-density turbidites; this explains the
535 observed reduction in resistivity. MSF can be correlated across the basin, and its top coincides with the
536 *Iathetica re-influx* (Partington et al. 1993), whereas MSD is discontinuous across the basin. Low-density
537 turbidites contribute little to the primary reservoir and in cases are not oil-stained (core Φ = 15%, Kv =
538 ~400 mD, Kh = ~575 mD), suggesting they are isolated from the main reservoir. Core plug samples of
539 the H1 intervals of hybrid-beds, show these deposits have good porosity (16-24%) and moderate
540 permeability (Kh = 20-200 mD). Banded beds (Facies 4) near the basal section of the upper reservoir
541 (Fig. 6g, i) show more varied, typically lower porosities (>1-24%) and permeabilities (Kv = ~0.27 mD;
542 Kh = ~21 mD).

543

544 **Fluid pressures: temporal and spatial variability**

545 Formation pressure in the Magnus reservoir is known to be highly variable due to sealing faults and
546 clay-rich laterally extensive deposits (Atkinson 1985; Shepherd et al. 1990; Morris et al. 1999). Initial
547 reservoir pressure was 6635 psi, at 3050 m, with a gradient of 0.67 psi/ft (Shepherd 1991). Figure 10d
548 details the production history of the field and the operational timescales of the wells discussed below.

549 In early production wells, repeat formation tester pressure data display marked pressure breaks between
550 the upper and lower reservoirs (Fig. 10a). For example, in well 211/12a-M1, the upper reservoir pressure
551 gradient (0.34 psia/ft) follows a linear trend until the top of MSB (Fig. 10a). The lower reservoir
552 pressure measurement increase significantly above a linear trend from the upper reservoir gradient. This

major pressure break (430 psia) suggests that MSB is acting as a barrier, compartmentalising the upper and lower reservoirs (Fig. 10a). Similar trends are also observed in other early production wells, with ranges in pressure breaks varying from 1984 psia in well M4, to 377 psia in well M12 (Fig. 10a). Mid-production wells show much lower pressure breaks (e.g. 22 psia in well M16), in effect following the upper reservoir pressure gradient, and in many late infill wells a negative pressure differential (e.g. M31z -1976 psia) is observed between the upper and lower reservoirs (Fig. 10b).

This variability in pressure change (Δp) can be related to oil field management and operational activities (i.e. production and water injection, EnQuest Internal Report), and sealing faults that may serve to laterally compartmentalise the reservoir. There was an initial increase in the Δp trend (wells M1 to M5) related to rapid depletion of the upper reservoir prior to the full field-wide impact of water injection (Fig. 10b), pressure differences within the reservoir is represented by variable Δp values between wells M5 to M12 (Fig. 10b). The later negative Δp (wells M30 to M41) can be related to significant water injection into the upper reservoir, and limited water injection into the depleting lower reservoir during mid to late production (EnQuest Internal Report). No correlation between Δp and MSB thickness was found, suggesting MSB variability (within the areas sampled) has little impact on the unit's ability to act as a competent barrier on production timescales (Fig. 10c). Therefore, we can confidently infer that the MSB unit is acting as a fluid flow barrier across >7.5 km of the field. However, fluid pressure data in wells to the north (i.e. 7-1 and 7a-3) do not sample below MSC, therefore we cannot confirm whether or not the MSB (i.e. Facies D5, Fig. 6e, 7k) is sealing in this area. Overall, the pressure differentials suggest the MSB is a competent barrier in the central and southern areas of the field.

Vertical changes in formation pressure are also observed around MSF, which acts as a local pressure barrier (Fig. 10a). For example, wells M4, M9 and M16 show negative pressure breaks (-201, -242, and -10 psia respectively) between MSG and MSE (Fig. 10a). MSD also records vertical changes in formation pressure. However, breaks are not observed consistently, which we interpret to be related to the heterogeneity of facies (i.e. Facies 2, 3, 4 and 5) within MSF and MSD. In addition, pressure breaks are not observed in initial production wells (e.g. M1, Fig. 10a) suggesting that they are related to differential pressure depletion between zones of the upper reservoir during production, rather than virgin pressures (e.g. M16, Fig. 10a). In addition to the defined reservoir zones of the Magnus Field (see Fig. 3e) formation pressure plots also show intra-zone pressure breaks, which correlate with smaller sub-zones dominated by mudstones or transitional flow deposits (Fig. 10a). These variable pressured sub-zones also validate observed preferential water breakthrough along highly permeable sandstones during early production wells (see well M4, Fig. 10, EnQuest Internal Report).

Petrographic properties of the MSM

Core porosity (ϕ) and permeability (vertical K_v or horizontal K_h) cross-plots can help identify flow units within a reservoir (Fig. 8b). However, in reservoirs such as the MSM, with c. 60-85% sandstone, there is obviously a distortion in the dataset with respect to core plug samples (Fig. 9). Thus data are skewed towards sandstone-dominated units, transitional flow deposits (Facies 5, 4, & 5) are underrepresented, and debrite samples (Facies 7) are absent.

We therefore used QEMSCAN to quantify the difference in mineralogy, grain size, and porosity of facies sampled from well 211/12a-M16 (Fig. 2). In addition, QEMSCAN also allows analysis of depositional textures, particularly useful for debrites. Fourteen samples were collected (QM1 to QM14, see Fig. 4a for depths). Sample QM10 recorded scanning errors due to sample damage, thus its results are considered unreliable (see Fig. 14a). The grain-size distribution in QM6 is also artificially skewed towards the coarser end of the grainsize spectrum as some grain-grain contacts could not be resolved by the image-processing software (Fig. 13). The field of view in the mineral maps (QEMSCAN images) is approximately 2×2 cm (Fig. 11 & 12). The data is 2D and hence permeability cannot be quantified. An index of core images showing exact sample depths of QM1-14 can be found in the Supplementary Material.

Mineralogy

Using a quartz-feldspar-lithics ternary plot, MSM samples fall within the sub-arkose, arkose, lithic arkose, and feldspathic litharenite categories (Fig. 14b). Lithics were calculated by summing all other mineral percentages excluding clays, which are predominantly authigenic (e.g. kaolinite and illite) (see Fallick et al. 1993). Quartz is the dominant detrital mineral (c. 20-60%), apart from QM9, which sampled a mud-rich debrite with c. 30% illite. The high-density turbidite samples (QM6 & 14) and the hybrid-bed basal sandstone (QM12) (Facies 1, 2, & 5), plot within the arkose to sub-arkose category. All have low (<10%) amounts of lithics. Debrites (QM5, 7, 9), and the banded bed (QM8) samples, all display a high proportion of lithics spanning the lithic arkose to feldspathic arenite categories. Diagenetic clay overgrowths are present in all turbidite samples, but are generally minor (e.g. 1.85% illite, QM1), increasing in proportion when grain size decreases (e.g. c. 6% illite, QM4), with samples displaying pore-bridging illite fabrics (see QM2, Fig. 11). In the basal hybrid bed sandstone, clay content increases upward accompanying a transition from H1-to-H3 (QM12, Fig.12, Fig.5) (see Haughton et al. 2009). Heavy mineral content (zircon, iron oxides, and apatite) shows no distinct change or trend between the lower (QM1-4), MSB (QM5-9), and upper reservoir (QM11-14).

Grain-size distributions & reservoir quality

Grain size distributions were extracted from QEMSCAN images. Our samples span a range of grainsizes, from 1-20 μm (clay-silt) to >1000 um (very coarse sand). Distributions can appear skewed towards coarser or finer populations or may approximate a normal (gaussian) distribution (Fig. 13). As expected, high-density turbidites (Facies 1) show a skew towards coarser (>125 μm) grain size populations (QM1-4, Fig. 13). There is, however, some variability depending on precisely where in the bed the sample comes from (e.g. QM11 vs. QM1, Fig. 13). QM11, which is taken from the base of a bed, displays a significant coarse-grained skew, with most of the grains >250 μm, whereas samples from middle and upper parts of turbidite beds have normal distributions (e.g. QM13, Fig. 13). A low-density turbidite sampled by QM14 shows a fine-grained skew, with silt and very fine sand dominating the sample. The hybrid-bed (H1) shows a finer skew than high-density turbidites, with no sand grade over medium (QM12, Fig. 13). QM12 also shows a distinct normal grading, increasing in fines towards the top of the sample (Fig. 12). The banded bed sample shows a similar trend to QM14, with distinct grain size breaks visible in the mineral maps (QM8, Fig. 12). The MSB debritic matrix demonstrates a broadly normal distribution of grain sizes in samples QM5 and QM7, with the grain size ranging from coarse sand to clay-silt grade material. QM9 samples the mud-rich debrite part of MSB, showing an increase in clay-silt grade material, and imbricated/shear fabrics (Fig. 12).

Clay content is defined by a combination of the percentage of glauconite, illite, chlorite, kaolinite, smectite, and other secondary clays (see Supplementary Material). Total clay versus total porosity demonstrates a strong, positive relationship (R^2=0.84). High porosity (17-26.5%) and low clay content (<10%) characterise the high-density turbidite samples, consistent with the primary reservoir facies (Fig. 14a). In the thin-bedded turbidite sample (QM14), detrital and diagenetic clays exceed 40%, reducing porosity to <5% and rendering them ineffective reservoirs. The hybrid-bed sample (QM12) clay content is elevated when compared to high-density turbidites, with a porosity of c. 15%; such deposits may therefore still contribute to net pay (Fig. 14a). Core porosity and permeability measurements from hybrid beds demonstrate they may act as reservoirs in the cases of the lower most sandstone divisions (H1) (*c.* Φ = 20%, Kh = 200 mD), with debritic divisions (H3) acting as baffles (*c.* Φ = 9%, Kh = 10 mD). Debrites and banded beds show high clay fractions (>37%), and low total porosities (<10%), and likely insignificant effective porosity, with connectivity between pore throats limited (Fig. 13, 14a). It must be noted that the sample dataset is small and spatially restricted to well M16. Therefore, these data show the potential of using QEMSCAN methods to characterise reservoir quality, but more samples would be needed to draw field-wide trends.

SEISMIC ANALYSIS OF THE MSM RESERVOIR

Seismic facies analysis of the MSM reservoir supports a slope to basinfloor environment, which is consistent with previous studies of the Magnus Field (e.g. Shepherd et al. 1990; Ravnås & Steel 1997). This is illustrated in the context of two seismic units: (i) the lower reservoir (Top Heather to Base MSB interval), and (ii) the upper reservoir (Base MSB to the BCU interval) (Fig. 2).

Lower reservoir

The lower reservoir comprises the MSA plus Lower Kimmeridge Clay Formation (Figs. 2 and 3) and is defined by a centrally located depocentre (up to 285 m thick), which is partially confined by WNW-ESE striking faults, and the N-trending Brent Fault High (Fig. 15). The updip (i.e. to the NW) edge of this interval is characterised by a narrow isopach thick, whereas downdip it thickens into a broader depocentre (Fig. 15b). The downdip (i.e. to the SE) thickening of the MSA in the central area coincides with an increase in the proportion of high density turbidites (c. 20 m to >150 m, Fig. 9a), whereas thinner sequences characterise southern and northern areas (c. <25 m, Fig. 9b, c). The WNW-ESE striking faults do not offset the MSA reservoir, but instead tip-out in the Lower Kimmeridge Clay Formation, with stratal thickening into the faults. Hence, these faults were not active, but formed an irregular topography that shaped the distribution of the MSA (Fig. 15a). The seismic character of the MSA displays a clear updip to downdip transition. The updip area comprises a confined (650 m wide), continuous, high-amplitude and low acoustic impedance reflection (Fig. 15a, X-X'). This reflection exhibits a mounded geometry with positive relief, reflecting differential compaction around sandstone-rich fairways (i.e. wells M12 and M16, Fig 9a). Further downdip, the MSA reflection initially widens (c. 1.5 km) (Fig. 15a, Y-Y') and then transitions into two reflections with high-amplitude and high continuity in the central area and lower amplitude and thinning to the north and south (Fig. 15a, Z-Z'). Amplitude extractions taken from the top MSA show the distribution of the reservoir, imaging a centrally confined channel form in an inferred upper to mid-slope position, expanding downdip into a lobate geometry (c. 10.25 km^2) (Fig. 15b, -30 m offset). The system then backsteps up the slope, until there is no reservoir amplitude response, marking the boundary with the mud-prone MSB (Fig. 15b, -10 m offset). The gross geometry of the MSA is consistent with the petrophysical and core analysis, which shows a predominance of high density turbidites in the central MSA fairway area, and more mud-rich thin-bedded turbidites (Facies 2), injectites, and background mudstones (Facies 6) farther downdip and along strike (i.e. northern and southern areas).

686 **Upper reservoir**

687 The upper reservoir comprises the upper MSM (Base MSB to Upper Kimmeridge Clay Formation/BCU
688 interval; Figs. 2 and 3), which is split into two depocentres, trending along the axis of the Penguin half-
689 graben: (i) a southern depocentre within the hanging-wall of the Brent Fault, and (ii) a north-eastern
690 depocentre (Fig. 16b). The Brent Fault tips out within the MSM, and was active during the deposition
691 of the upper reservoir based on thickening into its hanging-wall (Fig. 16a, Y-Y^{1}). The reflection are
692 high-amplitude but contain both high and low acoustic impedance responses that are more
693 discontinuous than the lower reservoir (Fig. 16a, X-X'). Amplitude extractions from near top MSM,
694 show high amplitudes are truncated by the BCU (Fig. 16b, -20 m). Amplitudes trend SW, increasing
695 from isolated linear forms to more connected responses, suggesting a possible change in the sediment
696 supply direction when compared to MSA (Fig. 16b, -50 m). The upper reservoir is more heterogeneous
697 than the lower reservoir, preventing calibration of individual facies to the seismic response. However,
698 backstepping of the system to the NE is inferred from an absence of high amplitudes in the south near
699 the top of the reservoir (Fig. 16b, -50 m to -20 m). The upper MSM is overlain by a continuous high-
700 amplitude response in the south-east of the field (Fig. 16b), which is interpreted as the Upper
701 Kimmeridge Clay Formation (Fig. 9f).

702 The upper reservoir also contains several footwall-collapse structures, which can be interpreted as an
703 MTC (i.e. seismic-scale MTDs), with hummocky upper surfaces and high amplitude basal shear zones
704 (Fig. 17) (e.g. Bull et al. 2009; Steventon et al. 2019). The intact rotated blocks and discrete faulting
705 suggests the MTC was emplaced by slump processes (e.g. Mulder & Cochonat 1996). In some slumped
706 areas, updip extensional faults, which offset the BCU and detach into the MSB mudstone-rich unit,
707 create a complex reservoir architecture in areas affected by footwall degradation (Fig. 3d) (e.g.
708 Underhill et al. 1997; McLeod & Underhill 1999).

709

710

711 **MSM Depositional Environment**

712 In this section we synthesise observations from core, petrophysical, petrographic, and seismic reflection
713 data to interpret the overall stratigraphic evolution of the Magnus Sandstone Member in the Magnus
714 Field, drawing on other field and subsurface studies where relevant.

715 In the lower reservoir, the combination of an updip channel form, and downdip lobate geometries, with
716 the dominance of high-density turbidites (Facies 1) supports a depositional model with (1) sediment
717 supply from the NW, (2) a central updip slope portion characterised by a confined submarine channel,
718 and (3) a downdip toe-of-slope area represented by a turbidite lobe complex (Prélat et al. 2009) (Fig.
719 15). The updip channel is dominated by coarse-grained lag deposits (well M12, Facies 1, Fig. 5),
720 representative of proximal areas near sediment input points and channels where bypass of turbidity

currents is common (e.g. Stevenson et al. 2015). The downdip central area is also dominated by high density turbidite facies and is interpreted to represent the axis of a lobe complex. The mudclast-rich zones may represent boundaries between lobes (Fig. 5). Away from the central axial area, thin-bedded sandstones and background/turbidite mudstones are interpreted as off-axis to lobe fringe environments (Mutti 1977; Walker 1985; Kendrick 1998; Passey et al. 2006).

The MSB unit forms a barrier between the two reservoirs and is composed of predominantly mud-rich debrite, coeval with the *Autissiodorensis* maximum flooding surface (Fig. 7, 9). Unit MSB thickens SE, following the thickness trend of the lower reservoir, and becomes more mud-rich in this direction, we interpret the source area to be from the NW (Fig. 7a). This is consistent with the palaeo-dip of the slope to the SE (Fig. 3c, d). The Magnus dataset only covers part of the MSB, which extends across the Penguin half-graben (Morris et al. 1999). From the Magnus to Penguin-A Field, the MSB unit shows a thickening trend up to 33 m, terminating against the Penguin Horst (Al-Abry 2002). Al-Abry (2002) also notes the presence of debritic and slumped facies confined to the collapsed terrace areas of the Penguin Horst, relating their presence to slope instability, while noting other areas are dominated by background mudstones (Fig. 18b). This suggest that the debrite-rich MSB (i.e. Facies D1-4) in the Magnus area forms one of at least two debrites, initiated and transported towards the basin centre during a period of instability. We infer that the two debrite units are isolated to the slope and terrace areas of the Magnus and Penguin-A Fields respectively (Fig. 18b). Facies D5 in the northern area of the Magnus Field is interpreted to form as a separate deposit (Fig. 18b). Overall, we interpret the MSB to represent basin margin instability, likely triggered from normal faulting and oversteepening, after a period of sand starvation possibly related to relative sea-level rise (e.g. Piper et al. 1997; Strachan 2002; Grecula et al. 2008).

The upper reservoir comprises at least two lobe complexes, separated by the mud-dominated MSD and MSF units (Figs. 9a and 16). The NE-trending linear amplitudes are interpreted as distributary channels, suggesting sediment supply from the NE (Fig 16b). However, an alternative interpretation may be that the linear amplitudes represent linked fault-bound depocentres that have focused sediment axially along the field. As the Brent Fault was an active palaeo-high during deposition, it is likely the southern depocentre input point was near the original lower reservoir channel, whereas the northern depocenetre was located NE of the Magnus Field (Fig. 16b). Facies within the upper reservoir are dominated by high-density turbidites, with thin-bedded sandstones, banded, hybrid and remobilised deposits common in both the MSD and MSF units. In other studies, banded beds have been observed at the transition between lobe axis and off-axis settings (e.g. Spychala et al. 2017b), or in proximal lobe settings (e.g. Stevenson et al. 2020). In the upper reservoir banded sandstone beds are concentrated above the mud-rich MSB unit (see Fig. 6f-i) suggesting that banded sandstone beds in MSC represent initially turbulent sediment-gravity flows interacting with the mud-rich slope substrate of MSB (e.g. Davis et al. 2009; Stevenson et al. 2020). Hybrid and remobilised beds are typically diagnostic of frontal lobe fringe

environments (e.g. Barker et al. 2008; Spychala et al. 2017b), and may also mark fan initiation cycles (e.g. Hodgson 2009). In the Magnus Field, transitional flow deposits and low-density turbidites dominate in the lower MSC, MSD and MSF of central and southern wells (e.g. Fig. 6h, well M16), with fewer of thee facies types in the northern area of the field (e.g. see Facies proportions, Fig. 9). This supports the overall upper reservoir system being sourced from the NE, with well 7-1 in a proximal and axial lobe location, supported by the dominance of high-density turbidites and limited number of transitional flow deposits (Fig. 6j-l, Fig. 9). This is supported by the distribution of high-amplitudes in the upper reservoir, which backstep to the NE (Fig. 16b). In the central and southern areas, we interpret the system to be in a predominantly axial lobe location, evidenced by the dominance of high-density turbidites. However, distinct mud-prone units (MSD and MSF) represent periods of lateral shift and/or system backstepping to the north, moving the central and southern areas into off-axis or distal positions, and therefore, promoting the deposition lobe fringe deposits. This interpretation is consistent with the Magnus Field being located on the basin margin of the Penguin half-graben. Similar observations were made farther north in the basin where high-density turbidite axial lobe deposition was correlated with lobe fringes dominated by transitional flow deposits (Haughton et al. 2003).

DISCUSSION

Evolution of the submarine slope depositional system in the Magnus reservoir and wider Penguin half-graben

The MSM records a significant sediment pulse during relatively high subsidence rates in the Penguin half-graben (Al-Abry 2002), and is coeval with the uplift of the Nordfjord High (see Fig. 2 inset map) to the north west and Shetland Platform to the west (Ziegler 1990; Ravnås & Steel 1997). The MSM onlaps the Penguin Horst, indicating it was a paleo-high during deposition (Dominguez 2007). However, it is likely the Magnus and End of the World faults experienced only minor activity, or were in fact dormant during much of MSM deposition (Ravnås & Steel 1997) (Fig. 2, inset maps). Sedimentation during the MSM can be separated into four stages: (i) confined sediment input derived from the north-west, (ii) a period of relative sea-level rise and basin instability, (iii) a switching of sediment input to a northern province, and (iv) a further period of instability.

Stage 1: The lower reservoir (MSA) is characterised as a centrally restricted, fault-controlled channel-lobe complex, sourced from a single north-westerly input point (Fig. Fig. 15b & 9a). Probable hinterland source areas include the Magnus Basin (North Shetland Trough), which had not fully subsided at this time, and the Nordfjord High/Margareta Spur. Ravnås & Steel (1997) propose a fill-and-spill model for the MSM deposition, interpreting that the Magnus Basin had limited accommodation, promoting

sediment transport farther basinwards into the Penguin half-graben (Fig. 18a). An alternative interpretation is a sediment source from the Shetland Platform to the west, similar to other Upper Jurassic deep-water systems in the Moray Firth and Viking Graben (Shepherd et al. 1990).

Stage 2: MTDs are typically associated with shelf-edge and/or slope instability (e.g. Nemec et al. 1988; Nemec 1990; Mayall et al. 1992; Galloway 1998). The mud-rich character of the MSB debrite support its association with a period of reduced clastic input and precedes reorganisation of sediment supply from the north-west (lower reservoir) to the north (upper reservoir) (Fig. 18). Increased subsidence is likely during this time, due to fault population linkage correlating with the formation of the maximum flooding surface (*Autissiodorensis)*, and an increase in hemipelagic radiolarian diversity (Morris et al. 1999; Al-Abry 2002) (Fig. 9). Therefore, the preconditions to slope failure may have been relative sea-level rise and hemipelagic sedimentation, and slope steepening due to tectonism, with failure across a weak mud-rich layer (e.g. Bull et al. 2009; Spychala et al. 2017a). Similar debrite facies with starry-night textures have also been observed to compartmentalise other turbidite reservoirs in the North Sea (e.g. Britannia Field, Barker et al. 2008; Eggenhuisen et al. 2010), and in outcrop-based studies (e.g. Pickering & Corregidor 2005; Jackson & Johnson 2009; Auchter et al. 2016).

Stage 3: The input direction for the upper reservoir (MSC-H) is interpreted to change to the north-east, evidenced by the SW-trending seismic amplitudes and axial trending depocentres (Fig. 16b). This suggests a shift in sediment supply from north-west to north, with potential sources including the Makrell Horst/northern Penguin Ridge and the Magnet Ridge (Ravnås & Steel 1997; Gabrielsen et al. 1999; Al-Abry 2002). However, heavy mineral percentages from QEMSCAN show no change between upper and lower reservoirs, which may suggest: (i) a change in sediment routeing pattern but not source area; (ii) a change in catchment area with eroded sediments being mineralogically consistent between the two areas; (iii) intrabasinal sediment storage and recycling; and/or (iv) updip mixing of multiple source terrains.

Stage 4: During the latest Jurassic to earliest Cretaceous, the basin transitioned from sand-rich MSM deposition into the mud-dominated Upper Kimmeridge Clay Formation. This transition is associated with the *Hudlestoni* maximum flooding surface (base J66), which can be correlated across the basin (Morris et al. 1999). This relative sea-level rise may be associated to the linkage of the Magnus and End of the World basin-bounding faults, related to the opening of the Magnus Basin (North Shetland Trough) and the Møre Basin, to the west of the study area (Fig. 17c). The observed slumping in the upper MSM was likely caused by increased activity on basin-bounding faults and associated uplift and tilting of their footwalls (Fig. 17).

Identifying sealing sub-seismic MTDs

Understanding of the sealing potential of MTDs is important for several applications including: (i) the distribution of reservoir-seal pairs, and stratigraphic traps during exploration, particularly on unstable basin slopes (e.g. Sabah, NW Borneo, Grecula et al. 2008), (ii) understanding reservoir compartmentalisation during hydrocarbon production, and (iii) subsurface pore pressure prediction and the correct placement of well engineering (e.g. casing shoes) during drilling operations. Numerous studies have shown the sealing capacity of seismic-scale MTDs (e.g. Flemings et al. 2008; Algar et al. 2011; Dugan 2012; Day-Stirrat et al. 2013; Cardona et al. 2016; Sun et al. 2017; Wu et al. 2019). These studies highlight the importance of densification and shearing, causing enhanced alignment of clay minerals along basal shear zones, leading to a reduction in porosity and permeability. Through the analysis of core, petrophysical, and particularly pressure data, we have demonstrated the ability of a sub-seismic MTD (MSB) to act as a competent field-wide barrier to fluid flow.

Initial identification of abrupt pressure barriers between reservoirs or internally within a reservoir zone, is a useful method for identifying potential sealing-MTDs (Fig. 10a). Petrophysical logs should allow a distinction between mud-rich sub-seismic MTDs and slope mudstones. However, with increasing burial and compaction, along with hydrocarbon charge, log responses identified from studies of shallower sections (e.g. < 1 km) can become unreliable in predicting deeply buried sealing-MTD (e.g. Sawyer et al. 2009; Day-Stirrat et al. 2013). It should also be noted that wireline logging tools have a vertical resolution of ~0.15 m, and therefore, will only characterise trends throughout an MTD and not more subtle, core-scale heterogeneities (Table 2). Gamma-ray values are generally high (> 75 gAPI), related to high volumes of clay in the MTD matrix, but can be variable depending on the lithology of entrained clasts and large blocks. Density motifs in shallow studies are characterised by high values when compared to surrounding sediments, and peaks in the basal zone are attributed to shearing and over consolidation (Dugan 2012; Wu et al. 2019). In the Magnus Field, the MSB unit demonstrates higher densities than bounding sedimentary successions, similar to shallow studies (< 1 km). However, caution should be taken when using this approach below the sand/shale density crossover (~600 mbsf, Cook & Sawyer 2015), and in deeper formations, as sandstone can become much denser than shale, particularly during the onset of cementation (e.g. Avseth 2000). Neutron-density plots should display a cross-over with neutron to the left and density the right, indicating a shale response (Fig. 8a). In shallow studies, resistivity in MTDs is generally higher than background sediments and is particularly elevated in the basal zone (e.g. Day-Stirrat et al. 2013). This increase is attributed to densification and porosity loss when compared to background mudstones (Flemings et al. 2008; Dugan 2012). In this study, we observed a similar downward increase in resistivity within the MSB unit, with a peak in the basal zone (Fig. 8a). However, below the MSB resistivity increases further in the oil-filled MSA reservoir, and therefore, resistivity should not be a discriminating factor when identifying MTD-based hydrocarbon seals or barriers (Fig. 8a). MTD porosity should be low (<10%) (Fig. 4, PHIT), with possible isolated

high-porosity zones generated by entrained clasts (e.g. sample QM6, Fig. 14a). Volumes of clay are likely to be high (e.g. 37-57% in MSB, Fig. 14a).

Recognition of sub-seismic sealing MTDs should be undertaken through the integration of multiple datasets, particularly pressure measurements which provide a valuable dynamic validation of hydraulic sealing. For example in the Måløy Slope, offshore Norway, sub-seismic debrites and slumped units can be identified by integration of well-logs through electro-facies analysis (Prélat et al. 2015). The Buzzard Field, in the Central North Sea, shows how intra-reservoir mud-prone slump units were initially predicted to be sealing, however, during production bounding reservoir units were found to be in pressure communication (Ray et al. 2010). Hence, individual motifs from a single log or core sample alone cannot reliably indicate a sealing-MTD. Multiple log motifs and formation pressures should be observed in unison. In addition, MTDs are likely to show higher spatial and stratigraphic variability, when compared to background sediments.

Lateral variability of the MSB and impact on later deposition

Sources of mud for the MSB unit and younger transitional flows

Mud-rich substrates and/or source areas are important for the development of laminar and transitional flows, in both the initiation stages of shear failure as in the case of MTDs, or during flow transformation(s) of hybrid, banded, and remobilised beds (e.g. Haughton et al. 2003; Davis et al. 2009). Flume tank experiments have shown the development of cohesive debris flows needs >10-15% of cohesive fines (<20-30 μm) (Talling 2013). The fines content of transitional flow deposits varies spatially, and can be explained through several mechanisms including: (i) deposition of coarser fractions during the initial flow, (ii) variation in substrate and entrainment of mud-rich fractions causing longitudinal flow transformation, (iii) failure of a heterogeneous source, and (iv) partial transformation of debris flows (Haughton et al. 2003; Barker et al. 2008). However, for both laminar and transitional flows, sources of cohesive muds are essential. The MSB and MSF units validate the importance of coring clay-rich units, and not initially assuming they represent background mudstone sedimentation. MSB also demonstrates that correlation of maximum flooding surfaces (e.g. *Autissiodorensis* of MSB) and hemipelagic radiolaria diversity do not necessarily equate to *in situ* hemipelagic mudstones. Morris et al. (1999) suggest the interpretation of microfossils within the MSB is not decisively hemipelagic, but rather a mix of hemipelagic and low-density mud-rich turbidites. This suggests that mudstones could have been sourced partially from hemipelagic sedimentation, and partially from mud-rich turbidites, during a period of relative sea-level rise (Fig. 15b, 18a). Volumes of mudstone deposited by muddy turbulent flows can be significant (10s m), even near sediment entry points (see Boulesteix et al. 2019). In the case of the MSB unit, it is probable that hemipelagic sediments and muddy turbidites were remobilised and entrained into the interpreted cohesive debris flow (MSB). This suggests the Penguin

half-graben experienced variability in the thickness and source of mudstone sedimentation, both during and after the deposition of the sand-grade MSA. Thus, the extent of the MSA may influence the lateral and downslope variability of the MSB, described below.

MTD lateral variability and sealing

Sedimentation rates and a source of sediment for mass-transport is an important consideration, with many tectonically active margins experiencing low sedimentation rates recording limited mass-transport processes (e.g. Tappin et al. 2007). Laterally the MSB can be split into: (i) central and southern areas characterised by mud- and clast-rich debrites (Facies D1-4, Table 2), and (ii) a northern area characterised by injectites and slumping fabrics (Facies DB, Table 2, Fig. 17b). This observed variability correlates with the presence and composition of the underlying MSA reservoir (Fig. 7a). In the central and southern areas, deposition of sand- and mud-grade material from the MSA channel-lobe complex, would have enabled the debris flow to preferentially entrain sandy-substrate. This, combined with a subsequent relative sea-level rise (Partington et al. 1993) and fault activity (Al-Abry 2002), would provide preconditioning factors for shear failure and the development of a cohesive debris flow. Preferential entrainment of the axial part of channel-lobe systems during mass-transport has also been observed in other systems (e.g. Magdalena fan, offshore Columbia, Ortiz-Karpf et al. 2017).

The northern area experienced lower sedimentation rates during the MSA period, and was topographically elevated compared to the central and southern areas, hence the absence of cohesive debris flow deposits. As the northern MSA interval was not charged with oil, the MSB has not been dynamically tested as a barrier (e.g. well 7-1, 7a-3, Fig 7a). However, inclusion of sand injectite fabrics in the northern MSB may indicate the presence of larger injectites that can act as efficient fluid flow conduits between disconnected reservoir units, casting uncertainty on seal integrity in the area (e.g. Hurst & Cartwright 2007; Cobain et al. 2017; Dodd et al. 2019).

Understanding the lateral variability of clay-rich zones should be considered an important component of hydrocarbon seal evaluation. The MSB highlights the importance of this by demonstrating that in slope settings, laterally continuous clay-rich zones that are associated with maximum flooding surfaces do not always correlate with hemipelagic/pelagic sedimentation. The MSB demonstrates the potential for clay-rich sub-seismic MTDs to act as competent seals or barriers, but that lateral heterogeneities within such rock bodies can pose a risk to seal integrity. It should be noted that there is likely uncertainty in MSB short-scale variability (i.e. <10's m), which has been identified in field examples of other debrite rich intervals (e.g. Fonnesu et al. 2015; Auchter et al. 2016).

Flow-deposit interactions above the MSB

Above the MSB unit, particularly in the central region of the Magnus Field, the stacking of transitional flow deposits and hybrid beds follows a common pattern (Fig. 6). The lower part of MSC is characterised by a transition between mud-rich debrites, and remobilised flows and/or banded beds, both of which are common in cores (e.g. Fig. 6, M1, M12, M16). This is consistent with flows entraining a mud-rich substrate after the emplacement of the MSB debrite, and the rerouting of the sediment transport system to a NE input leading to flow transformation. However, hybrid beds are most common after the initial transition, and are distributed throughout the upper reservoir interval. This is common when slopes are in constant out-of-equilibrium states, as was probably the case in the Penguin half-graben (Haughton et al. 2009).

Therefore, we suggest an idealised stacking pattern after the deposition of a mud-rich MTD, whereby flows are prone to transformation, leading to the preferential deposition of transitional flow deposits (Fig 19f). This idealised stacking pattern implies that the paleo-seabed was mud-rich and the emplacement of the MSB debrite likely modified pre-existing sediment dispersal patters, forcing flows through poorly established routing systems. These two factors may explain how turbulent flows were preferentially susceptible to becoming charged with mud and transformed into transitional flow types in the lower part of the MSC. The preferential development of transitional flow deposits directly above mud-rich MTDs is important for the reservoir potential of the lower MSC, which has been negatively impacted (see Fig. 14a, 19f). The recognition of this idealised stacking pattern may also be important for predicting the reservoir potential of other deep-water turbidite reservoirs.

Reservoir architecture and transitional flow deposit heterogeneity

The core porosity and permeability data, and QEMSCAN results support identification of principal reservoir facies (Facies 1, 2, and 4), and barriers/baffles (Facies 3, 4, 5 & 6) within the Magnus Field. Figure 14a demonstrates the influence of sediment gravity flow type on reservoir quality and shows a similar overall trend to other studies comparing sediment gravity flow mechanism and reservoir quality (Porten et al. 2016; Southern et al. 2017). Below we consider the reservoir architecture within the Magnus Field, and bed-scale heterogeneities of barriers and baffles, including their potential effects on Kv/Kh, reservoir modelling, and production from sand-rich submarine fans.

Reservoir architecture

Figure 19 summarises the reservoir architectures observed within the Magnus Field. The central area captures the full extent of the reservoir with a thick lower lobe complex (MSA), widespread debrite

963 deposition (MSB) and a full upper reservoir sequence (MSC-H) (Fig. 19a). In the southern area the
964 lower reservoir is thin or absent and the upper reservoir is divided by the Brent Fault High. In the
965 northern area, the lower reservoir is also thin or absent, and the upper reservoir's stratigraphic
966 architecture is complicated by gravitational faulting and a distinctive MSB that we interpret to be
967 confined to a small area of the slope (Fig. 18, 19). The central area of the lower reservoir is estimated
968 to be composed of ~80-90% high-density turbidites, and therefore is highly homogeneous with no
969 significant baffles impacting production (Kv/Kh ≈ 0.8) (Fig. 19e). The pressure data also shows that the
970 MSB within the central and southern areas acts as a competent fluid flow barrier, compartmentalising
971 the upper and lower reservoir (Fig 19e). Sealing faults are known to have split the field into numerous
972 sectors with deep-seated (i.e. rift-related) extensional and thin-skinned slump faults (Fig. 17) impacting
973 reservoir production (Shepherd et al. 1990).

974 In addition to these major features which were identified early in field development and production
975 (e.g. De'Ath et al. 1981; Shepherd 1991; Morris et al. 1999) we also identify the role transitional flow
976 deposits play in controlling vertical permeability and differential pressure depletion within the upper
977 reservoir (Fig. 10). Shepherd et al. (1990) showed the significance of mudstones within the upper
978 reservoir, which were observed to act a laterally extensive baffles to fluid flow, compartmentalising the
979 field into four sand-rich reservoir units. Here, we can demonstrate that transitional flow deposits are
980 also acting as intermittent pressure discontinuities, namely in the MSD and MSF, but also within
981 subzones of the Magnus Field (Fig. 10a). The Magnus Field demonstrates how transitional flow deposits
982 can impact vertical permeability, showing that they can isolate reservoir sandstones and negatively
983 impact the sweep efficiency (i.e. the volume of reservoir "swept" by injected fluids, Lake 1989) during
984 waterflooding and enhanced oil recovery (Fig. 10a).

985

986 *Bed-scale heterogeneities and outcrop analogues*

987 Capturing bed-scale heterogeneities and the geometry of baffles and barriers is important for
988 understanding reservoir properties, distribution, and sweep efficiency. Begg & King (1985) demonstrate
989 the importance of characterising baffle dimensions, showing exponential relationships between
990 increasing baffle dimension (i.e. thickness, width, length) and decreasing effective K_v (Fig. 19d). The
991 3D nature of baffles and barriers is particularly important, as 2D reservoir simulations of impermeable
992 heterogeneities often significantly overestimate their effect on reservoir production (see Jackson &
993 Muggeridge 2000). A limitation of reservoir modelling is that many impermeable heterogeneities
994 captured in core may be lost through the upscaling process during reservoir simulation, whereby a
995 reservoir model (~50-100 m grid scale) aims to realistically capture 3D bed-scale heterogeneities (Fig
996 19d). However, high resolution reservoir modelling and new technologies such as surface-based grids
997 (e.g. Jackson et al. 2014; Jacquemyn et al. 2019) and adaptive reservoir model grids (e.g. Melnikova et

al. 2016) are beginning to allow reservoir models to realistically capture heterogeneities identified during wireline and core logging. To achieve this, outcrop analogues can be used to help improve our understanding of baffle dimensions.

In the Magnus reservoir we have identified several facies that act as baffles to fluid flow (Facies 2, 3, 4, 5) or, if amalgamated, as barriers (i.e. MSF) (Fig. 19e, Table. 2). However, we are not able to correlate individual beds across the field. Outcrop examples of transitional flow deposits allow us to take subsurface observations and compare these with possible analogues, where correlation along well exposed outcrop allows confirmation of dimensions. The Ross Sandstone Formation, in county Clare, Ireland, may provide a suitable outcrop analogue. The formation is composed of a sand-rich deep-water channel-lobe system, with a relatively high-proportion of hybrid-event beds and MTDs (e.g. Pierce et al. 2018). Studies focusing on lobe fringe environments in the Ross Sandstone Formation, where low-density turbidites and hybrid beds dominate, show hybrid-event beds and MTDs can be correlated for ~1 km (Pierce et al. 2018). Pyles & Jennette (2009) identify these fringe areas to have lower net to gross and a higher proportion of MTDs. Other outcrop studies of transitional flow deposits include: the Gottero Turbidite Sandstone in north-west Italy. Here, hybrid beds can be correlated for ~4 km, with both laterally continuous and discontinuous morphologies (see Fonnesu et al. 2018). In the Skoorsteenberg Formation, Karoo Basin, South Africa, hybrid beds are preferentially concentrated in lobe fringe environments, where individual beds can be tracked for ~0.5-1 km, becoming amalgamated updip and along-strike (Hodgson 2009; Spychala et al., 2017).

These outcrop examples demonstrate how transitional flow deposits may form 100's m scale baffles to fluid flow. Studies of other Upper Jurassic North Sea turbidites reservoirs (e.g. Brae-Miller-Kingfisher fan) have interpreted the debritic intervals of transitional flows to be widespread across the system, evidenced by large exotic (i.e. non slope derived) clasts (Haughton et al. 2009). Therefore, assuming the model of increasing thickness of H3 (i.e. debritic divisions) towards the lobe fringe (see Haughton et al. 2003), it is likely that hybrid beds in the upper reservoir of the Magnus Field are laterally continuous from mid-lobe to lobe fringe environments. This model is consistent with our observations of pressures, where transitional flow deposits reduce the vertical permeability, connectivity of turbidite facies, and sweep efficiency during production (Fig. 10, 19e). Amy et al. (2009) undertook a 2D reservoir flow simulation of the Marnoso Arenacea Formation in northern Italy, composed of sheet-like basinfloor turbidite sandstone with related transitional flow deposits. They similarly found beds containing significant debritic material (porosity <15%, permeability <100 mD) which reduced production efficiency and led to quicker water breakthrough. Our results highlight the importance of characterising not just background mudstone but also other non-reservoir rocks. This is particularly true for transitional flow deposits which are in most cases genetically related to the distribution of turbidite reservoirs (e.g. Davis et al. 2009; Hodgson 2009; Spychala et al. 2017b). These deposits should be

1033 properly characterised during reservoir modelling studies of turbidite channel-lobe systems, in order to
1034 adequately capture the heterogeneities in rock properties and simulate fluid flow within a reservoir.

1035

1036

1037 # CONCLUSIONS

1038

1039 (i) The evolution of the Magnus Sandstone Member's depositional system in the Penguin half-
1040 graben can be divided into 4 main phases: *Phase 1* deposition of a centrally fault controlled
1041 channel-lobe complex dominated by high-density turbidite facies, with a likely provenance
1042 from the north-west, *Phase 2* a period of flooding, slope instability, and deposition of a mud-
1043 rich debrite by a cohesive debris flow, *Phase 3* a shift of sediment supply from the north-west
1044 to the north/north-east, and deposition of lobe complexes along the axial trend of the half-
1045 graben, and *Phase 4* a relative sea level rise, basin tilting, and slumping within the Magnus
1046 footwall. Post-rift thermal subsidence continued during the Cretaceous and Tertiary sequences.
1047
1048 (ii) Sub-seismic MTDs can act as competent fluid flow barriers at depth. Identification of such
1049 deposits is best undertaken through the integration of fluid pressure, petrophysical, and core
1050 data. Distinguishing features include abrupt pressure barriers between permeable flow units,
1051 diagnostic motifs of logs (bulk density and resistivity) through comparison of MTDs with
1052 background mudstones, variability in response across the deposit, high (>35%) volumes of clay,
1053 and sedimentary structures associated with shear failure and mass-transport processes (e.g.
1054 debritic textures, soft-sediment deformation, and sheared fabrics).
1055
1056 (iii) Evaluation of lateral variability within an MTD is critical in establishing its ability to act as a
1057 competent barrier unit. The MSB unit demonstrates a stark contrast between mud-rich debritic
1058 textures in the central and southern areas which are known to be sealing, and the northern area
1059 where injection fabrics may provide fluid conduits between disconnected reservoir units. This
1060 variability is also significant for reservoir development strategies and the prediction of fluid
1061 pressure cells between reservoir segments.
1062
1063 (iv) Transitional flows may preferentially form above mud-rich substrates such as the MSB, where
1064 turbulent flows are susceptible to becoming charged with cohesive mud. This produces an
1065 idealised stacking pattern with transitional flow deposits (e.g. banded and remobilised beds)
1066 occurring directly above mud-prone MTDs or other mud-rich substrates.
1067

(v) Transitional flow deposits have been shown to act as intermittent barriers or baffles to fluid flow. In the upper reservoir the deposits have compartmentalised the turbidite sandstone into sub-zones, significantly reducing sweep efficiency and enhancing early water breakthrough. Capturing these bed-scale heterogeneities during reservoir modelling is crucial for realistic reservoir flow simulation and an effective field development strategy.

Acknowledgements

We would like to thank Equinor, EnQuest, and Rocktype for their funding, access to data and general support throughout the project. The corresponding author would also like to thank the Geological Society of London for research funding through the Daniel Pidgeon Fund. We would also like to thank the Editors Caroline Hern and Kim Klitgord, and reviewers Neal Auchter, Martin Grecula, Mark Bentley, and one anonymous reviewer for their constructive feedback which greatly improved the final manuscript.

Data Access Statement

Some of the datasets generated during the current study are available through the OSF open-access repository, https://osf.io/2kfre/. However, some of datasets analysed the current study are not publicly available due to commercial confidentiality.

Figure captions

Fig.1 – Conceptual models of MTDs effect on reservoir and seal distribution, (a) dip section of shelf-slope-basinfloor transect with potential trapping mechanisms for turbidite slope channels, sheets, aprons, and basinfloor lobes from the Eocene shelf-edge-slope-basinfloor transect, offshore Brazil (modified from Steventon et al. 2020), (b) strike section of MTD affecting lobe reservoir distribution, observed from Temburong Formation, NW Borneo and Tres Paso Formation, Southern Chile (modified from Jackson & Johnson 2009, Armitage & Jackson 2010) (c) idealised formation pressure and petrophysical responses of a sealing-MTD.

Fig.2 – (Left) Reservoir distribution map of the Magnus Field, note inset maps with field location in relation to the wider structural framework, (Right) northern North Sea stratigraphic column of the Jurassic-Cretaceous, with studied section highlighted in red. Volgian is a regional term approximately equivalent to the Tithonian. Collated from Shepherd et al. (1991), Partington et al. (1993), Morris et al. (1999), Al-Abry (2002), and Dominguez et al. (2007).

Fig.3: Field overview, (a) seismic dip section through the field (note: location X-X' found in Fig.2a), (b) geoseismic section of principle seismic-stratigraphic units, note updip pinch-out and truncation of the MSM into the BCU, highlighting the combination structural-stratigraphic trap, (c) Top Heather depth structure map with major normal fault arrays, (d) BCU depth structure with late-syn rift normal faults and MTD headwall scarps and slump faults (see Fig. 17a), (e) summary of reservoir units MSA to MSH from well 211/12a-M16.

Fig.4: (a) Summary core logging sheet from 211/12a-M16 with main lithologies, reservoir units, and petrophysical responses. Note positions of samples (QM) taken for QEMSCAN analysis. RHOB = bulk density, NPHI = neutron porosity, PHIT = total porosity. (b) Detailed log of the MSB unit from well 211/12a-M16, note depths of core photos in Figure 6 & 7.

Fig.5: Summary of turbidite (F1-2), transitional (F3-4), and debrite (D2-4) core facies observations.

Fig.6: (a-d) core photos of the downslope longitudinal flow transformation of Facies D1-4 from sand-rich to clay-rich, (e) core photo of facies D5 (see Table 2), (f-l) observations of the transition between MSB and MSC. Note green arrows marking the contact, well 7-1 contact was not recovered during coring.

Fig.7: (a) MSB thickness calculated from formation tops from wells, note the correlation between thickness and the outline of the underlying MSA unit. (c-p) core photos capturing the heterogeneity within the MSB units. Note the basal shear zone (BSZ) or contact between the MSA and MSB is marked by a green arrow, (r-q) example of axial and off-axis MSA.

Fig.8: (a) Petrophysical log suite from 211/12a-M16 summarising the Magnus Reservoir, from left to right, GR = gamma-ray, CALI = calliper, NPHI = neutron porosity, RHOB = bulk density, DRHO = density correction, DTCO = compressional (sonic) velocity, RMEDI = medium resistivity, RDEEP = deep resistivity. (b) horizontal core permeability vs. core porosity, and (c) vertical core permeability vs. core porosity.

Fig.9: Reservoir correlation panels, (a-c) downdip correlations, (d-f) along-strike correlations. Note facies proportions in logged wells, and biostratigraphic markers Autissiodorensis, Iathetica re-influx, and Hudlestoni.

Fig.10: (a) formation fluid pressure plots, note pressure break associated with MSB, MSD, MSF and isolated transitional flow deposits, (b) change in pressure observed between MSA and MSC, (c) plot of change in pressure between MSA and MSC vs. MSB thickness, (D) production profile of the Magnus Field, including both oil production and water production (cut), note activity timelines of wells.

Fig. 11. Mineral maps and related porosity extractions of turbidite facies (HDT = high-density turbidites, VCL = volume of clay). Field of view = 2×2 cm.

Fig. 12. Mineral maps and related porosity extractions of laminar and transitional flow deposits (VCL = volume of clay). Field of view = 2×2 cm.

Fig.13: Grain-size distribution of quartz phases extracted from the QEMSCAN samples QM1-14 (see Fig. 4a for sample depths within well M16).

Fig.14: (a) QEMSCAN total volume of clay vs. porosity, note linear relationship, with turbulent facies having low clay and high porosity values and debrites having high clay and low porosity values, (b) quartz-feldspar-lithics ternary plot of QEMSCAN samples generally clustering around sub-arkose, arkose, lithic arkose, and feldspathic litharenite categories.

Fig.15: (a) strike-orientated seismic sections imaging the evolution of the lower reservoir (MSA) from a confined updip channel to distributive lobe complexes downdip, note sections are displayed using a coloured inversion cube, with high (hard) acoustic impedances = blue, and low (soft) acoustic impedance = yellow, (b) thickness map highlighting the central isopach thick of the lower reservoir, with sum of negative amplitude extractions highlighting the geometry and evolution of the MSA reservoir channel-lobe system.

Fig.16: (a) dip-orientated seismic sections highlighting the evolution of the upper reservoir (MSC-H), with the central section (X-X1) imaging the depocentre to the north of the Brent Fault High, and the southern section (Y-Y1) imaging the syn-depositional depocentre south of the high, note sections are displayed using a coloured inversion cube, with high (hard) acoustic impedances = blue, and low (soft) acoustic impedance = yellow, (b) thickness map highlighting the southern and northern isopach thicks, with RMS amplitude extractions highlighting the geometry and evolution of the upper reservoir and the Upper Kimmeridge Clay Formation (UKCF).

Fig.17: (a) northern dip-orientated seismic section of slumping within the upper reservoir, with extensional slump faults detaching into the MSB, (b) southern dip-orientated seismic section with minor incision and slumping. Note slump faults displace the BCU.

Fig. 18: Basin evolution of the Penguin half-graben, (a) Lower reservoir point sourced from the north-west, (b) Intra-reservoir MTD composed of debris flow from both the Magnus and Penguin Horsts, (c) Upper reservoir inferred to be sourced from the north-east, with a local input point transporting sediment into the hanging-wall of the Brent Fault.

Fig. 19: Synthesis of lateral variability in reservoir architecture (a-c) idealised cross-sections of the northern, central, and southern reservoir architectures, (d/e) highlighting the difficulty of capturing core-scale heterogeneity in geological and simulation grid scale reservoir models, with a grid cell only able to represent a single value for porosity and permeability, with effective vertical permeability vs. baffle dimension showing the importance of understanding baffle dimension (modified from Begg & King 1985), (f) summary of reservoir heterogeneity within the Magnus Field.

Table 1: Summary of reservoir sedimentology in the Magnus Sandstone Member (MSM). Note Kv/Kh ratios are calculated from core plug data.

Facies	Lithology	Thickness (m)	Sedimentology	Interpretation	Reservoir Unit (approx. Φ, Kv, Kh, VSH, Facies proportions %)
Thick-bedded sandstones (F1)	Fine-coarse grained sandstone, infrequent fine sandstone/siltstone caps	0.2->1.0 (amalgamated)	Massive or planar laminated sandstone, subtle normal grading, dewatering pipes/dishes, flame and load structures, with common bed amalgamation. Floating mudclast-rich horizons with sheared fabrics distributed throughout. Rarely preserved fine sand-silt grade ripple laminated bed tops.	*Process:* High-density turbidity currents (see Lowe 1982; Shanmugam 1996), *Environment:* forming in an axial submarine lobe position	*Primary reservoir* MSA & MSC-G Core Φ = 22% Log Φ = 29% Kv = 500 mD Kh = 600 mD Kv/Kh = 0.83 Log VSH = <1%
Basal sandstones (F1)	Medium sand to granule grade sandstones	<0.05-0.25	Sandstones, with weak to irregular grading, imbrication of granule/pebble material, and incisional/erosive bed bases	*Process:* tractional carpets at base of turbidity flow, *Environment:* basal lag deposit of submarine channel or bypass surface from the passage of turbidity currents (Walker 1984)	MSA & MSC-G Log Φ = 26% VSH = 3%
Thin-bedded sandstones (F2)	VF-Fine grained sandstone and siltstone, with mudstone caps	<0.05-0.2	Current ripple laminated sandstones, occasional flame and load or shear fabric structures at the base (T_C). Sharp normal grading from sandstone to silt and mudstones ($T_{D/E}$).	*Process:* Low-density turbidity currents (Mutti 1977), *Environment:* forming in an off-axis, submarine lobe and/or channel position (Jobe et al. 2012).	MSC-G Core Φ = 22% Log Φ = 15% Kv = 400 mD Kh = 575 mD Log VSH = 7-14%
Banded beds (F3)	Couplets of VF-Fine grained sandstone and siltstone, with mud-rich sandstones	<0.05-0.35	Distinctive alternating light/dark banding couplets. Light bands are often planar or ripple-cross laminated, sand-silt, upper contacts are either sharp or gradational, foundering structures common at base. Dark bands have elevated amounts of mudstone.	*Process:* Transitional flows, alternating between turbulent and laminar flows (Lowe & Guy 2000), *Environment:* submarine lobe sourced from and/or depositing on mud-rich substrate (Stevenson et al. 2020).	MSC-G Core Φ = 20 Log Φ = <1-24% Kv = 0.27 mD Kh = 21 mD Log VSH = 0-24%
Hybrid beds (F4)	Fine-medium sandstones and mud-rich sandstones	0.15-0.4	Lower sandstone beds graded or ungraded with loading structures at base (H1), dewatering pipes, and isolated mudclasts/chips at bed top.	*Process:* Hybrid event beds/linked debrites, transformation from turbulent	MSC-G (H1 & H3) Core Φ = 20 & 9% Log Φ = 0.23%

			Weakly laminated sandstone or banded bed divisions (H2). Sharp or sharp foundered contact into mud-rich sandstone with debritic texture, sand injections, outsized clasts, with sheared mud-stone clasts at the top of the bed (H3). Sharp irregular contact into parallel/ripple cross laminated fine sandstone and silt (H4). Sharp irregular contact into massive mudstone (H5).	to laminar flows (Haughton et al. 2003; Talling et al. 2004; Haughton et al. 2009), *Environment:* predominantly in distal/fringe submarine lobe positions (Hodgson 2009)	Kv = n/a Kh = 200, 10 mD Log VSH = <1%
Deformed-remobilised "slurry" beds (F5)	Fine grained sandstone, siltstones, and mud-rich sandstone	0.25-0.7	Sheared and folded internal fabrics, ball and pillow structures, relic banded bed (F5) sequences, highly shear mud clasts. Commonly occur in the same sequence as Banded beds (F5).	*Process:* Transitional flows, (Lowe & Guy (2000), with potential for post-depositional remobilisation (Barker et al. 2008), *Environment:* submarine lobe sourced from and/or depositing on mud-rich substrate	
Mudstones (F6)	Mudstone to siltstone	0.02->1.0	Homogeneous mudstones and/or finely (mm-scale) parallel laminated mudstones and siltstones. Contacts are usually sharp.	*Process:* hemipelagic settling and/or mud-rich turbidity currents (Stow & Shanmugam 1980; Boulesteix et al. 2019), *Environment:* slope and basinfloor	MSA-MSG Log Φ = 0% VSH =90+%
Heterogeneous argillaceous beds (MSB) (see Table 6-2) (F7)	Chaotic Mud-rich sandstones, siltstones, and mudstones	1-18 (assuming a single event)	Poorly sorted mud-silt-sand matrix, with varying degrees of clay content from very dark grey/black (>50%), to light (<25%), matrix contains floating fine-medium sand-grade quartz, along with some granule to pebble grade clasts, producing a "starry night texture'. Structures include, sheared fabrics and mudstone clasts, injectites, soft-sediment deformation, micro-faulting, and irregular contacts with undeformed blocks of intact stratigraphy.	*Process:* mass-transport processes initiated from slope instability, predominately "well mixed" cohesive debris flows (Barker et al. 2008; Eggenhuisen et al. 2010), *Environment:* unstable submarine slope	MSB & F QEMSCAN Φ = 7% Log Φ = 6% Kv = n/a Kh = n/a Log VSH = 60%

Table 2: Summary of debrite (Facies 7) sedimentology

Sub-facies	Sedimentological character	Process Interpretation
Sand-rich debrite (D1)	Matrix supported mud-rich sandstones, with coarse sand to granule grade predominantly quartz making up the grains, with minor amounts of mudstone (clasts and sheared fabrics). Bed bases are occasionally grain supported. Sandstone and mudstone clasts are angular and often sheared.	*Process:* poorly cohesive debris flow, with sufficient yield strength to support ~0.5 m clasts, *Environment:* upper to mid slope.
Mud-rich debrites (D2-4)	Matrix supported mud-rich sandstones, with floating quartz clasts, and varying degrees of clay content. Intercalation of clasts and bedded sequences are common with varying degrees of disaggregation from minor soft sediment deformation to clast rich debrites. Often recognisable by "starry night" texture.	*Process:* cohesive debris flow (see Talling et al. 2014, M-2, ~100+ Pa yield strength), with enough strength to support 1+ m clasts, *Environment:* slope and base-of-slope in main MSA lobe complex depositional fairway
Facies (D5) injectite/breccia	Chaotic mix of mudstone-sandstone breccias, sandstones, and mudstones. Structures include soft sediment deformation and injection fabrics.	*Process:* hydraulic fracturing, injection, and minor slumping (e.g. Satur & Hurst 2007), *Environment:* off-axis of initial MSA depositional fairway.

REFERENCES

Al-Abry, N.S. 2002. *Role of syn-sedimentary faulting in controlling deep water depositional systems: Upper Jurassic Magnus Sandstone Member, Northern North Sea.* University of Edinburgh.

Algar, S., Milton, C., Upshall, H. & Crevello, P. 2011. Mass-transport deposits of the deepwater Northwestern Borneo Margin - Characteization from seismic-reflection, borehole, and core data with implications for hydrocarbon exploration and exploitation. *Sedimentary Geology*.

Alves, T.M., Kurtev, K., Moore, G.F. & Strasser, M. 2014. Assessing the internal character, reservoir potential, and seal competence of mass-transport deposits using seismic texture: A geophysical and petrophysical approach. *AAPG Bulletin*, **98**, 793-824.

Amy, L.A., Peachey, S.A., Gardiner, A.A. & Talling, P.J. 2009. Prediction of hydrocarbon recovery from turbidite sandstones with linked-debrite facies: Numerical flow-simulation studies. *Marine and Petroleum Geology*, **26**, 2032-2043.

Armitage, D.A., Romans, B.W., Covault, J.A. & Graham, S.A. 2009. The influence of mass-transport-deposit surface topography on the evolution of turbidite architecture: The Sierra Contreras, Tres Pasos Formation (Cretaceous), southern Chile. *Journal of Sedimentary Research*, **79**, 287-301.

Armitage, D.A. and Jackson, C.A. 2010. Role of Mass-Transport Deposit (MTD) Related Topography on Turbidite Deposition and Reservoir Architecture: A Comparative Study of the Tres Pasos Formation (Cretaceous), Southern Chile and Temburong Formation (Miocene), NW Borneo. Search and Discovery Article, **30121**,11-14.

Atkinson, J. 1985. The use of reservoir engineering in the development of the Magnus oil reservoir. *Offshore Europe*. Society of Petroleum Engineers.

Auchter, N.C., Romans, B.W. & Hubbard, S.M. 2016. Influence of deposit architecture on intrastratal deformation, slope deposits of the Tres Pasos Formation, Chile. *Sedimentary Geology*, **341**, 13-26.

Avseth, P. 2000. *Combining rock physics and sedimentology for seismic reservoir characterization of North Sea turbidite systems*. Stanford University.

Baas, J.H., Best, J.L. & Peakall, J. 2011. Depositional processes, bedform development and hybrid bed formation in rapidly decelerated cohesive (mud–sand) sediment flows. *Sedimentology*, **58**, 1953-1987.

Baas, J.H., Manica, R., Puhl, E. & de Oliveira Borges, A.L. 2016. Thresholds of intrabed flow and other interactions of turbidity currents with soft muddy substrates. *Sedimentology*, **63**, 2002-2036.

Badley, M., Price, J., Dahl, C.R. & Agdestein, T. 1988. The structural evolution of the northern Viking Graben and its bearing upon extensional modes of basin formation. *Journal of the Geological Society*, **145**, 455-472.

Badley, M.E., Egeberg, T. & Nipen, O. 1984. Development of rift basins illustrated by the structural evolution of the Oseberg feature, Block 30/6, offshore Norway. *Journal of the Geological Society*, **141**, 639-649.

Barker, S.P., Haughton, P.D., McCaffrey, W.D., Archer, S.G. & Hakes, B. 2008. Development of rheological heterogeneity in clay-rich high-density turbidity currents: Aptian Britannia Sandstone Member, UK continental shelf. *Journal of Sedimentary Research*, **78**, 45-68.

Beaubouef, R. & Friedmann, S. 2000. High resolution seismic/sequence stratigraphic framework for the evolution of Pleistocene intra slope basins, western Gulf of Mexico: depositional models and reservoir analogs. *Deep-water reservoirs of the world: Gulf Coast Section SEPM 20th Annual Research Conference*, 40-60.

Beaubouef, R. & Abreu, V. 2010. MTCs of the Brazos-Trinity slope system; thoughts on the sequence stratigraphy of MTCs and their possible roles in shaping hydrocarbon traps *Submarine Mass Movements and Their Consequences*. Springer, 475-490.

Begg, S. & King, P. 1985. Modelling the effects of shales on reservoir performance: calculation of effective vertical permeability. *SPE Reservoir Simulation Symposium*. Society of Petroleum Engineers.

Bell, D., Stevenson, C.J., Kane, I.A., Hodgson, D.M. & Poyatos-Moré, M. 2018. Topographic Controls On the Development of Contemporaneous but Contrasting Basin-Floor Depositional Architectures. *Journal of Sedimentary Research*, **88**, 1166-1189.

Berndt, C., Bünz, S. & Mienert, J. 2003. Polygonal fault systems on the mid-Norwegian margin: a long-term source for fluid flow. *Geological Society, London, Special Publications*, **216**, 283-290.

Berndt, C., Costa, S., Canals, M., Camerlenghi, A., de Mol, B. & Saunders, M. 2012. Repeated slope failure linked to fluid migration: the Ana submarine landslide complex, Eivissa Channel, Western Mediterranean Sea. *Earth and Planetary Science Letters*, **319**, 65-74.

Boulesteix, K., Poyatos-Moré, M., Flint, S.S., Hodgson, D.M., Taylor, K.G. & Parry, G.R. 2019. Sedimentary facies and stratigraphic architecture of deep-water mudstones beyond the basin-floor fan sandstone pinchout.

Bouma, A. 1964. Turbidites. *Developments in sedimentology*, **3**, 247-256.

Bull, S., Cartwright, J. & Huuse, M. 2009. A review of kinematic indicators from mass-transport complexes using 3D seismic data. *Marine and Petroleum Geology*, **26**, 1132-1151.

Bünz, S., Mienert, J. & Berndt, C. 2003. Geological controls on the Storegga gas-hydrate system of the mid-Norwegian continental margin. *Earth and Planetary Science Letters*, **209**, 291-307.

Butler, R.W., Eggenhuisen, J.T., Haughton, P. & McCaffrey, W.D. 2016. Interpreting syndepositional sediment remobilization and deformation beneath submarine gravity flows; a kinematic boundary layer approach. *Journal of the Geological Society of London*, **173**, 46-58.

Cardona, S., Wood, L.J., Day-Stirrat, R.J. & Moscardelli, L. 2016. Fabric development and pore-throat reduction in a mass-transport deposit in the Jubilee Gas Field, Eastern Gulf of Mexico: consequences for the sealing capacity of MTDs *Submarine Mass Movements and their Consequences*. Springer, 27-37.

Cobain, S.L., Hodgson, D.M., Peakall, J. & Shiers, M.N. 2017. An integrated model of clastic injectites and basin floor lobe complexes: implications for stratigraphic trap plays. *Basin Research*, **29**, 816-835.

Coleman, J. & Prior, D.B. 1988. Mass wasting on continental margins. *Annual Review of Earth and Planetary Sciences*, **16**, 101-119.

Cook, A.E. & Sawyer, D.E. 2015. The mud-sand crossover on marine seismic data. *Geophysics*, **80**, A109-A114.

Davis, C., Haughton, P., McCaffrey, W., Scott, E., Hogg, N. & Kitching, D. 2009. Character and distribution of hybrid sediment gravity flow deposits from the outer Forties Fan, Palaeocene Central North Sea, UKCS. *Marine and Petroleum Geology*, **26**, 1919-1939.

Day-Stirrat, R.J., Flemings, P.B., You, Y. & van der Pluijm, B.A. 2013. Modification of mudstone fabric and pore structure as a result of slope failure: Ursa Basin, Gulf of Mexico. *Marine Geology*, **341**, 58-67.

De'Ath, N., DE'ATH, N. & SF, S. 1981. The geology of the Magnus oilfield.

Dodd, T.J., McCarthy, D.J. & Clarke, S.M. 2019. Clastic injectites, internal structures and flow regime during injection: the Sea Lion Injectite System, North Falkland Basin. *Sedimentology*.

Dominguez, R. 2007. Structural evolution of the Penguins cluster, UK northern North Sea. *Geological Society, London, Special Publications*, **292**, 25-48.

Dott, R. 1963. Dynamics of subaqueous gravity depositional processes. *American Association of Petroleum Geologists (AAPG) Bulletin*, **47**, 104-128.

Downey, M.W. 1984. Evaluating seals for hydrocarbon accumulations. *AAPG Bulletin*, **68**, 1752-1763.

Drinkwater, N. & Pickering, K. 2001. Architectural elements in a high-continuity sand-prone turbidite system, late Precambrian Kongsfjord Formation, northern Norway: Application to hydrocarbon reservoir characterization. *AAPG Bulletin*, **85**, 1731-1757.

Dugan, B. 2012. Petrophysical and consolidation behavior of mass transport deposits from the northern Gulf of Mexico, IODP Expedition 308. *Marine Geology*, **315**, 98-107.

Dykstra, M., Garyfalou, K., Kertznus, V., Kneller, B., Milana, J.P., Molinaro, M., Szuman, M. & Thompson, P. 2011. Mass-transport deposits: combining outcrop studies and seismic forward modeling

to understand lithofacies distributions, deformation, and their seismic expression. *SEPM Special Publication*, **96**, 293-310.

Eggenhuisen, J., McCaffrey, W., Haughton, P., Butler, R., Moore, I., Jarvie, A. & Hakes, W. 2010. Reconstructing large-scale remobilisation of deep-water deposits and its impact on sand-body architecture from cored wells: The Lower Cretaceous Britannia Sandstone Formation, UK North Sea. *Marine and Petroleum Geology*, **27**, 1595-1615.

Fisher, R.V. 1983. Flow transformations in sediment gravity flows. *Geology*, **11**, 273-274.

Flemings, P., Long, H., Dugan, B., Germaine, J., John, C., Behrmann, J.H., Sawyer, D. & Expedition, I. 2008. Pore pressure penetrometers document high overpressure near the seafloor where multiple submarine landslides have occurred on the continental slope, offshore Louisiana, Gulf of Mexico. *Earth and Planetary Science Letters*, **269**, 309-325.

Flint, S.S., Hodgson, D.M., Sixsmith, P.J., Grecula, M. & Wickens, H.D.V. 2007. Karoo Basin, South Africa: Deep-water Basin-floor and Slope Deposits of the Laingsburg Depocenter.

Fonnesu, M., Haughton, P., Felletti, F. & McCaffrey, W. 2015. Short length-scale variability of hybrid event beds and its applied significance. *Marine and Petroleum Geology*, **67**, 583-603.

Fonnesu, M., Felletti, F., Haughton, P.D., Patacci, M. & McCaffrey, W.D. 2018. Hybrid event bed character and distribution linked to turbidite system sub-environments: The North Apennine Gottero Sandstone (north-west Italy). *Sedimentology*, **65**, 151-190.

Fraser, S., Robinson, A., Johnson, H., Underhill, J., Kadolsky, D., Connell, R., Johannesson, P. & Ravnås, R. 2003. Upper Jurassic, in The Millennium Atlas: petroleum geology of the central and northern North Sea. London: Geological Society, 157–189.

Gabrielsen, R., Odinsen, T. & Grunnaleite, I. 1999. Structuring of the Northern Viking Graben and the Møre Basin; the influence of basement structural grain, and the particular role of the Møre-Trøndelag Fault Complex. *Marine and Petroleum Geology*, **16**, 443-465.

Galloway, W.E. 1998. Siliciclastic slope and base-of-slope depositional systems: component facies, stratigraphic architecture, and classification. *American Association of Petroleum Geologists (AAPG) bulletin*, **82**, 569-595.

Gamboa, D. & Alves, T.M. 2015. Three-dimensional fault meshes and multi-layer shear in mass-transport blocks: Implications for fluid flow on continental margins. *Tectonophysics*, **647**, 21-32.

Garland, C., Haughton, P., King, R. & Moulds, T. 1999. Capturing reservoir heterogeneity in a sand-rich submarine fan, Miller Field. *Geological Society, London, Petroleum Geology Conference series*. Geological Society of London, 1199-1208.

Goodall, I., Lofts, J., Mulcahy, M., Ashton, M. & Johnson, S. 1999. A sedimentological application of ultrasonic borehole images in complex lithologies: the Lower Kimmeridge Clay Formation, Magnus Field, UKCS. *Geological Society, London, Special Publications*, **159**, 203-225.

Grecula, M., Kattah, S., Akinsanmi, O., Uy, H., Hedeir, K., Osterloff, P., Maguire, K., Shiner, P., *et al.* 2008. Prediction of Reservoir Distribution and Quality in Tectonically Active NW Borneo Slope. *IPTC 2008: International Petroleum Technology Conference*. European Association of Geoscientists & Engineers, cp-148-00149.

Hampton, M. 1975. Competence of fine-grained debris flows. *Journal of Sedimentary Research*, **45**, 834-844.

Hansen, L., Janocko, M., Kane, I. & Kneller, B. 2017. Submarine channel evolution, terrace development, and preservation of intra-channel thin-bedded turbidites: Mahin and Avon channels, offshore Nigeria. *Marine Geology*, **383**, 146-167.

Haughton, P., Davis, C., McCaffrey, W. & Barker, S. 2009. Hybrid sediment gravity flow deposits–classification, origin and significance. *Marine and Petroleum Geology*, **26**, 1900-1918.

Haughton, P.D., Barker, S.P. & McCaffrey, W.D. 2003. 'Linked'debrites in sand-rich turbidite systems–origin and significance. *Sedimentology*, **50**, 459-482.

Hodgson, D.M. 2009. Distribution and origin of hybrid beds in sand-rich submarine fans of the Tanqua depocentre, Karoo Basin, South Africa. *Marine and Petroleum Geology*, **26**, 1940-1956.

Hodgson, D.M., Brooks, H.L., Ortiz-Karpf, A., Spychala, Y., Lee, D.R. and Jackson, C.L., 2019. Entrainment and abrasion of megaclasts during submarine landsliding and their impact on flow behaviour. Geological Society, London, Special Publications, **477**(1), 223-240.

Hurst, A. & Cartwright, J. 2007. Relevance of sand injectites to hydrocarbon exploration and production.

Jackson, C.A. & Johnson, H.D. 2009. Sustained turbidity currents and their interaction with debrite-related topography; Labuan Island, offshore NW Borneo, Malaysia. *Sedimentary Geology*, **219**, 77-96.

Jackson, M. & Muggeridge, A. 2000. Effect of discontinuous shales on reservoir performance during horizontal waterflooding. *SPE Journal*, **5**, 446-455.

Jackson, M., Hampson, G., Saunders, J., El-Sheikh, A., Graham, G. & Massart, B. 2014. Surface-based reservoir modelling for flow simulation. *Geological Society, London, Special Publications*, **387**, 271-292.

Jacquemyn, C., Jackson, M.D. & Hampson, G.J. 2019. Surface-based geological reservoir modelling using grid-free NURBS curves and surfaces. *Mathematical Geosciences*, **51**, 1-28.

Jennette, D.C., Garfield, T.R., Mohrig, D.C. & Cayley, G.T. 2000. The interaction of shelf accommodation, sediment supply and sea level in controlling the facies, architecture and sequence stacking patterns of the Tay and Forties/Sele basin-floor fans, Central North Sea. *Deep-Water Reservoirs of the World. GCSSEPM Foundation 20th Annual Research Conference Proceedings*, 3-6.

Jobe, Z.R., Lowe, D.R. & Morris, W.R. 2012. Climbing-ripple successions in turbidite systems: depositional environments, sedimentation rates and accumulation times. *Sedimentology*, **59**, 867-898.

Johns, C.R. & Andrews, I.J. 1985. The petroleum geology of the Unst Basin, North Sea. *Marine and Petroleum Geology*, **2**, 361-372.

Kaldi, J. & Atkinson, C. 1997. Evaluating seal potential: example from the Talang Akar Formation, offshore northwest Java, Indonesia. *Memoirs, American Association of Petroleum Geologist*, 85-102.

Kane, I.A., Pontén, A.S., Vangdal, B., Eggenhuisen, J.T., Hodgson, D.M. & Spychala, Y.T. 2017. The stratigraphic record and processes of turbidity current transformation across deep-marine lobes. *Sedimentology*.

Kendrick, J. 1998. Turbidite reservoir architecture in the Gulf of Mexico-insights from field development. *EAGE/AAPG 3rd Research Symposium-Developing and Managing Turbidite Reservoirs*. European Association of Geoscientists & Engineers, cp-100-00003.

Kendrick, J.W. 2000. Turbidite Reservoir Architecture in the Northern Gulf of Mexico Deepwater: Insights from the Development of Auger, Tahoe, and Ram/Powell Fields. *In*: Weimer, P. (ed) *Deep-Water Reservoirs of the World*. SEPM Society for Sedimentary Geology.

Kneller, B., Dykstra, M., Fairweather, L. & Milana, J.P. 2016. Mass-transport and slope accommodation: implications for turbidite sandstone reservoirs. *AAPG Bulletin*, **100**, 213-235.

Kneller, B.C. & Branney, M.J. 1995. Sustained high-density turbidity currents and the deposition of thick massive sands. *Sedimentology*, **42**, 607-616.

Koša, E. 2007. Differential subsidence driving the formation of mounded stratigraphy in deep-water sediments; Palaeocene, central North Sea. *Marine and Petroleum Geology*, **24**, 632-652.

Lake, L.W. 1989. Enhanced oil recovery.

Lancaster, S. & Whitcombe, D. 2000. Fast-track 'coloured'inversion *SEG Technical Program Expanded Abstracts 2000*. Society of Exploration Geophysicists, 1572-1575.

Lee, M. & Hwang, Y. 1993. Tectonic evolution and structural styles of the East Shetland Basin. *Geological Society, London, Petroleum Geology Conference series*. Geological Society of London, 1137-1149.

Lowe, D., Guy, M. & Palfrey, A. 2003. Facies of slurry-flow deposits, Britannia Formation (Lower Cretaceous), North Sea: implications for flow evolution and deposit geometry. *Sedimentology*, **50**, 45-80.

Lowe, D.R. 1982. Sediment gravity flows: II Depositional models with special reference to the deposits of high-density turbidity currents. *Journal of Sedimentary Research*, **52**.

Lowe, D.R. & Guy, M. 2000. Slurry-flow deposits in the Britannia Formation (Lower Cretaceous), North Sea: a new perspective on the turbidity current and debris flow problem. *Sedimentology*, **47**, 31-70.

MacGregor, A., Trussell, P., Lauver, S., Bedrock, M., Bryce, J. & Moulds, T. 2005. The Magnus Field: extending field life through good reservoir management and enhanced oil recovery. *Geological Society, London, Petroleum Geology Conference series*. Geological Society of London, 469-475.

Mattern, F. 2005. Ancient sand-rich submarine fans: depositional systems, models, identification, and analysis. *Earth-Science Reviews*, **70**, 167-202.

Mayall, M., Yeilding, C., Oldroyd, J., Pulham, A. & Sakurai, S. 1992. Facies in a Shelf-Edge Delta--An Example from the Subsurface of the Gulf of Mexico, Middle Pliocene, Mississippi Canyon, Block 109 (1). *American Association of Petroleum Geologists (AAPG) bulletin*, **76**, 435-448.

McCaffrey, W. & Kneller, B. 2001. Process controls on the development of stratigraphic trap potential on the margins of confined turbidite systems and aids to reservoir evaluation. *AAPG Bulletin*, **85**, 971-988.

McLeod, A. & Underhill, J. 1999. Processes and products of footwall degradation, northern Brent Field, Northern North Sea. *Geological Society, London, Petroleum Geology Conference series*. Geological Society of London, 91-106.

Meckel, L. 2011. Reservoir characteristics and classification of sand-prone submarine mass-transport deposits. *SEPM Special Publication*, **96**, 432-452.

Melnikova, Y., Jacquemyn, C., Osman, H., Salinas, P., Gorman, G., Hampson, G. & Jackson, M. 2016. Reservoir modelling using parametric surfaces and dynamically adaptive fully unstructured grids. *ECMOR XV-15th European Conference on the Mathematics of Oil Recovery*. European Association of Geoscientists & Engineers, cp-494-00147.

Mohrig, D., Ellis, C., Parker, G., Whipple, K.X. & Hondzo, M. 1998. Hydroplaning of subaqueous debris flows. *Geological Society of America Bulletin*, **110**, 387-394.

Morris, P., Payne, S. & Richards, D. 1999. Micropalaeontological biostratigraphy of the Magnus Sandstone Member (Kimmeridgian-Early Volgian), Magnus Field, UK North Sea. *Geological Society, London, Special Publications*, **152**, 55-73.

Moscardelli, L., Wood, L. & Mann, P. 2006. Mass-transport complexes and associated processes in the offshore area of Trinidad and Venezuela. *AAPG Bulletin*, **90**, 1059-1088.

Mulder, T. & Cochonat, P. 1996. Classification of offshore mass movements. *Journal of Sedimentary Research*, **66**, 43-57.

Mutti, E. 1977. Distinctive thin-bedded turbidite facies and related depositional environments in the Eocene Hecho Group (South-central Pyrenees, Spain). *Sedimentology*, **24**, 107-131.

Mutti, E. & Normark, W.R. 1987. Comparing examples of modern and ancient turbidite systems: problems and concepts *Marine clastic sedimentology*. Springer, 1-38.

Nardin, T.R. 1979. A review of mass movement processes sediment and acoustic characteristics, and contrasts in slope and base-of-slope systems versus canyon-fan-basin floor systems. *SEPM Special Publication*.

Nemec, W. 1990. Aspects of sediment movement on steep delta slopes. *Special Publication, International Association of Sedimentologists, Coarse-grained deltas*, **10**, 29-73.

Nemec, W., Steel, R., Gjelberg, J., Collinson, J., Prestholm, E. & Oxnevad, I. 1988. Anatomy of collapsed and re-established delta front in Lower Cretaceous of eastern Spitsbergen: gravitational sliding and sedimentation processes. *American Association of Petroleum Geologists (AAPG) bulletin*, **72**, 454-476.

O'Connor, S. & Walker, D. 1993. Paleocene reservoirs of the Everest trend. *Geological Society, London, Petroleum Geology Conference series*. Geological Society of London, 145-160.

Ortiz-Karpf, A., Hodgson, D. & McCaffrey, W. 2015. The role of mass-transport complexes in controlling channel avulsion and the subsequent sediment dispersal patterns on an active margin: the Magdalena Fan, offshore Colombia. *Marine and Petroleum Geology*, **64**, 58-75.

Ortiz-Karpf, A., Hodgson, D.M., Jackson, C.A.L. & McCaffrey, W.D. 2016. Mass-transport complexes as markers of deep-water fold-and-thrust belt evolution: insights from the southern Magdalena fan, offshore Colombia. *Basin Research*, http://doi.org/10.1111/bre.12208.

Ortiz-Karpf, A., Hodgson, D.M., Jackson, C.A.-L. & McCaffrey, W.D. 2017. Influence of Seabed Morphology and Substrate Composition On Mass-Transport Flow Processes and Pathways: Insights From the Magdalena Fan, Offshore Colombia. *Journal of Sedimentary Research*, **87**, 189-209.

Osborne, M.J. & Swarbrick, R.E. 1997. Mechanisms for generating overpressure in sedimentary basins: a reevaluation. *AAPG Bulletin*, **81**, 1023-1041.

Partington, M., Copestake, P., Mitchener, B.a. & Underhill, J.R. 1993. Biostratigraphic calibration of genetic stratigraphic sequences in the Jurassic–lowermost Cretaceous (Hettangian to Ryazanian) of the North Sea and adjacent areas. *Geological Society, London, Petroleum Geology Conference series*. Geological Society of London, 371-386.

Passey, Q.R., Dahlberg, K.E., Sullivan, K., Yin, H., Brackett, B., Xiao, Y. & Guzman-Garcia, A.G. 2006. *Petrophysical evaluation of hydrocarbon pore-thickness in thinly bedded clastic reservoirs: AAPG Archie Series, no. 1*. Aapg.

Pickering, K.T. & Corregidor, J. 2005. Mass-transport complexes (MTCs) and tectonic control on basin-floor submarine fans, middle Eocene, south Spanish Pyrenees. *Journal of Sedimentary Research*, **75**, 761-783.

Pierce, C.S., Haughton, P.D., Shannon, P.M., Pulham, A.J., Barker, S.P. & Martinsen, O.J. 2018. Variable character and diverse origin of hybrid event beds in a sandy submarine fan system, Pennsylvanian Ross Sandstone Formation, western Ireland. *Sedimentology*, **65**, 952-992.

Piper, D., Pirmez, C., Manley, P., Long, D., Flood, R., Normark, W. & Showers, W. 1997. Mass-transport deposits of the Amazon Fan.

Piper, D.J. & Normark, W.R. 1983. Turbidite depositional patterns and flow characteristics, Navy submarine fan, California Borderland. *Sedimentology*, **30**, 681-694.

Porten, K.W., Kane, I.A., Warchoł, M.J. & Southern, S.J. 2016. A sedimentological process-based approach to depositional reservoir quality of deep-marine sandstones: an example from the Springar Formation, northwestern Vøring Basin, Norwegian Sea. *Journal of Sedimentary Research*, **86**, 1269-1286.

Prather, B.E. 2003. Controls on reservoir distribution, architecture and stratigraphic trapping in slope settings. *Marine and Petroleum Geology*, **20**, 529-545.

Prélat, A., Hodgson, D. & Flint, S. 2009. Evolution, architecture and hierarchy of distributary deep-water deposits: a high-resolution outcrop investigation from the Permian Karoo Basin, South Africa. *Sedimentology*, **56**, 2132-2154.

Prélat, A., Hodgson, D.M., Hall, M., Jackson, C.A.-L., Baunack, C. & Tveiten, B. 2015. Constraining sub-seismic deep-water stratal elements with electrofacies analysis; A case study from the Upper Cretaceous of the Måløy Slope, offshore Norway. *Marine and Petroleum Geology*, **59**, 268-285.

Pyles, D.R. 2007. Architectural elements in a ponded submarine fan, Carboniferous Ross Sandstone, western Ireland.

Pyles, D.R. & Jennette, D. 2009. Geometry and architectural associations of co-genetic debrite–turbidite beds in basin-margin strata, Carboniferous Ross Sandstone (Ireland): Applications to reservoirs located on the margins of structurally confined submarine fans. *Marine and Petroleum Geology*, **26**, 1974-1996.

Ravnås, R. & Steel, R.J. 1997. Contrasting styles of Late Jurassic syn-rift turbidite sedimentation: a comparative study of the Magnus and Oseberg areas, northern North Sea. *Marine and Petroleum Geology*, **14**, 417-449.

Ray, F., Pinnock, S., Katamish, H. & Turnbull, J. 2010. The Buzzard Field: anatomy of the reservoir from appraisal to production. *Geological Society, London, Petroleum Geology Conference series*. Geological Society of London, 369-386.

Reading, H.G. & Richards, M. 1994. Turbidite systems in deep-water basin margins classified by grain size and feeder system. *American Association of Petroleum Geologists (AAPG) bulletin*, **78**, 792-822.

Riboulot, V., Cattaneo, A., Sultan, N., Garziglia, S., Ker, S., Imbert, P. & Voisset, M. 2013. Sea-level change and free gas occurrence influencing a submarine landslide and pockmark formation and distribution in deepwater Nigeria. *Earth and Planetary Science Letters*, **375**, 78-91.

Sarkar, S., Berndt, C., Minshull, T.A., Westbrook, G.K., Klaeschen, D., Masson, D.G., Chabert, A. & Thatcher, K.E. 2012. Seismic evidence for shallow gas-escape features associated with a retreating gas hydrate zone offshore west Svalbard. *Journal of Geophysical Research: Solid Earth*, **117**.

Satur, N. & Hurst, A. 2007. Sand-injection Structures in Deep-water Sandstones from the Ty Formation (Paleocene), Sleipner st Field, Norwegian North Sea.

Sawyer, D.E., Flemings, P.B., Dugan, B. & Germaine, J.T. 2009. Retrogressive failures recorded in mass transport deposits in the Ursa Basin, Northern Gulf of Mexico. *Journal of Geophysical Research: Solid Earth*, **114**.

Sawyer, D.E., Flemings, P.B., Buttles, J. & Mohrig, D. 2012. Mudflow transport behavior and deposit morphology: Role of shear stress to yield strength ratio in subaqueous experiments. *Marine Geology*, **307**, 28-39.

Shepherd, M. 1991. The Magnus Field, Block 211/7a, 12a, UK North Sea. *Geological Society, London, Memoirs*, **14**, 153-157.

Shepherd, M., Kearney, C. & Milne, J. 1990. Magnus field.

Sobiesiak, M.S., Kneller, B., Alsop, G.I. & Milana, J.P. 2018. Styles of basal interaction beneath mass transport deposits. *Marine and Petroleum Geology*, **98**, 629-639.

Southern, S.J., Kane, I.A., Warchoł, M.J., Porten, K.W. & McCaffrey, W.D. 2017. Hybrid event beds dominated by transitional-flow facies: character, distribution and significance in the Maastrichtian Springar Formation, north-west Vøring Basin, Norwegian Sea. *Sedimentology*, **64**, 747-776.

Soutter, E.L., Kane, I.A., Fuhrmann, A., Cumberpatch, Z.A. & Huuse, M. 2019. The stratigraphic evolution of onlap in siliciclastic deep-water systems: Autogenic modulation of allogenic signals. *Journal of Sedimentary Research*, **89**, 890-917.

Spychala, Y.T., Hodgson, D.M., Stevenson, C.J. & Flint, S.S. 2017a. Aggradational lobe fringes: The influence of subtle intrabasinal seabed topography on sediment gravity flow processes and lobe stacking patterns. *Sedimentology*, **64**, 582-608.

Spychala, Y.T., Hodgson, D.M., Prélat, A., Kane, I.A., Flint, S.S. & Mountney, N.P. 2017b. Frontal and lateral submarine lobe fringes: comparing sedimentary facies, architecture and flow processes. *Journal of Sedimentary Research*, **87**, 75-96.

Stevenson, C.J., Jackson, C.A.-L., Hodgson, D.M., Hubbard, S.M. & Eggenhuisen, J.T. 2015. Deep-water sediment bypass. *Journal of Sedimentary Research*, **85**, 1058-1081.

Stevenson, C.J., Peakall, J., Hodgson, D., M, Bell, D. & Privat, A. 2020. Tb or not Tb: Banding in Turbidite Sandstones. *Sedimentology*, **In review**.

Steventon, M.J., Jackson, C.A.L., Hodgson, D.M. & Johnson, H.D. 2019. Strain analysis of a seismically imaged mass-transport complex, offshore Uruguay. *Basin Research*, **31**, 600-620.

Steventon, M.J., Jackson, C.A., Hodgson, D.M. and Johnson, H.D., 2020. Lateral variability of shelf-edge and basin-floor deposits, Santos Basin, offshore Brazil. *Journal of Sedimentary Research*, **90**, 1198-1221.

Stow, D. & Piper, D. 1984. Deep-water fine-grained sediments: facies models. *Geological Society, London, Special Publications*, **15**, 611-646.

Strachan, L.J. 2002. Slump-initiated and controlled syndepositional sandstone remobilization: an example from the Namurian of County Clare, Ireland. *Sedimentology*, **49**, 25-41.

Sumner, E.J., Talling, P.J. & Amy, L.A. 2009. Deposits of flows transitional between turbidity current and debris flow. *Geology*, **37**, 991-994.

Sun, Q. & Alves, T. 2020. Petrophysics of fine-grained mass-transport deposits: A critical review. *Journal of Asian Earth Sciences*, 104291.

Sun, Q., Alves, T., Xie, X., He, J., Li, W. & Ni, X. 2017. Free gas accumulations in basal shear zones of mass-transport deposits (Pearl River Mouth Basin, South China Sea): An important geohazard on continental slope basins. *Marine and Petroleum Geology*, **81**, 17-32.

Talling, P., Amy, L.A., Wynn, R., Peakall, J. & Robinson, M. 2004. Beds comprising debrite sandwiched within co-genetic turbidite: origin and widespread occurrence in distal depositional environments. *Sedimentology*, **51**, 163-194.

Talling, P.J. 2013. Hybrid submarine flows comprising turbidity current and cohesive debris flow: Deposits, theoretical and experimental analyses, and generalized models. *Geosphere*, **9**, 460-488.

Talling, P.J., Masson, D.G., Sumner, E.J. & Malgesini, G. 2012. Subaqueous sediment density flows: depositional processes and deposit types. *Sedimentology*, **59**, 1937-2003.

Tappin, D., McNeil, L., Henstock, T. & Mosher, D. 2007. Mass wasting processes-offshore Sumatra *Submarine mass movements and their consequences*. Springer, 327-336.

Thomas, D. & Coward, M. 1995. Late Jurassic-Early Cretaceous inversion of the northern East Shetland Basin, northern North Sea. *Oceanographic Literature Review*, **11**, 982.

Tripsanas, E.K., Piper, D.J., Jenner, K.A. & Bryant, W.R. 2008. Submarine mass-transport facies: new perspectives on flow processes from cores on the eastern North American margin. *Sedimentology*, **55**, 97-136.

Underhill, J.R., Sawyer, M.J., Hodgson, P., Shallcross, M.D. & Gawthorpe, R.L. 1997. Implications of fault scarp degradation for Brent Group prospectivity, Ninian Field, northern North Sea. *AAPG Bulletin*, **81**, 999-1022.

Walker, R.G. 1985. Mudstones and thin-bedded turbidites associated with the Upper Cretaceous Wheeler Gorge conglomerates, California; a possible channel-levee complex. *Journal of Sedimentary Research*, **55**, 279-290.

Walker, R.G. & Mutti, E. 1973. Part IV. Turbidite facies and facies associations.

Weimer, P. 1989. Sequence stratigraphy of the Mississippi Fan (Plio-Pleistocene), Gulf of Mexico. *Geo-Marine Letters*, **9**, 185-272.

Welbon, A., Brockbank, P., Brunsden, D. & Olsen, T. 2007. Characterizing and producing from reservoirs in landslides: Challenges and opportunities. *Geological Society, London, Special Publications*, **292**, 49-74.

Wu, N., Jackson, C.A.-L., Johnson, H. & Hodgson, D.M. 2019. Lithological, petrophysical and seal properties of mass-transport complexes (MTCs), northern Gulf of Mexico.

Yamamoto, Y. & Sawyer, D.E. 2012. Systematic Spatial Variations in the Fabric and Physical Properties of Mass-Transport Deposits in the Ursa Region, Northern Gulf of Mexico *Submarine Mass Movements and Their Consequences*. Springer, 649-658.

Yielding, G. 1990. Footwall uplift associated with Late Jurassic normal faulting in the northern North Sea. *Journal of the Geological Society*, **147**, 219-222.

Ziegler, P. 1990. Tectonic and palaeogeographic development of the North Sea rift system. *Tectonic evolution of the North Sea rifts*, 1-36.

figure 1

Click here to access/download;figure;Fig.1.pdf

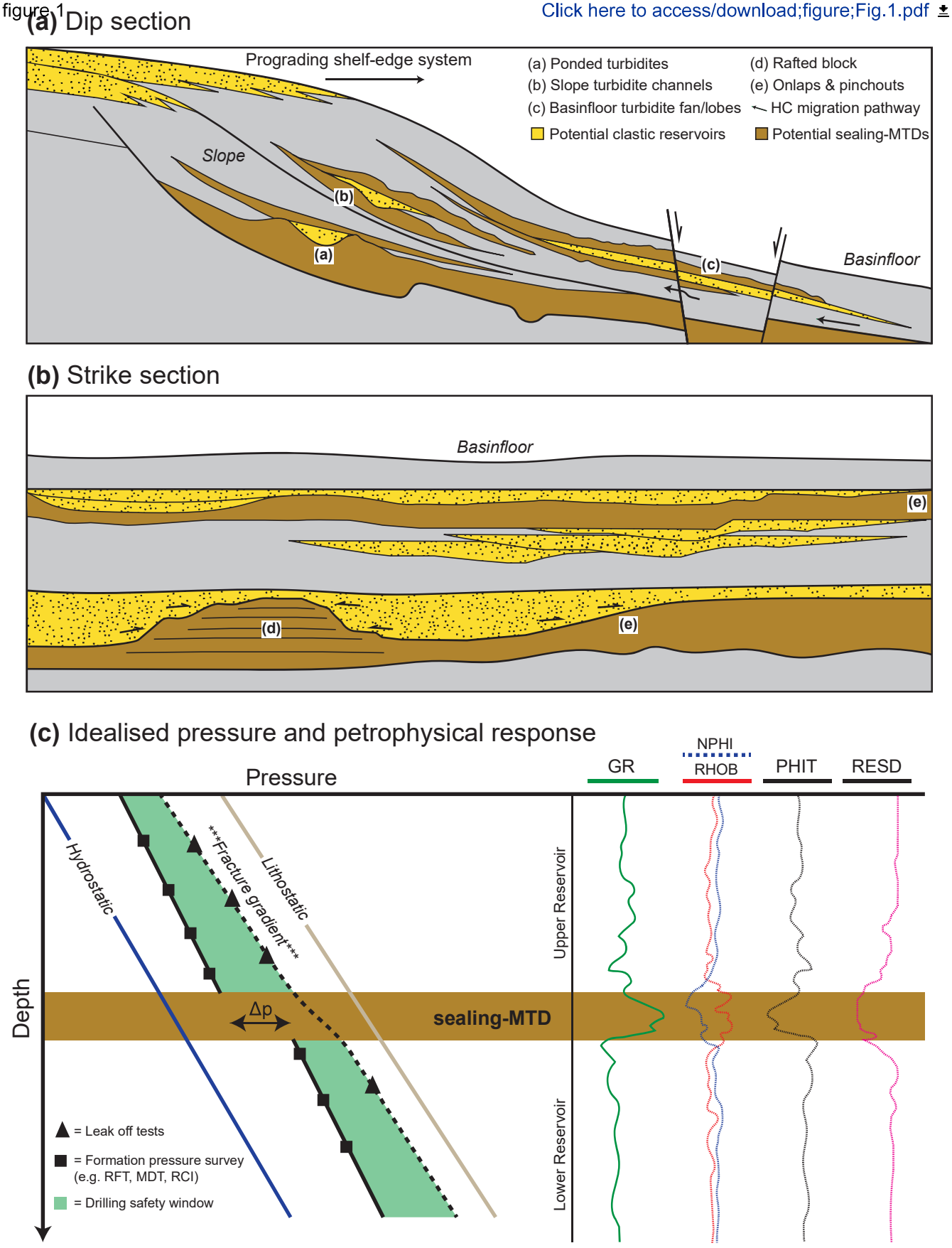

figure 2

Click here to access/download;figure;Fig.2.pdf

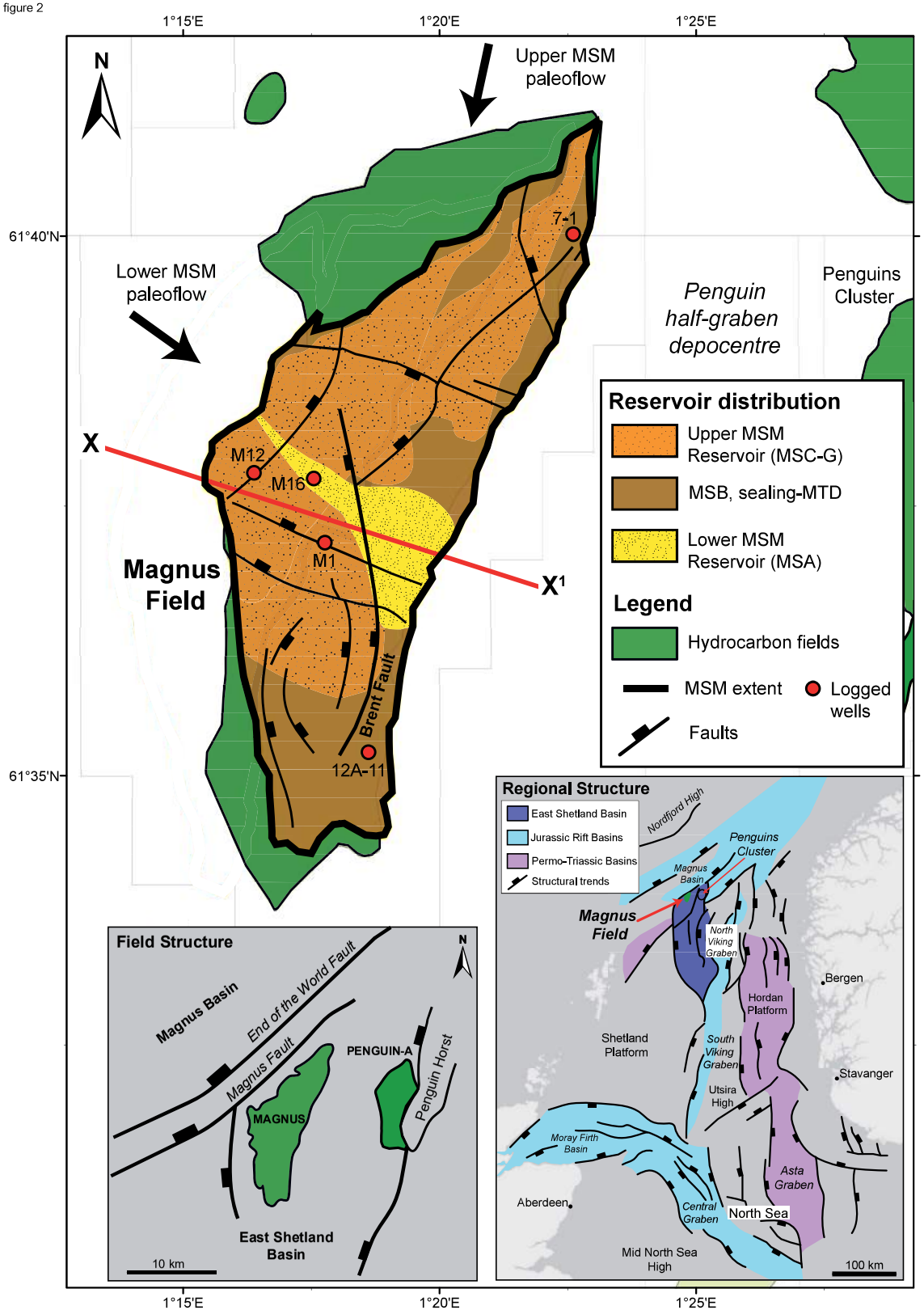

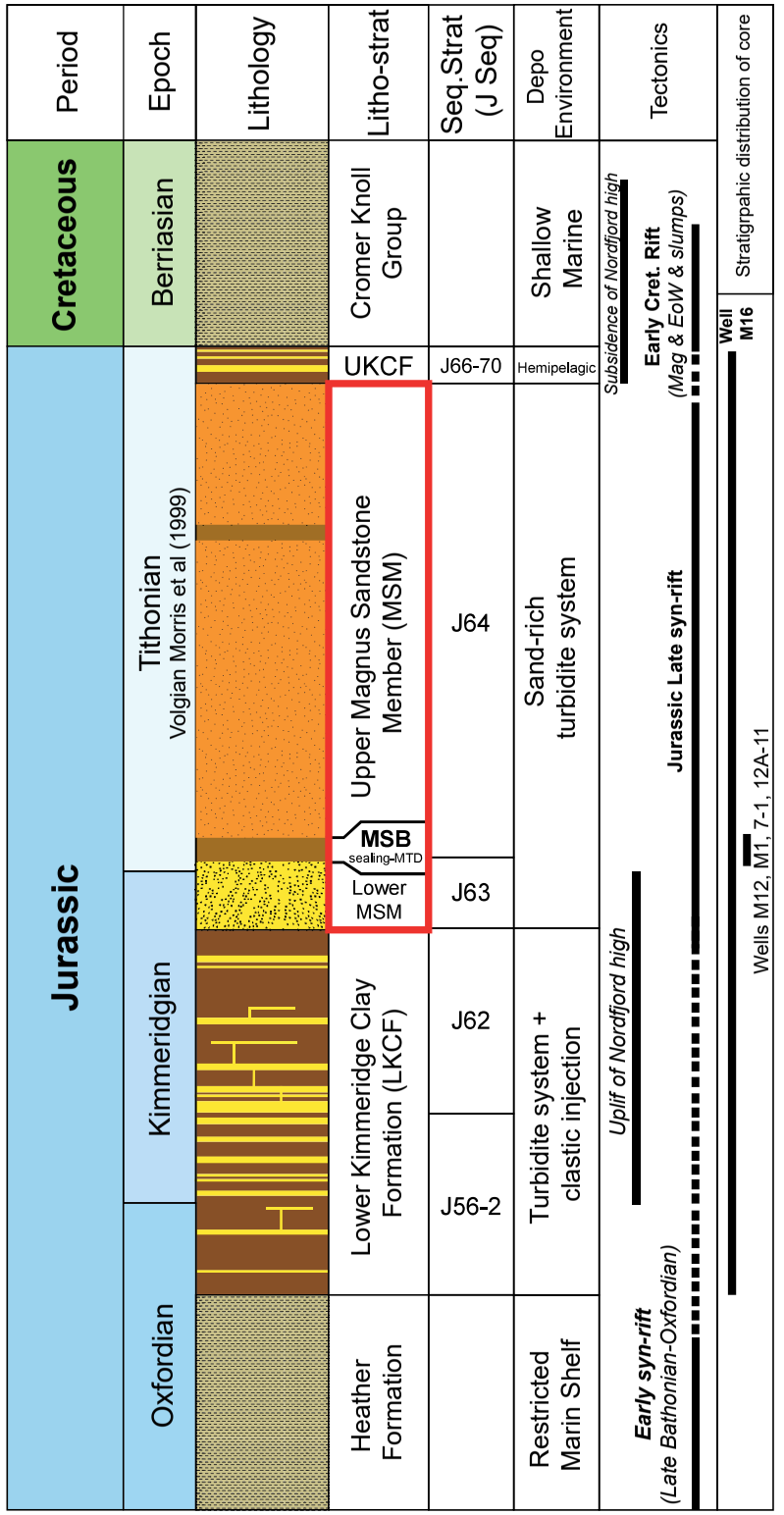

figure 4

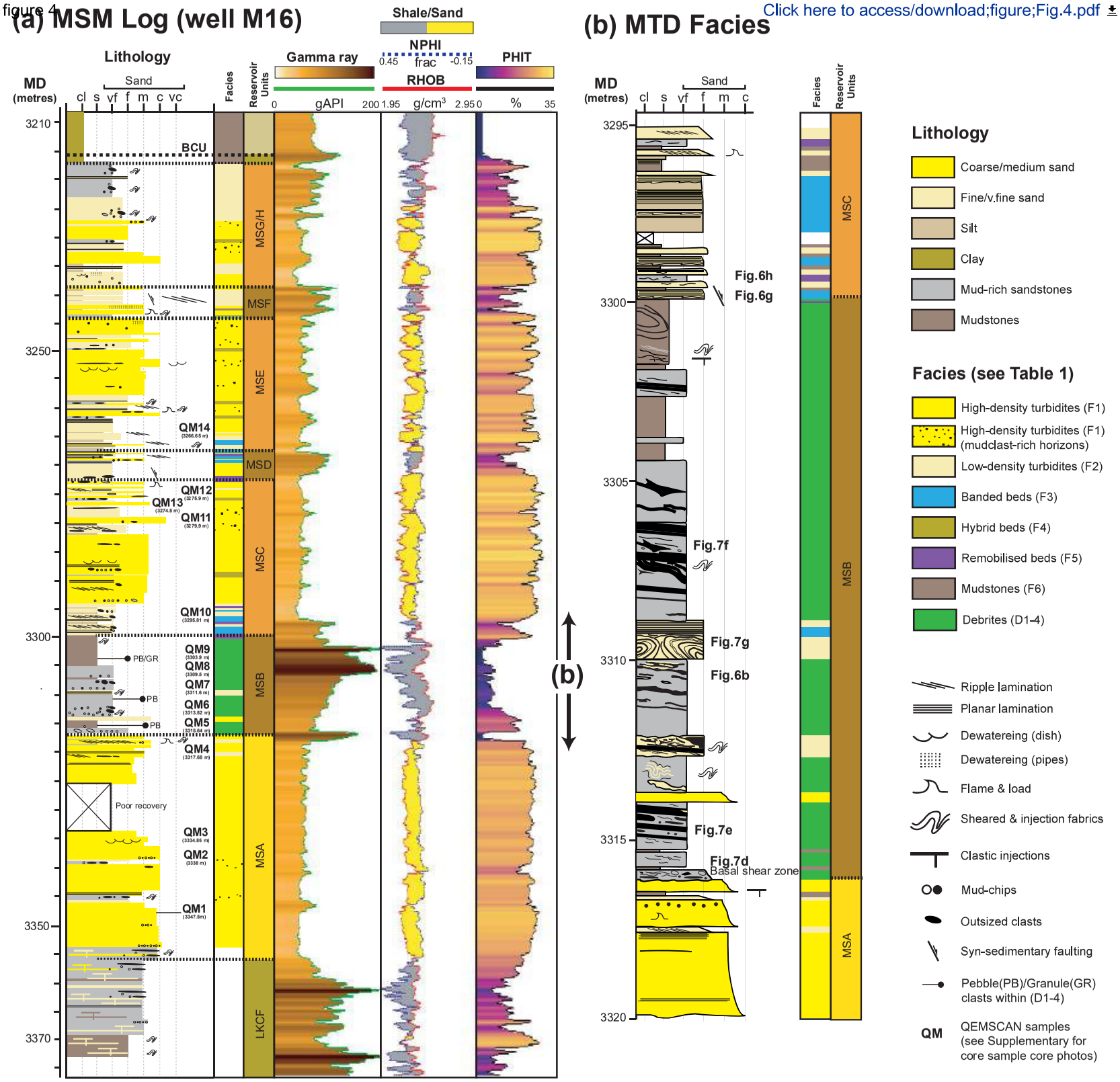

Figure 3

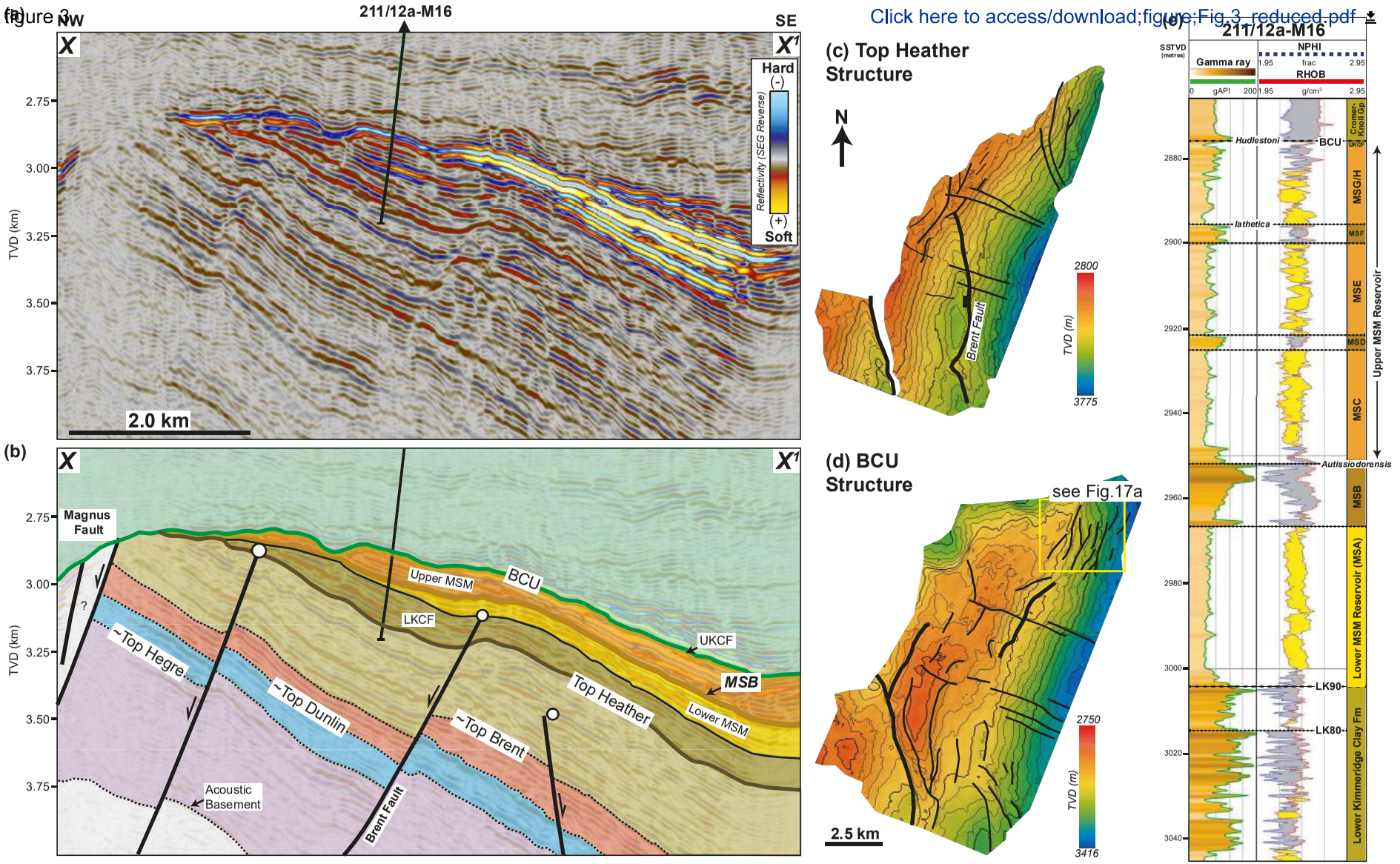

figure 5

Click here to access/download;figure;Fig.5_reduced.pdf

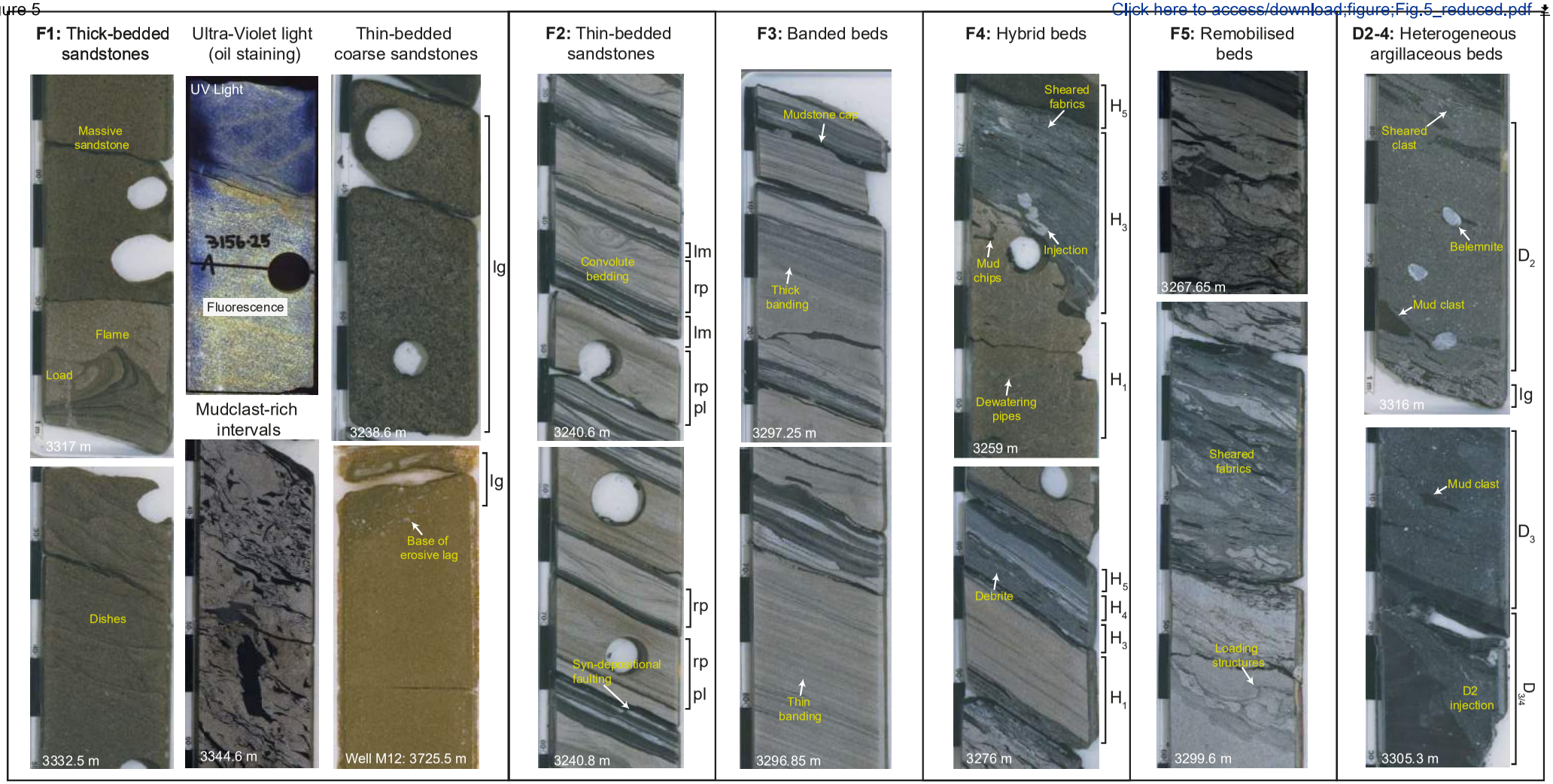

figure 6

Longitudinal flow transformation

Click here to access/download;figure;Fig.6_reduced.pdf

Updip Immature → *Central-Southern MSB* Increased runout distance → **Downdip** Mature → *Northern MSB* Injectite fabrics (D5)

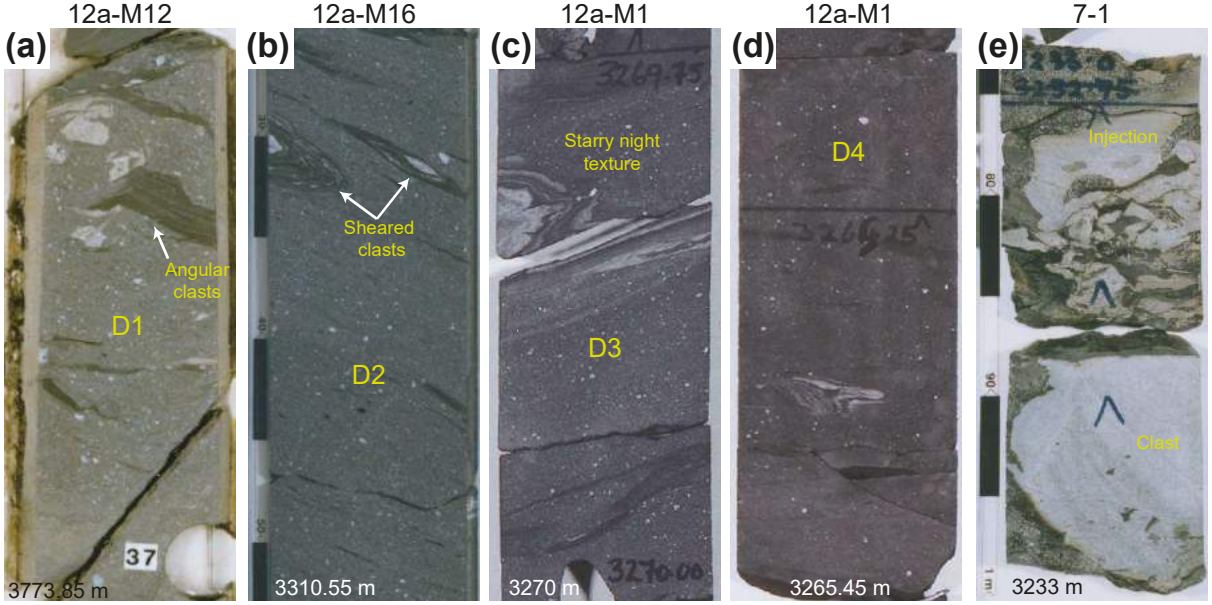

Transition from MSB to MSC

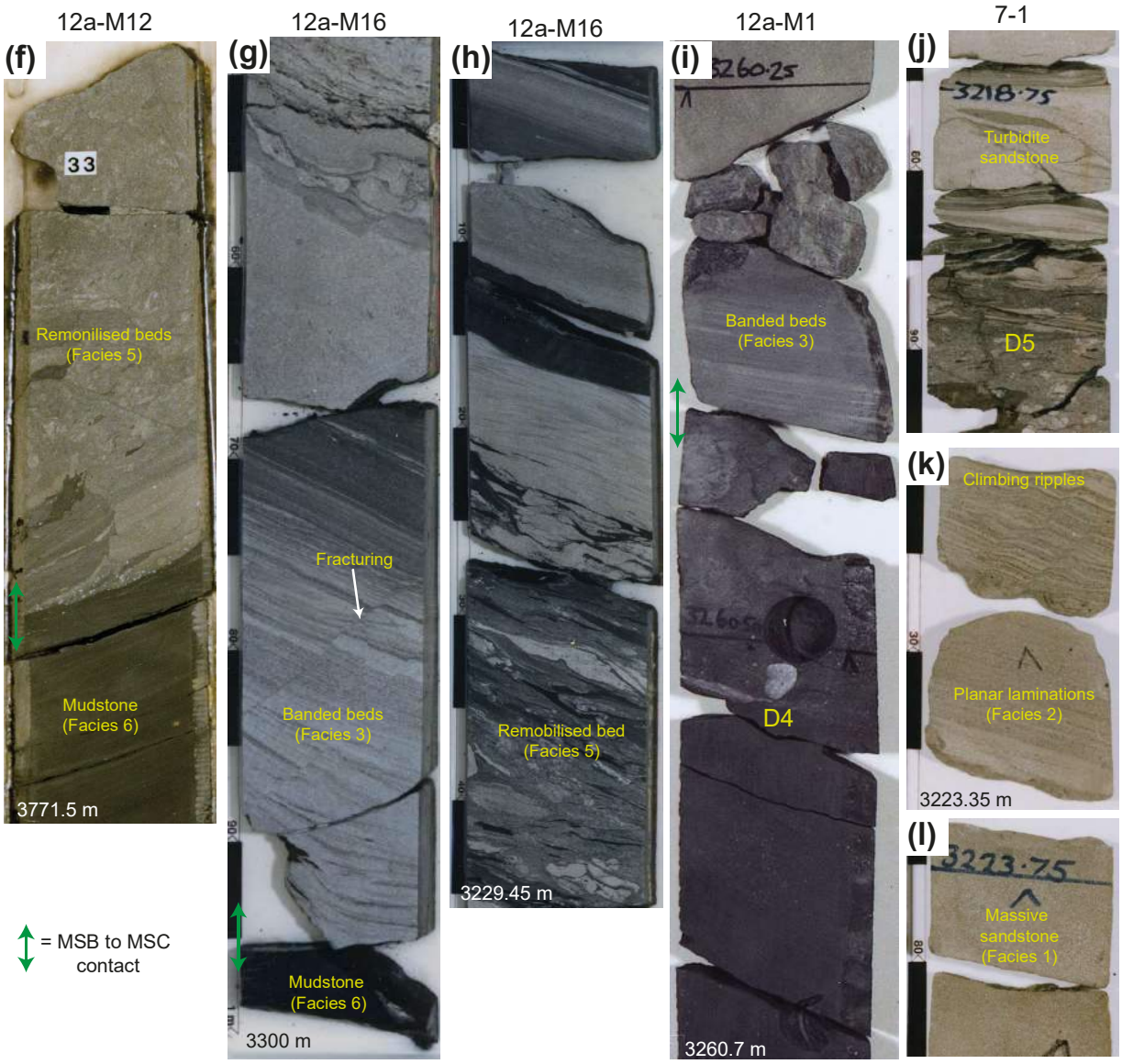

figure 7

Click here to access/download;figure;Fig.7_reduced.pdf

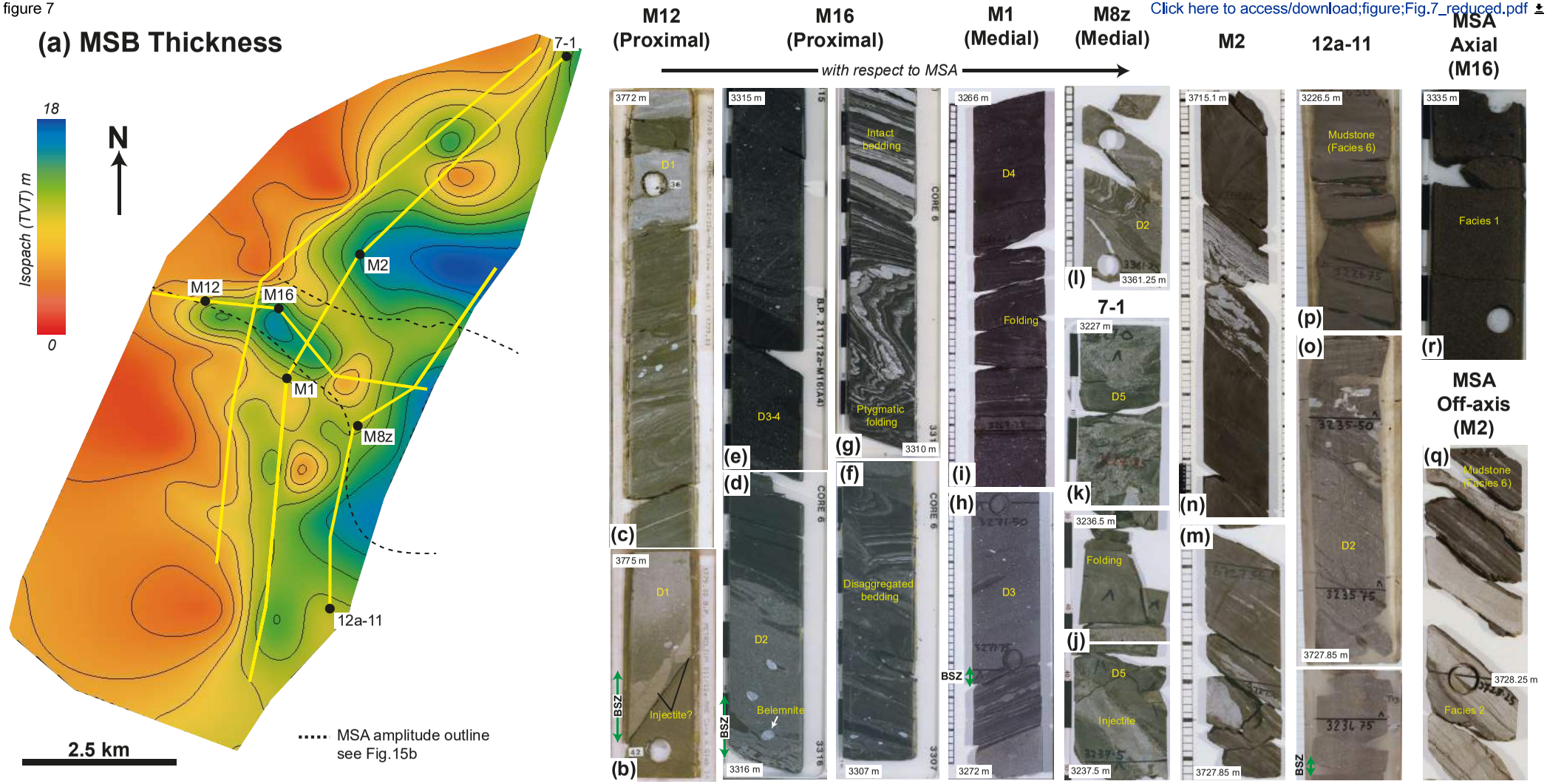

figure

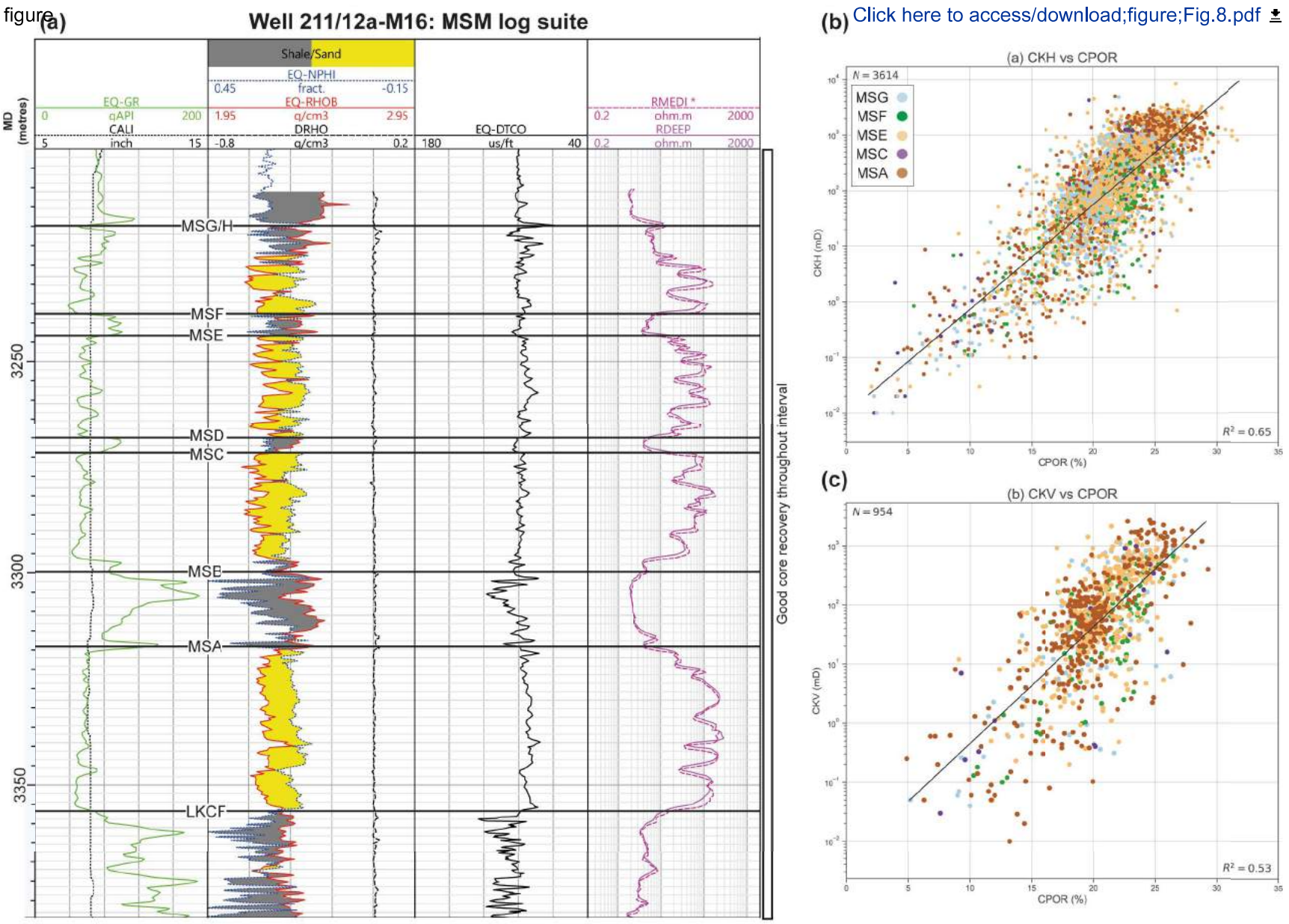

Click here to access/download;figure;Fig.8.pdf

figure 9 part 1

Click here to access/download;figure;Fig.9_part_1.pdf

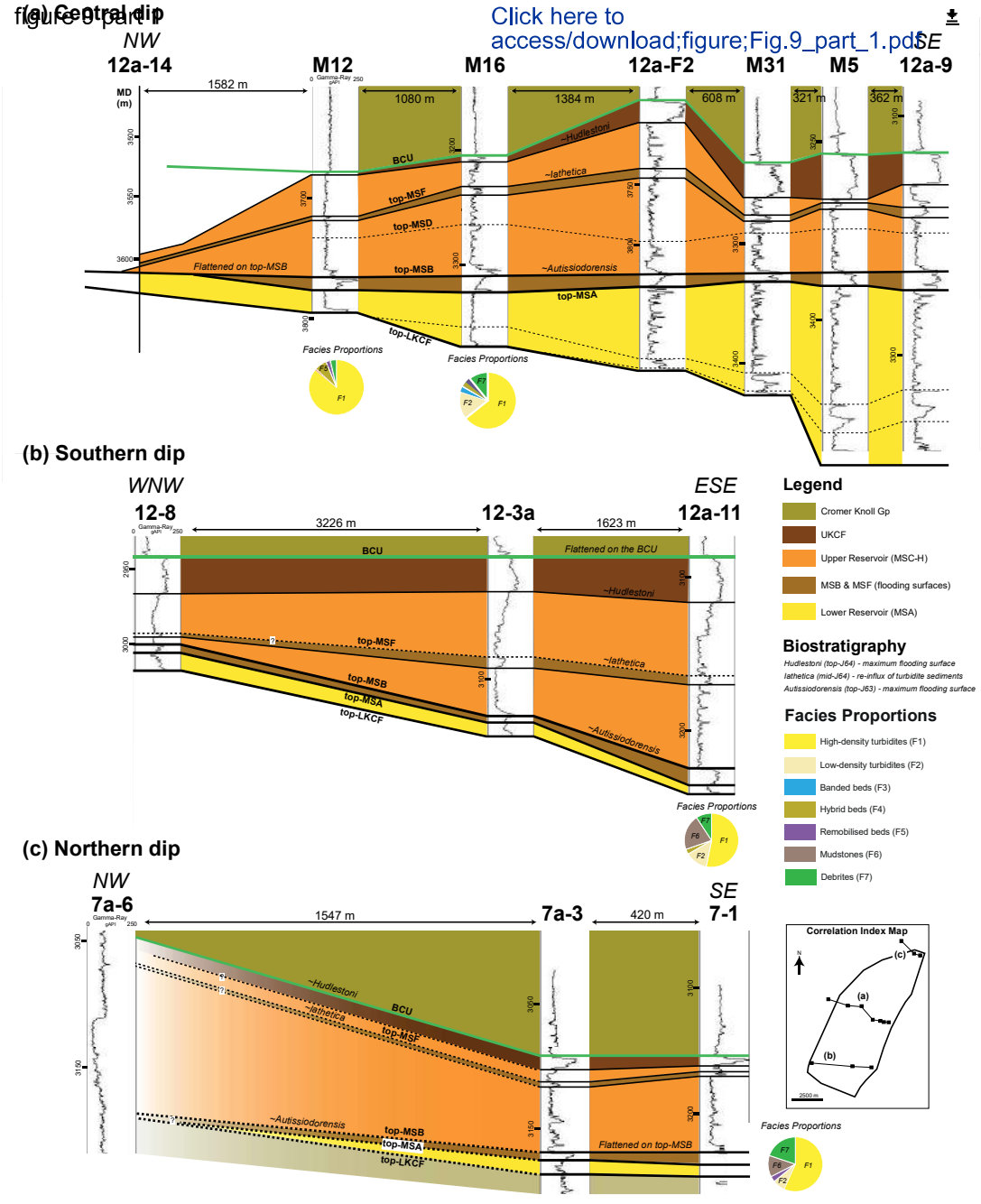

figure 9 part 2

Click here to access/download;figure;Fig.9_part2

(d) Upper slope

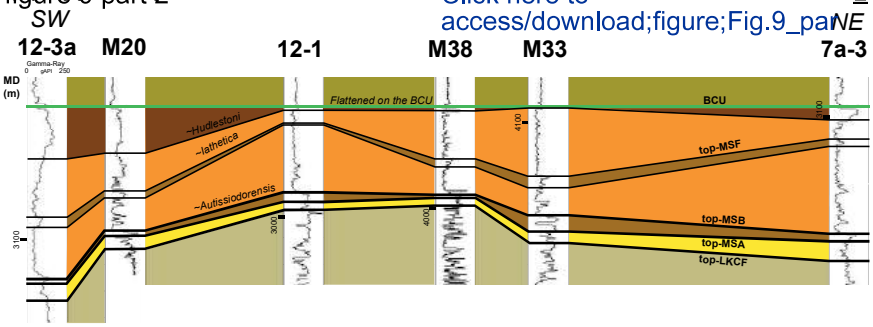

(e) Mid slope

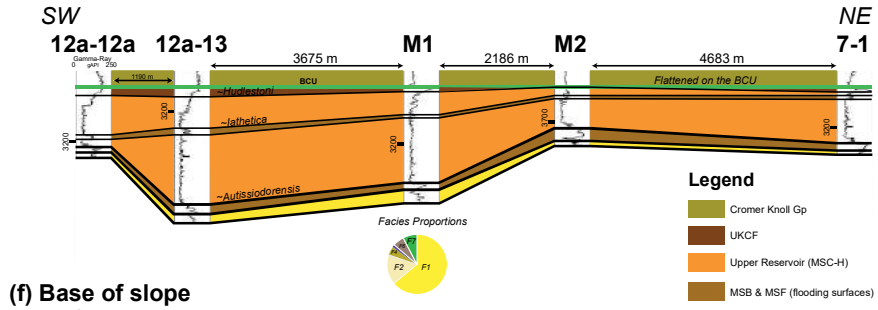

(f) Base of slope

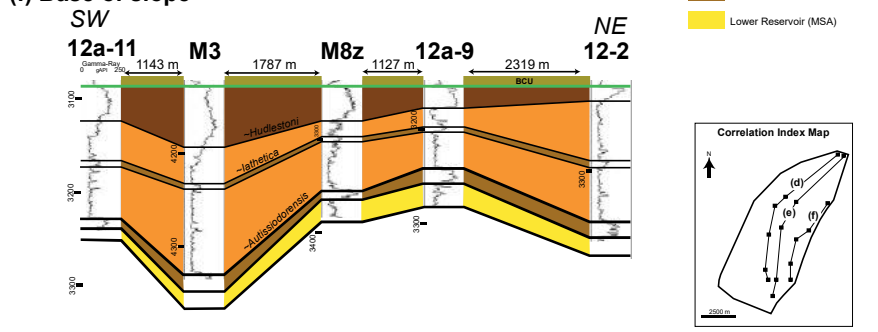

figure 10

Click here to access/download:figure:Fig 10.pdf

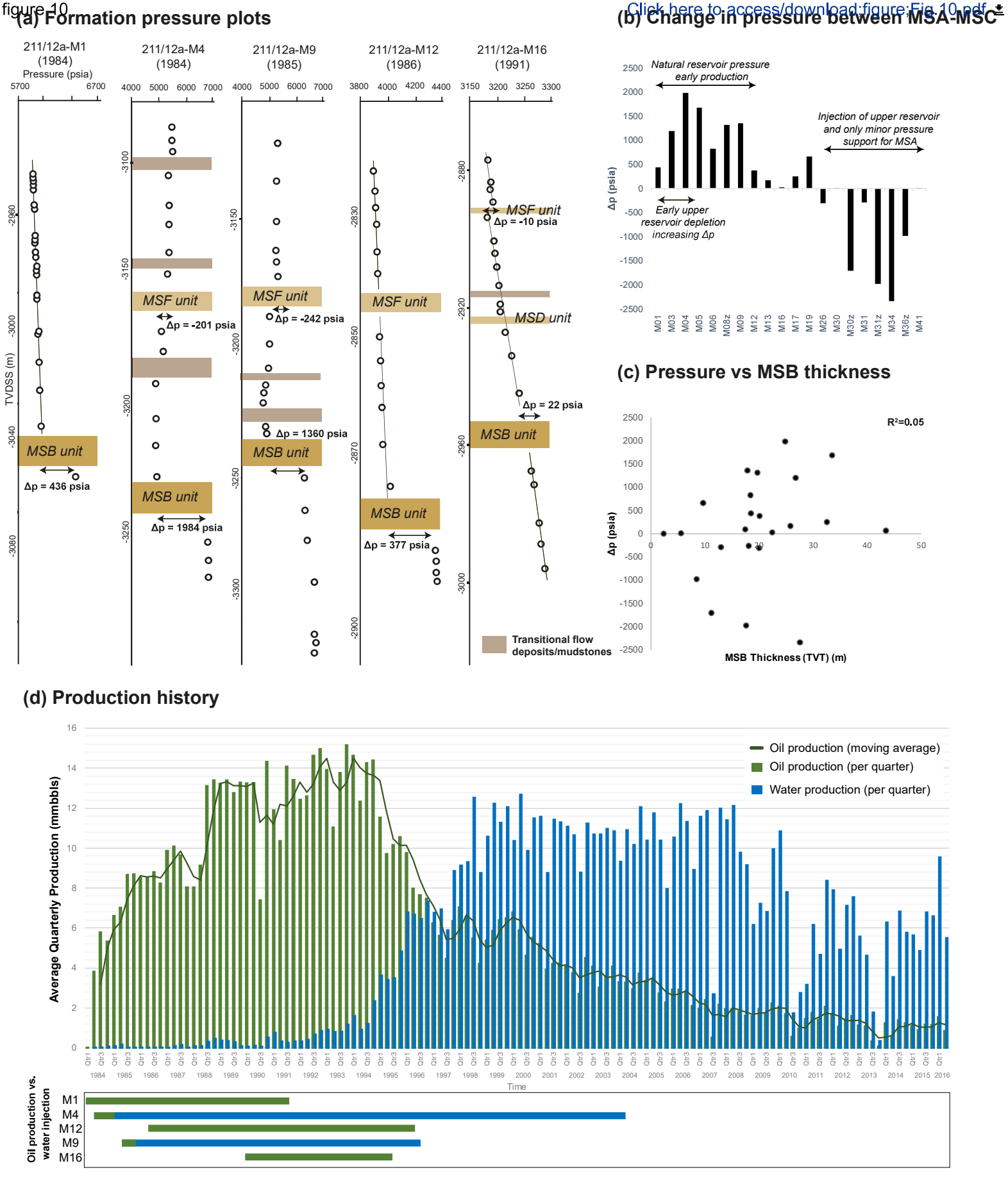

figure 11

Click here to access/download;figure;Fig.11.pdf

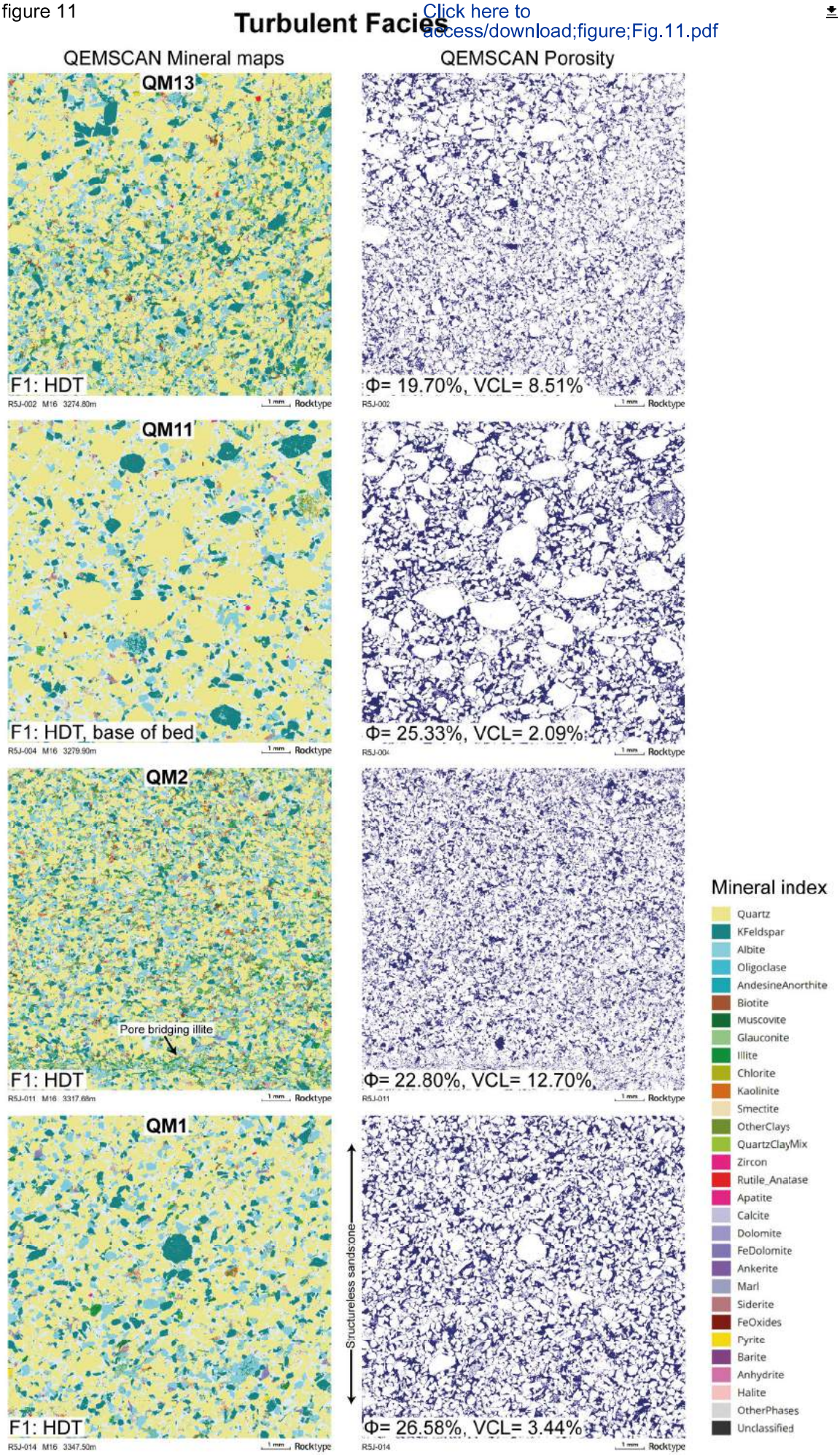

figure 12

Click here to access/download;figure;Fig.12.pdf

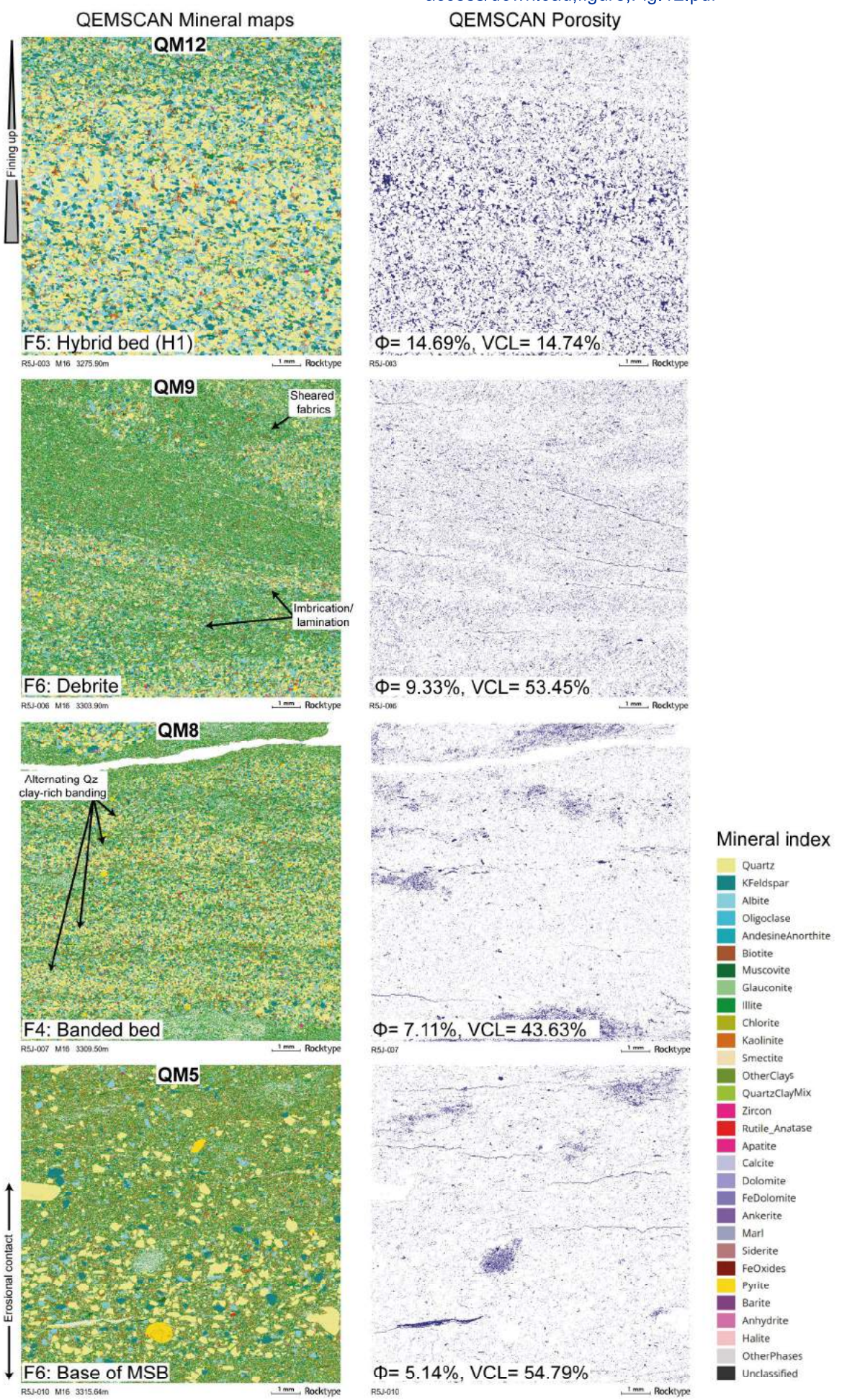

figure 13

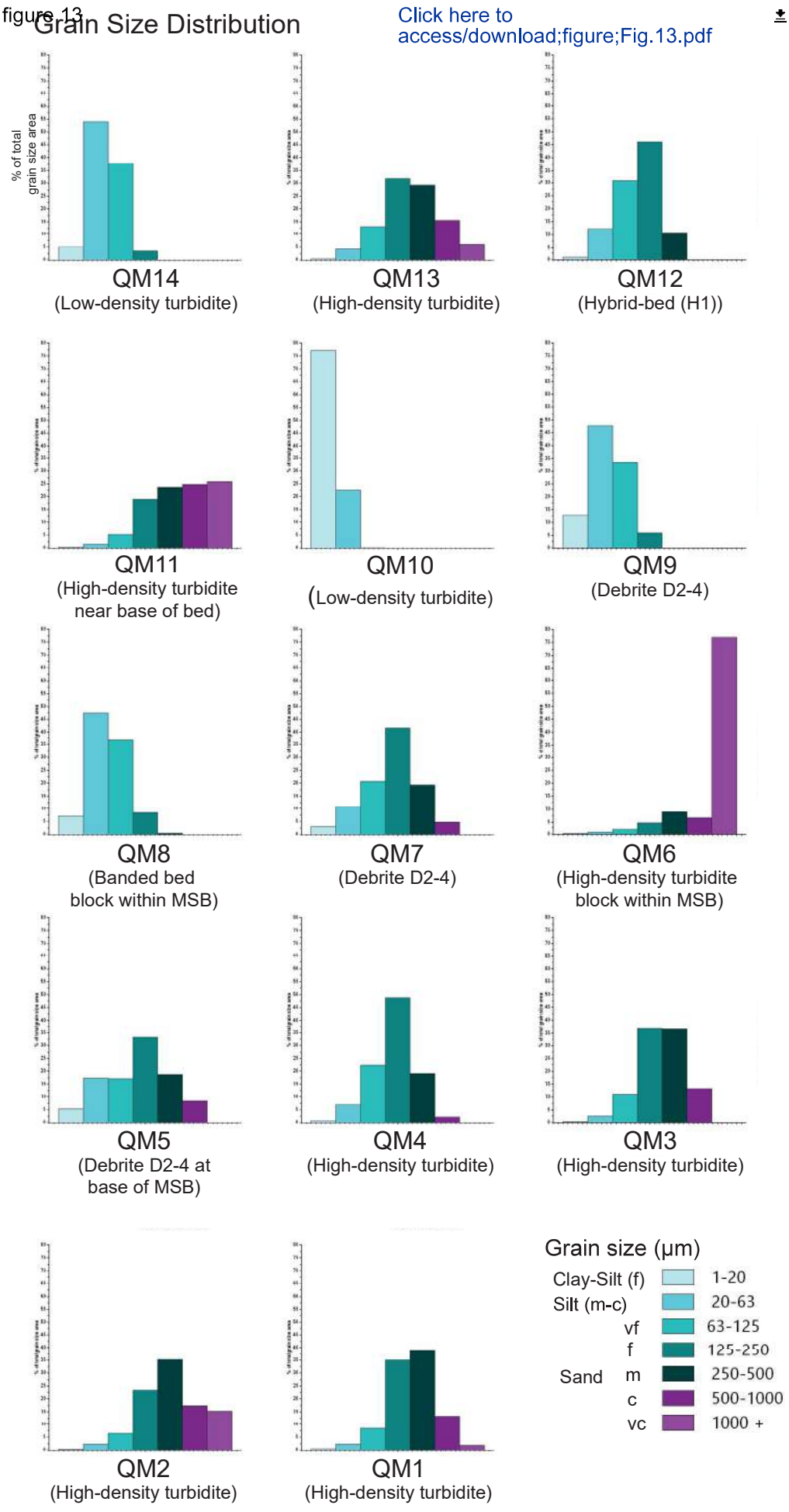
Grain Size Distribution
Click here to access/download;figure;Fig.13.pdf
% of total grain size area
QM14
(Low-density turbidite)
QM13
(High-density turbidite)
QM12
(Hybrid-bed (H1))
QM11
(High-density turbidite near base of bed)
QM10
(Low-density turbidite)
QM9
(Debrite D2-4)
QM8
(Banded bed block within MSB)
QM7
(Debrite D2-4)
QM6
(High-density turbidite block within MSB)
QM5
(Debrite D2-4 at base of MSB)
QM4
(High-density turbidite)
QM3
(High-density turbidite)
QM2
(High-density turbidite)
QM1
(High-density turbidite)
Grain size (µm)
Clay-Silt (f) 1-20
Silt (m-c) 20-63
Sand vf 63-125
f 125-250
m 250-500
c 500-1000
vc 1000 +

figure 14

Click here to access/download;figure;Fig.14.pdf

(a) Total clay vs. porosity

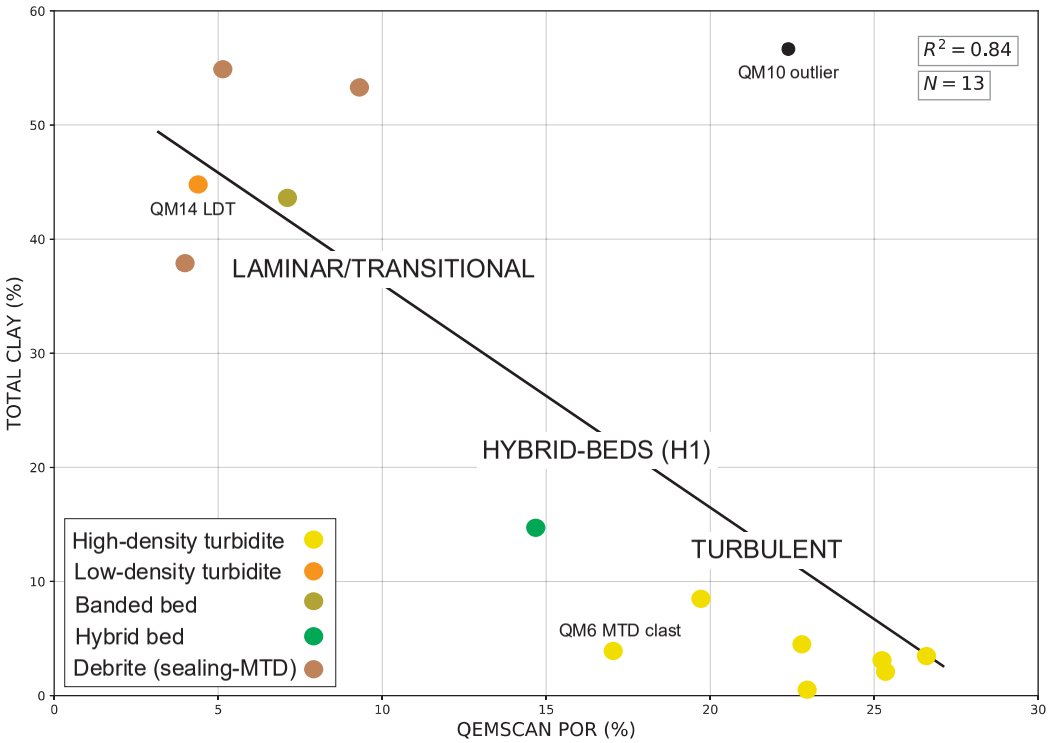

(b) Ternary plot

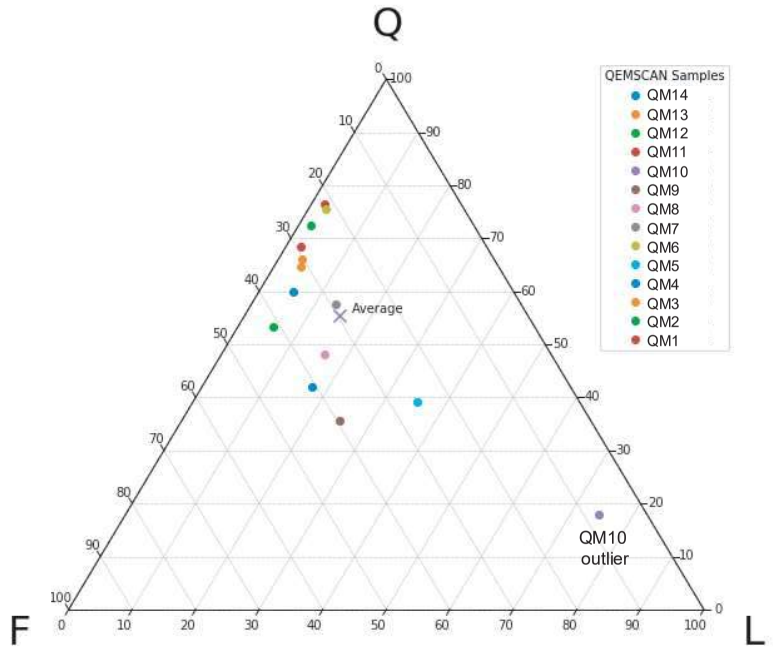

figure 15

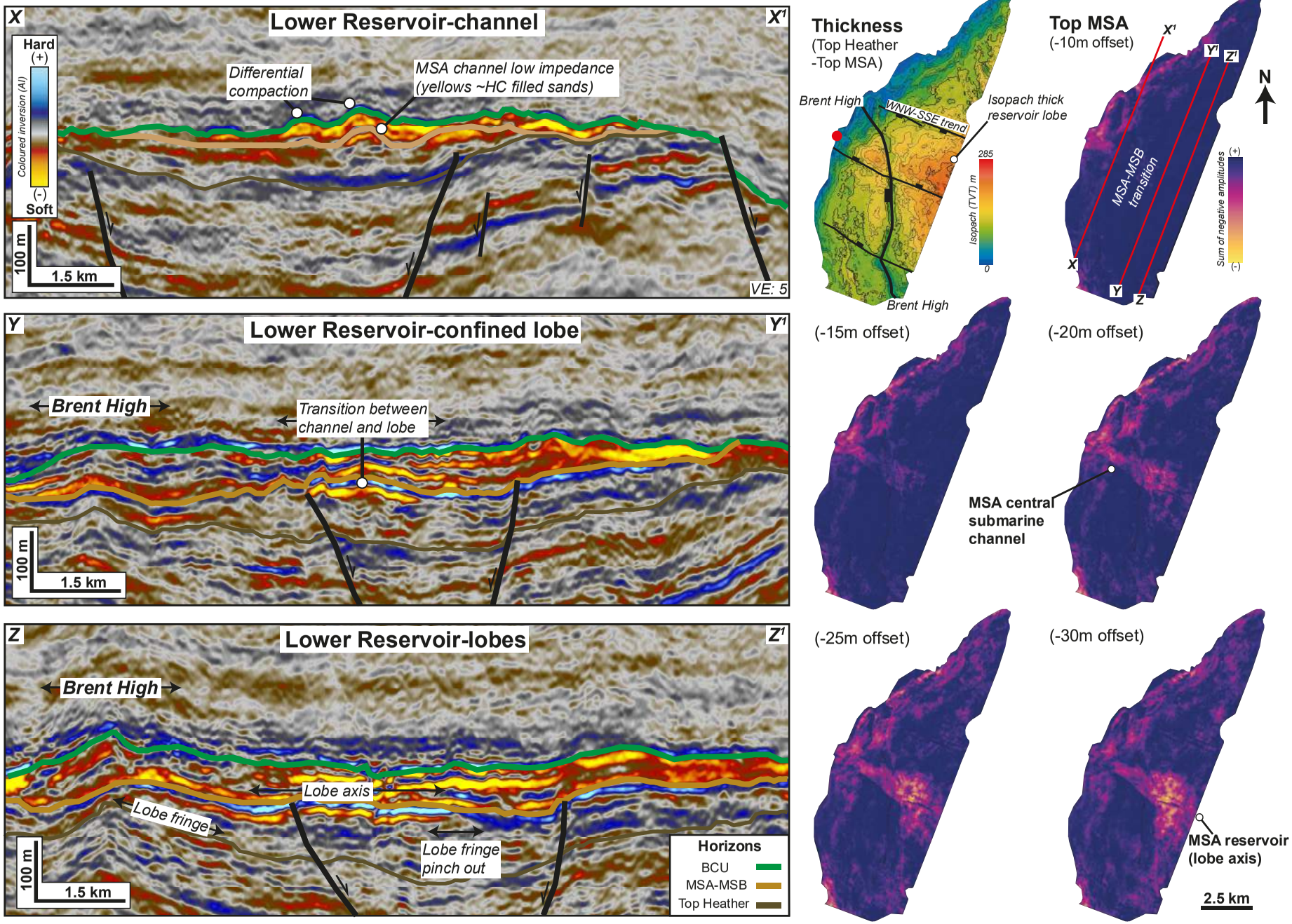

Figure 16

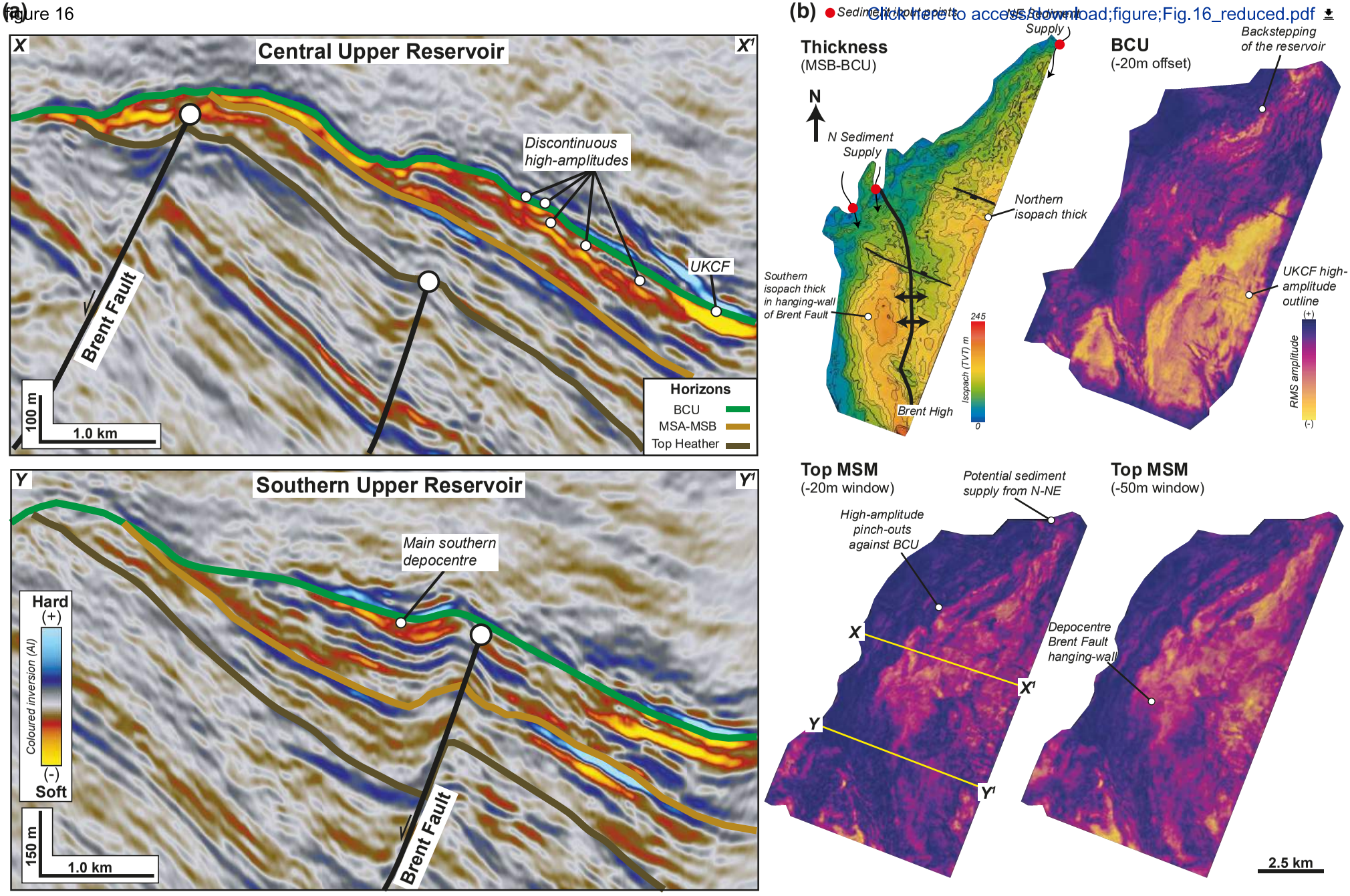

Figure 17

Click here to access/download;figure;Fig.17_reduce

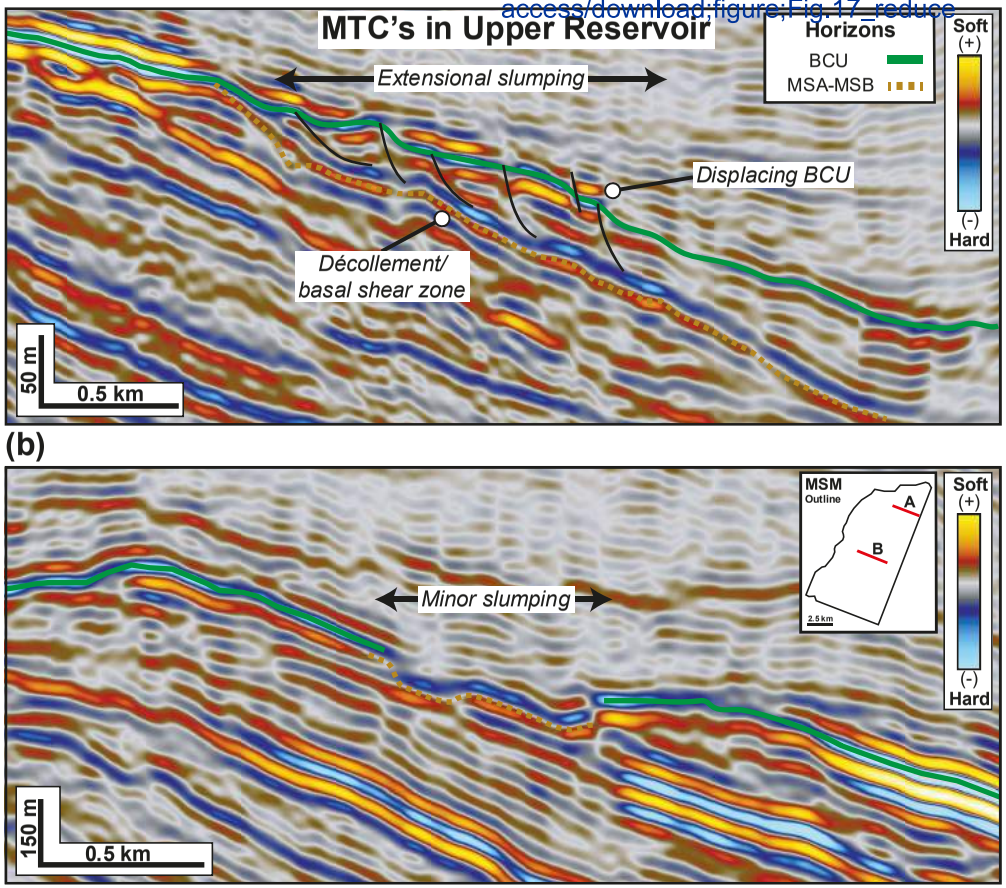

figure 18

Click here to access/download;figure;Fig.18.pdf

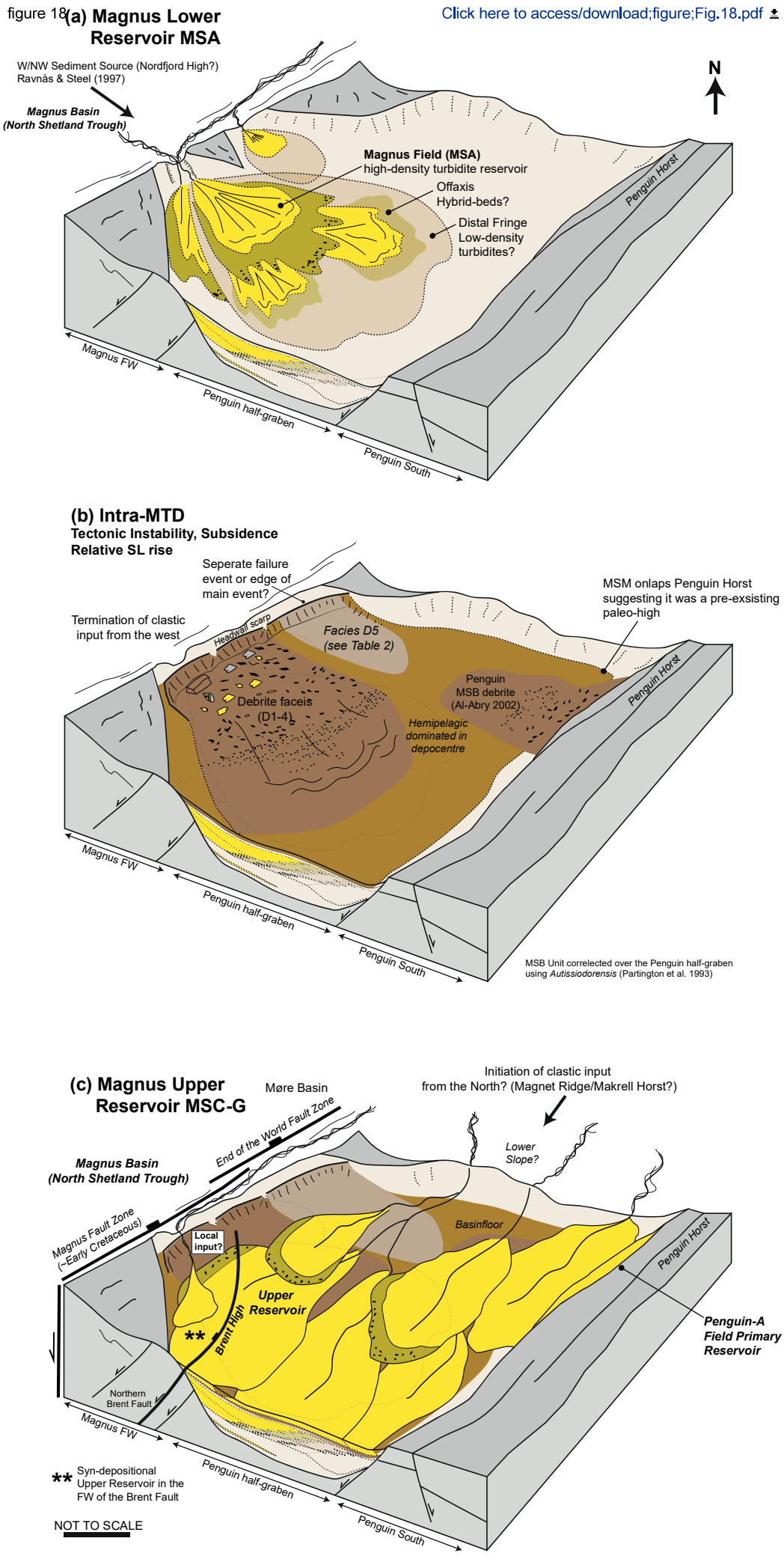

figure 19

Click here to access/download;figure;Fig.19.pdf